A Numerical Optimization Study of a Novel Electrospray Emitter Design

A Thesis Presented for the

Master of Science

Degree

The University of Tennessee, Knoxville

Joshua Harrison Howell

May 2022

Copyright © 2022 by Joshua Harrison Howell
All rights reserved.

ACKNOWLEDGEMENTS

I am thankful to God for being blessed with the opportunity and capability to continue to pursue my love of engineering and for that I am truly grateful. I would also like to thank my amazing wife and daughter, Misty and Amelia. I do not know what I would do without their endless love, encouragement, support, and patience.

I would like to acknowledge and express my sincere gratitude for my major advisor, Dr. Trevor Moeller. His research with propulsion is what first brought my interest to UTSI. However, at first it seemed there might not be any propulsion related projects for me to work on. After Dr. Moeller and I discussed my concerns, and my desire to work in propulsion with his group, he worked tirelessly for me to ensure that I was able to work on a project with him. It turned out that this project is the dream project I first had after discussing it with him in my entrance interview to the Space Institute. Dr. Moeller has been my mentor and advisor, and his enthusiasm for electric propulsion constantly reminds me of why I pursued engineering in the first place. I am grateful for all of his feedback, encouragement, enthusiasm, and mentorship, and also for his helping me to continually improve my critical thinking skills.

I also want to thank my thesis committee advisors, Dr. Brian Canfield, and Dr. Lino Costa. Dr. Canfield has constantly helped me to improve in my technical writing skills by continuing to offer me his valuable feedback on my work. I am also grateful for his insight into manufacturing processes that are allowing me to understand more of the project as a whole and to gain knowledge in an area I have not had the opportunity to study very much until now. I am thankful for all of Dr. Costa's feedback on my work as well. His feedback has helped me to further develop my critical thinking skills and to look at the project from angles I may not have thought of before. I am thankful for all of the guidance and help that Dr.

Canfield and Dr. Costa have given me to help further my knowledge and skills to help me continue growing into a better researcher to prepare me for my future research and academic career. I would also like to acknowledge Alexander Terekhov. His questions about the project have helped me to think about different aspects of the project and what challenges or influences might affect electrospray thruster designs. I would like to extend a special thanks to Justin Jones for helping to lay the foundation that allowed me to continue the electrospray thruster work at UTSI. I would also like to thank Adam Croft for taking a lengthy amount of time out of his own doctoral research to help me better understand how the HPC clusters at UTSI work, and for helping me try to work through some of the errors that occurred when trying to use HPC for my simulations. I would also like to thank the Center for Laser Applications and UTSI for their support for my project and enabling me to perform my master's research and transition into my doctoral work.

I would like to extend a very special thanks to my family, I could not have done this work without their love and support. I thank my mom, Shawn, for her love and support and for taking time out of her life to teach me. My dad, Mike, for inspiring my love for science and engineering as a child and continuing to do so. My sister, Jessica, for her endless encouragement. Her boyfriend, Ty, and my awesome nieces and nephews: Elijah, Luna, Noah, and my new niece on the way. I would also like to extend thanks to my mother-in-law Juanita Fain, my sister-in-law and brother-in-law Amber and Larry, and my other awesome nieces and nephews: Blaze, Addy, and Caspian. I would also like to thank Davey, Cheyenne, Gracie, and all of my other extended family and friends in Tennessee, Ohio, and Virginia.

ABSTRACT

The low thrust and high specific impulse of electric propulsion has been brought to the forefront for CubeSat and small spacecraft applications. Electrospray thrusters, which operate via electrostatic principles, have seen much research, development, and application in recent years. The small sizes of the spacecraft that utilize electrospray thrusters has focused development into the miniaturization of this technology to the micro-scale. Miniaturization introduces design challenges that must be addressed, including power supply mass and footprint requirements. This consequence requires investigation into the effects of design choices on the thruster onset voltage, defined as the voltage at which ion emission begins. This study focuses on the second design iteration of novel electrospray thruster technology being developed by the University of Tennessee Space Institute. The thruster design consists of an emitter chip with capillaries, etched into borosilicate glass with an indium tin oxide extraction grid deposited on the top surface, which are fabricated using ultrafast laser machining in the Center for Laser Applications. Emitter capillaries open into wider, cylindrical voids defined as the electrospray cavities. An onset-voltage-optimization study is performed via electrostatic simulations by determining design choices that minimize the onset voltage for three design parameters: the electrospray-cavity aspect ratio, the effects of indium tin oxide erasure as a consequence of the laser machining process, and the choice of an ionic liquid propellant. The results show that electrospray cavities with smaller dimensions lead to a decrease in onset voltage, but optimal aspect ratios can be determined. Erasure of the extraction grid leads to an increase in onset voltage, which is greater for smaller electrospray cavity dimensions, and is most profound for small electrospray cavity heights. Therefore, the amount of erasure should be minimized as much as machining processes will allow, since smaller electrospray-cavity widths and heights are a desirable design choice to minimize onset voltage. The results also show that, although more

investigation is required, ionic liquid propellants with lower surface tensions yield smaller onset voltages. This work details the methodology of the optimization study and provides best practices in preliminary electrospray emitter chip design for electrospray thrusters.

TABLE OF CONTENTS

CHAPTER 1: INTRODUCTION 1
1.1 Overview 1
1.2 Electric Propulsion for Space Applications 4
1.2.1 Background and Relevance 4
1.2.2 Types of Electric Propulsion Devices and Notable Missions 8
1.3 Electrospray Thrusters for Electric Space Propulsion 12
1.3.1 Basic Overview of Electrospray Thrusters 14
1.3.2 Emitter Design Types 15
1.4 Motivation 15
1.5 Literature Review of Related Work 18
1.5.1 Early Observations and Research of Electrospray Physics 18
1.5.2 Numerical Modeling of Electrospray Physics 24
1.5.3 Effects of Electrospray-Cavity Aspect Ratio on Onset Voltage 29
1.5.4 ITO Extraction Grid Erasure 32
1.5.5 Ionic Liquid Comparison 32
1.6 Organization 34
CHAPTER 2: PHYSICAL BACKGROUND 36
2.1 Fluid Dynamics Governing Equations 36
2.2 Electromagnetics Governing Equations 39
2.3 Application of Physics to Electrospray Devices 48
2.3.1 Electrohydrodynamic Model 48
2.3.2 Quasi-Static Evolution 53
2.3.3 Taylor Cone Modeling 58
CHAPTER 3: METHODOLOGY 64
3.1 Design of Research Model for Electrostatic Simulations 64
3.2 Determining Onset Voltage 67
3.2.1 Mesh Resolution Guidelines for Mesh Independent Solutions 72

3.2.2 Mesh Convergence Study....74
3.3 Simulation Variations....74
3.3.1 Electrospray Cavity Aspect Ratio....74
3.3.2 ITO Extraction Grid Erasure....76
3.3.3 Ionic Liquid Comparison....76
3.3.4 Comparison of Single-Capillary Emitter and Multi-Capillary Arrays....78
CHAPTER 4: RESULTS AND DISCUSSION....79
4.1 Mesh Convergence Study Results....79
4.2 Electrospray Cavity Aspect Ratio....82
4.3 ITO Extraction Grid Erasure....91
4.4 Ionic Liquid Comparison....94
4.5 Comparison of Single-Capillary Emitters and Multi-Capillary Arrays....98
CHAPTER 5: CONCLUSIONS AND FUTURE WORK....102
5.1 Conclusions....102
5.2 Suggestions for Future Work....104
WORKS CITED....106
VITA....116

LIST OF TABLES

Table 2.1. Fluid dynamics governing equations. 40
Table 2.2. Maxwell's Equations. 43
Table 2.3. Electrohydrodynamics governing equations. 54
Table 2.4. Interfacial conditions for electrostatic assumption 55
Table 3.1. AR variations, and their corresponding values of m and d used in the mesh-convergence study. 75
Table 3.2. Relevant physical properties of the ILs used in this study at $\mathbf{25}$° C ... 77

LIST OF FIGURES

Figure 1.1. General operational principle of an electrospray device. 2
Figure 1.2. Comparison of specific impulse and thrust levels of common propulsion types (taken from [2]). 7
Figure 1.3. μCAT thruster developed for the CANYVAL-X mission by The George Washington University (taken from [5]). 9
Figure 1.4. A Cluster of SpaceX Starlink satellites (taken from [7]).....11
Figure 1.5. Busek colloidal thruster developed for the LISA Pathfinder mission (taken from [14]). 13
Figure 1.6. Schematics of typical emitter design types. 16
Figure 1.7. Schematic representation of the μSTAMPS novel emitter design....19
Figure 1.8. Photograph of the Taylor cone and liquid jet from Zeleny's experiments with the instability of electrified liquid surfaces (taken from [20]). 21
Figure 1.9. Photograph of results from Taylor's work. Note the black chalk markings that distinguish the angle 98.6° which corresponds to twice the semi-vertex angle of 49.3° (taken from [16]).....23
Figure 1.10. Extraction grid erasure as a side-effect of ultrafast-laser machining. 33
Figure 2.1. Plot of the equilibrium voltage as it approaches a steady-state value for decreasing ra (taken from [34]). 59
Figure 2.2. Representation of the Taylor cone modeling showing the effects of changes in w (taken from [34]). 62
Figure 3.1. 3D view of the single-capillary model from Ansys EDT.....65
Figure 3.2. 2D view of the model from Figure 3.1 including the dimensions of the electrospray cavity. 66
Figure 3.3. 3D view of the Ansys EDT model used for the extraction grid erasure simulations. 68

Figure 3.4. 2D view of the model from Figure 3.3 including the dimensions of the electrospray cavity. 69
Figure 3.5. 3D view of the multi-emitter array. 70
Figure 3.6. 2D view of the model from Figure 3.5 including the dimensions of the electrospray cavity. 71
Figure 3.7. Regions of the IL column where specific element lengths, Le, were required. 73
Figure 4.1. Mesh convergence study results for $w \approx 11.63$. 80
Figure 4.2. Mesh convergence study results for $w \approx 13.95$. 81
Figure 4.3. Comparison of the effects of emitter AR on $V0$ for variations in d with m held constant. 83
Figure 4.4. Values of d for increasing m values that result in $ARopt$. 84
Figure 4.5. Comparison of the behavior of $V0$ with increasing d for set values of m..... 87
Figure 4.6. Comparison of the effects of emitter AR on $V0$ for variations in m with d held constant. 88
Figure 4.7. Comparison of the behavior of $V0$ with increasing m for set values of d. 89
Figure 4.8. Values of m for increasing d values that result in $ARopt$. 90
Figure 4.9. Effects of ITO We on $V0$ for the $ARopt$ values found in Section 4.2. 92
Figure 4.10. Percent increase in onset voltage with increasing m and We. 93
Figure 4.11. $V0$ with variation in AR for the ILs considered in this study for $m = 5$ µm..... 95
Figure 4.12. $V0$ with variation in AR for the ILs considered in this study for $m = 25$ µm..... 96
Figure 4.13. $V0$ with variation in AR for the ILs considered in this study for $m = 50$ µm..... 97
Figure 4.14. Comparison of convergence study results between the PC and INTEGRITY $V0$ values. 99

Figure 4.15. Comparison of $V0$ results between a high-pitch, multi-emitter array on INTEGRITY and the single-capillary case on the PC.....101

NOMENCLATURE

Note: Characters representing vectors are in **bold**, and tensors appear with $\overline{\overline{double\ overbars}}$.

Constants

g	*Sea Level Gravitational Acceleration*	*9.81 m/s^2*
ε_0	*Vacuum Permittivity*	8.85×10^{-12} *F/m*
μ_0	*Permeability of Free Space*	1.257×10^{-6} *H/m*

Propulsion Parameters

$\Delta \boldsymbol{V}$	*Velocity Increment*	*m/s*
$\boldsymbol{u_e}$	*Exhaust Velocity*	*m/s*
m_0	*Initial Mass*	*kg*
m_f	*Final Mass*	*kg*
m_0/m_f	*Mission Mass Fraction*	--
m_p	*Propellant Mass*	*kg*
I_{sp}	*Specific Impulse*	*s*

η	*Conversion Efficiency*	*--*
Δt	*Mission Time*	*s*
α	*Power Plant Mass*	*kg*

Electromagnetics

R_e	*Electric Reynolds Number*	*--*
V_0	*Onset Voltage*	*V*
q	*Free Charge Density*	*C/m^3*
D	*Electric Displacement*	*C/m^2*
B	*Magnetic Induction*	*T*
H	*Magnetic Field Intensity*	*A/m*
J	*Free Electric Current Density*	*A/m^2*
E	*Electric Field Strength*	*V/m*
M	*Magnetization*	*A/m*
P	*Polarization*	*C/m^2*
$\overline{\overline{\chi_m}}$	*Magnetic Susceptibility Tensor*	*--*

$\overline{\overline{\chi_e}}$	*Electric Susceptibility Tensor*	*--*
$\bar{\bar{\varepsilon}}$	*Absolute Permittivity Tensor*	*F/m*
$\bar{\bar{\mu}}$	*Absolute Permeability Tensor*	*H/m*
χ_e	*Scalar Electric Susceptibility*	*--*
χ_m	*Scalar Magnetic Susceptibility*	*--*
ε_r	*Relative Permittivity (Dielectric Constant)*	*--*
μ_r	*Relative Permeability*	*--*
$\boldsymbol{\varepsilon}$	*Absolute Permittivity*	*F/m*
$\boldsymbol{\mu}$	*Absolute Permeability*	*H/m*
q_s	*Surface Charge Density*	*C/m^2*
K	*Sheet-Current Density*	*A/m*
$\boldsymbol{b}_s^{EM}$	*Electromagnetic Body Force Acting on a Fluid*	*N/m^3*
τ_E	*Characteristic Electric Time*	*s*
σ	*Electrical Conductivity*	*S/m*
τ_M	*Characteristic Magnetic Time*	*s*

V_E	*Scalar Voltage*	*V*
E_{EQ}	*Equilibrium Electric Field Strength*	*V/m*
C	*Ratio of E_{Apex} to $V_{Applied}$*	*1/m*
E_{Apex}	*Electric Field Strength at Liquid Tip*	*V/m*
V_{EQ}	*Equilibrium Voltage*	*V*

Fluid Mechanics

γ	*Surface Tension Coefficient*	*N/m*
ρ	*Density*	*Kg/m^3*
$\boldsymbol{u}$	*Fluid Velocity Vector*	*m/s*
P	*Pressure*	*Pa*
$\bar{\bar{\tau}}$	*Viscous Stress Tensor*	*Pa*
$\boldsymbol{b}$	*Body Force*	*N/m^3*
R	*Specific Gas Constant*	*J/kg-K*
κ	*Local Curvature at the Fluid-fluid Surface*	*1/m*

Energy and Thermodynamics

v	*Scalar Velocity*	*m/s*
U_i	*Internal Energy*	*J/kg*
$\boldsymbol{q}$	*Heat Flux Vector*	*W/m^2*
U	*Total Energy*	*J*
k	*Thermal Conductivity*	*W/m-K*

Geometric Properties

AR	Electrospray-Cavity Aspect Ratio	--
m	Electrospray-Cavity Width	*µm*
d	Electrospray-Cavity Height	*µm*
r_c	*Capillary Radius*	*µm*
d	*Distance from Emitter to Extraction Electrode*	*µm*
h	*Taylor Cone Height from Base to Liquid Apex*	*µm*
p	*Emitter Capillary Pitch*	*µm*
h_e	*Emitter Height*	*µm*

AR_{opt}	Optimal Electrospray-Cavity Aspect Ratio	--
W_e	ITO Extraction-Grid Erasure	*μm*

Other

A_1	*Empirical Constant for Onset Voltage Scaling Law*	--
ϕ_0	*Taylor Cone Half-Angle*	°
∇	*Nabla Operator*	--
δ_{ij}	*Kronecker Delta*	--
$\boldsymbol{n}$	*Unit Normal Vector*	--
l	*Characteristic Length*	*m*
∇^2	*Laplacian Operator*	--
θ	*Angle Between Taylor Cone Surface and the Horizontal*	°
t	*Parametric Variable of the Conic Section*	--
r_a	Radius of the Conic Section Base	*m*
β	Revolution Angle of Conic Section	rad
w	Sharpness Parameter for Conic Section	--

L_e	Element Length	nm
M	Maximum Element Length	nm

Subscript and Superscript Characters

i	*ith Matrix Row*	--
j	*jth Matrix Column*	--
t	*Tangential Vector Component*	--
n	*Normal Vector Component*	--
1	*Medium 1*	--
2	*Medium 2*	--

CHAPTER 1: INTRODUCTION

1.1 Overview

Electrospray thrusters are a type of electric propulsion device that relies on the emission of a propellant, in the form of ions, liquid droplets, or a combination thereof. This process is achieved via an electric field that is generated by an applied potential difference between an extraction grid and the emitter itself. Ionic liquids (ILs) are the most commonly used propellant for electrospray thrusters. The general operational principles of electrospray emitters are shown in Figure 1.1. Because of their small size, electrospray thrusters have capabilities that are promising for important uses in CubeSat (small-scale satellites) propulsion systems, such as attitude control and controlled deorbit upon mission completion. This is a great benefit to prolong the mission life of the CubeSat and also prevents the buildup of space junk orbiting around a body. Electrospray thrusters are suited to CubeSat operation and are also a desirable choice for any low thrust level applications.

Requirements for propellant, thrust, specific impulse, and thrust density vary depending on the specific requirements for a given space mission. However, since electrospray thrusters are primarily used in smaller-scale roles, an important objective in the design of any electrospray thruster is the reduction of the power-supply size and mass. Even as the size of micro-scale thrusters is reduced, their usefulness will be greatly diminished if they require a prohibitively large power supply. Therefore, it is important to drive the power-supply size and mass requirements to a minimum when developing an electrospray thruster. The size and mass of the power supply are determined by the voltage requirements for which the thruster begins emission, thereby generating thrust. This voltage is defined as the onset voltage, V_0 in volts (V) and represents the minimum voltage

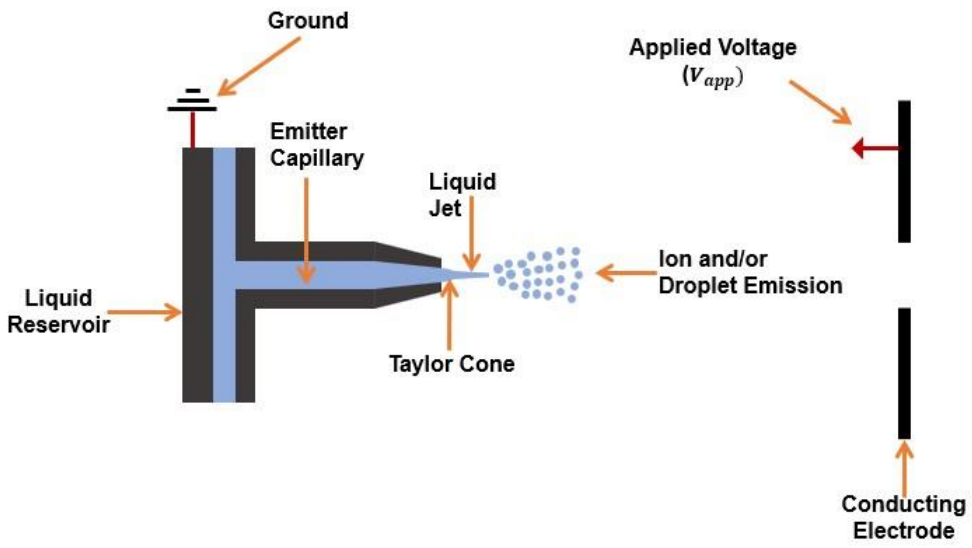

Figure 1.1. General operational principle of an electrospray device.

requirement for the electrospray process to begin. Therefore, it is essential to design an electrospray thruster with the lowest practical V_0 in order to decrease the onboard power supply footprint and mass.

When designing an electrospray thruster, there are several important design features that must be considered. However, any successful design will take into consideration the mass and volume of the required power supply, which depend on the voltage requirements of the thruster. Therefore, it is important to perform a numerical study to optimize the power supply requirements for the electrospray thruster. This is accomplished by designing emitter chips that minimize the onset voltage requirement. This optimization study is concerned with three electrospray thruster design features that have an impact on V_0 which are introduced in Section 1.4. If knowledge of the power supply requirements as determined by the onset voltage are determined numerically, via simulations, an understanding of the optimal design can be gained before fabrication of the emitter chip has begun. This leads to the development of guidelines, or best practices, for designing an electrospray thruster. These design guidelines can then be used as a starting point for development of electrospray thrusters.

The above is a brief introduction to this thesis. The remainder of Chapter 1 will provide a comprehensive look at the relevant background information for this study. This begins with an overview of the background and importance of electric propulsion. The background and relevance of electric propulsion is then followed by a review of electric propulsion types and the missions that implemented them. A discussion on the basic operation of electrospray emitters is then considered, which also includes descriptions of the three major electrospray emitter types. The background information of Chapter 1 concludes with a literature review of the relevant research that has been used as a background and starting point for this study.

1.2 Electric Propulsion for Space Applications

1.2.1 Background and Relevance

There are many technical considerations that are evaluated for any given mission in space. Regardless of the technical specifics, any space mission of genuine interest will carry some form of payload into space. The ability for a given spacecraft, with specific mission requirements, to deliver the largest possible payload mass to its destination is vital. The mission payload mass influences the choice of spacecraft and the propellant mass required to complete any specified set of maneuvers needed for the mission.

The most important propulsion parameters for any spacecraft are related to each other through Tsiolkovsky's rocket equation, also known as the ideal rocket equation or simply the rocket equation, which is given by [1]:

$$\Delta \boldsymbol{V} = \boldsymbol{u_e}\, ln(\frac{m_0}{m_f}), \qquad [1.1.1]$$

with $\Delta\mathbf{V}$ being the velocity increment in meters per second (m/s), $\mathbf{u_e}$ the exhaust velocity with units of m/s, $\mathrm{m_0}$ the initial wet mass in kilograms (kg), which includes propellant mass, and $\mathrm{m_f}$ the final mass in kg, which includes rocket engines, propellant tanks, payload mass, and, if the propellant was completely consumed during the maneuver, any other non-propellant mass. If the propellant has been completely used, the final mass is defined as the dry mass.

To minimize the required propellant mass, the unitless (--) mass fraction, m_0/m_f, of the spacecraft can be examined. Without defining the constituent masses belonging to m_0, m_0 can be written as $m_f + m_p$, with m_p defined as the

propellant mass in kg for any given maneuver. Keeping this in mind and referring to Equation [1.1.1], reducing the propellant mass results in a mass fraction that grows closer to unity. Solving for the mass fraction in Equation [1.1.1] yields [1]:

$$\frac{m_0}{m_f} = e^{(\frac{\Delta \boldsymbol{V}}{\boldsymbol{u_e}})}. \qquad [1.1.2]$$

Propulsion performance is rarely quoted in values of exhaust velocity, $\boldsymbol{u_e}$; therefore, it is useful to introduce another performance parameter, the specific impulse, or I_{sp}, in units of seconds (s).

The relationship between exhaust velocity and specific impulse is defined as:

$$I_{sp} = \frac{\boldsymbol{u_e}}{\boldsymbol{g}}, \qquad [1.1.3]$$

where *g* is defined as the standard sea-level acceleration due to gravity in meters per second squared (m/s^2). Specific impulse is a measure of the efficiency with which a propulsion system generates thrust. If Equation [1.1.3] is solved for $\boldsymbol{u_e}$ and substituted into [1.1.2], the mass fraction can be defined in terms of specific impulse:

$$\frac{m_0}{m_f} = e^{(\frac{\Delta \boldsymbol{V}}{I_{sp} g})} \qquad [1.1.4]$$

Examining the argument of the exponential function in Equation [1.1.4], and with the velocity increment set for a given maneuver, the only parameter that can be altered is the specific impulse of the spacecraft thruster. Since bringing the mass fraction as close to unity as possible is the desired outcome, the argument

of the exponential function in Equation [1.1.4] must be brought as close to zero as possible. This can be achieved by increasing the specific impulse, I_{sp}, or equivalently, the exhaust velocity, $\boldsymbol{u_e}$. It is worth noting that the optimum I_{sp}, $\widehat{I_{sp}}$ (s), can be related to the power plant mass, α (kg) by [1]

$$\widehat{I_{sp}} = \frac{1}{g}\sqrt{\frac{2\eta\Delta t}{\alpha}}, \qquad [1.1.5]$$

where η is the unitless conversion efficiency to thrust power (--) (and is equal to unity if perfect conversion is assumed), and Δt is the mission time in units of s. These principles can be used to guide the design of a propulsion system based on various mission parameters.

This is where the benefits of Electric Propulsion (EP) can be seen. Many EP systems can achieve high specific impulse, which results in the ability to deliver much larger payload masses to their target destinations or perform station-keeping maneuvers for extended periods of time. However, the high specific impulse that is achievable with EP results in thrust levels on the order of micro-newtons to newtons (μN to N). Figure 1.2 demonstrates the ranges of specific impulse and thrust levels for several propulsion types. Examining Figure 1.2 highlights the high specific impulse and lower thrust levels of the three EP types: electrothermal, electromagnetic, and electrostatic in comparison to higher-thrust propulsion types, e.g., chemical, and nuclear rockets. The following section contains a brief introduction to these categories of EP devices and some notable EP thruster types that have seen flight time in space missions.

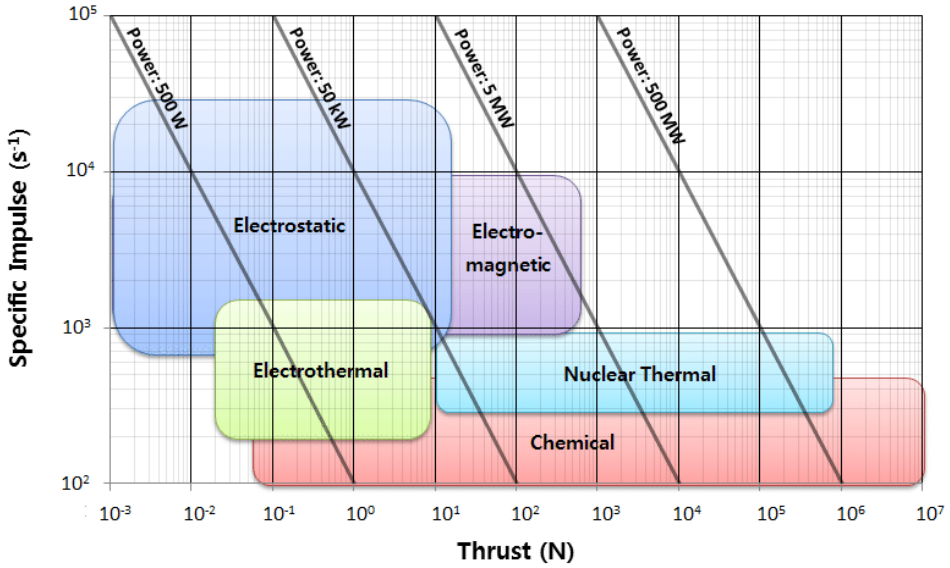

Figure 1.2. Comparison of specific impulse and thrust levels of common propulsion types (taken from [2]).

1.2.2 Types of Electric Propulsion Devices and Notable Missions

Electric propulsion thrusters are designed to accelerate propellants for propulsion by use of electrical heating (e.g., resistors) and by the use of magnetic or electric (or a combination of the two) body forces [1]. Electric propulsion devices are categorized by the physical processes that describe the propulsion method of the system. These are classified by three major types: electrothermal acceleration, electromagnetic acceleration, and electrostatic acceleration.

Electrothermal acceleration uses some form of electric device to heat gases or plasmas to high temperatures and expands them through a nozzle. This is done using resistors or an electrical arc between two electrodes as used in arcjet thrusters. These types of EP devices most strongly resemble traditional chemical rockets in their operation.

An example of a miniature electrothermal EP device was used recently in a mission of interest called the CubeSat Astronomy by NASA and Yonsei using Virtual Telescope Alignment eXperiment (CANYVAL-X) [3]. This was a joint mission between the National Aeronautics and Space Administration (NASA), The George Washington University (GWU), and Yonsei University in South Korea. The goal of the mission was to test the ability of two CubeSats, small satellites used in space research, to communicate with each other and fly in formations autonomously. GWU developed a Micro-Cathode Arc Thruster (μCAT) as a propulsive device to aid in stabilization and orbital control for the two satellites. The μCAT utilized a metal propellant that operated by cathode ablation and achieved specific impulse in the range of 200 – 3500 s with thrust levels reaching the millinewton (mN) range [4]. The μCAT thruster that was developed for the CANYVAL-X mission is displayed in Figure 1.3. Highlighting the small scale of EP devices, an μCAT device similar to the one used in the CANYVAL-X mission had

Figure 1.3. µCAT thruster developed for the CANYVAL-X mission by The George Washington University (taken from [5]).

a total mass of less than 200 grams (g) [4]. Ultimately, the goal of communication between the CubeSats failed due to ground-level interference. However, the technology developed for this project helped to advance the field of electrothermal EP.

Electromagnetic acceleration devices rely on interactions between electric and magnetic fields that act on bodies of plasma propellants to influence the direction of travel of the propellant and thus provide thrust to the system [1]. Because of these interactions, devices such as these are more theoretically complex and have seen less research and development efforts than other EP technology.

The Hall-effect thruster (HET) is one electromagnetic EP device that has been successfully developed and is currently being used in space applications. SpaceX and communications company OneWeb are two groups that are seeking to increase the availability of affordable broadband internet worldwide [6]. SpaceX and OneWeb both utilize Hall-effect thrusters on their satellites. The SpaceX Starlink program HET utilizes krypton propellants, while OneWeb thrusters are battery-powered xenon HETs [7, 8]. These thruster systems allow the satellite to make orbital corrections and deorbiting burns. SpaceX already has approximately 1500 satellites in the Starlink constellation [9], while the OneWeb constellation consists of approximately 288 satellites [10]. Figure 1.4 shows a cluster of SpaceX Starlink satellites ready for deployment.

The final class of EP devices operate via electrostatic acceleration. These devices use the Coulomb force provided by an electrical field generated by an applied potential difference to accelerate ions either from a plasma (ion engines), or a combination of ions and a liquid propellant (electrospray and colloidal thrusters). NASA successfully utilized ion engines for the Deep Space 1 and Dawn

Figure 1.4. A Cluster of SpaceX Starlink satellites (taken from [7]).

space exploration missions [11, 12]. Colloidal thrusters developed by Busek Space Propulsion and Systems have been flown on the NASA Space Technology 7 (ST7) for the European Space Agency (ESA) Laser Interferometer Space Antenna (LISA) Pathfinder mission. These colloidal thrusters were used to place a trio of satellites in near-perfect free fall to minimize disturbances caused by drag for use in the detection of gravitational waves [13]. Because of the sensitivity required to detect gravitational waves, highly accurate thrust levels on the order of μN were required. The colloidal thrusters developed by Busek were able to provide such thrust levels, resulting in a complete mission success. The colloidal thrusters developed by Busek for this mission can be seen in Figure 1.5.

Since the research topic of this thesis is electrospray thruster technology, the next few sections will further discuss this type of electrostatic thruster. A brief overview of the technology, electrospray thruster designs and applications, the electrospray thruster considered in this study, and relevant work in the literature will be examined.

1.3 Electrospray Thrusters for Electric Space Propulsion

Before a more detailed analysis of the underlying physical background of electric propulsion is examined, a broad overview is considered. This overview begins with a basic outline of how electrospray thrusters operate, leading design choices that are being studied and/or in current use, and their contributions to aerospace missions. This section concludes with a literature review of relevant work in the field and the motivation for this current work.

Figure 1.5. Busek colloidal thruster developed for the LISA Pathfinder mission (taken from [14]).

1.3.1 Basic Overview of Electrospray Thrusters

Consider a conducting liquid contained within a capillary that is fed via a reservoir. This liquid is placed at some distance from a conducting electrode (or extraction grid in the case of electrospray thrusters) that is attached to a power supply. The surface of the liquid in the capillary is considered an interface because it meets with air or vacuum, as is the case for electrospray thrusters. When operating in vacuum in the absence of any applied voltage, there are the surface tension, electrical stresses, gravitational interactions, and pressure forces acting on the liquid. When a voltage is applied between the conducting electrode and the liquid, polarization occurs at the interface, resulting in excess ionic charge at the surface [15].

With the presence of this electrostatic force, the liquid surface geometry begins to deform into a quasi-conical shape [15]. At this point, the surface tension and electrostatic forces are in balance. As the magnitude of the electrostatic force increases, there is a certain threshold level where the liquid surface geometry becomes fully conical. This resulting conical shape, which was first studied rigorously by G. I. Taylor in 1964 [16] and has come to be known as a Taylor cone in his honor, indicates when the electrostatic and surface tension forces are perfectly balanced. Once the electrostatic force is increased further, it overcomes the surface tension of the liquid locally, causing a liquid jet to emerge from the tip of the Taylor cone. The result of this instability is the emission of ions, a liquid stream, and/or a combination of ions and liquid droplets with a net charge.

Most electrospray devices are designed and operate in a similar fashion. From the example above, the capillary is defined as the emitter, the conducting electrode acts as an extraction grid, and the liquid propellants most commonly

used are ILs. In addition to these design features, electrospray devices also contain power supplies and a liquid-feeding mechanism to the capillary or emitter.

1.3.2 Emitter Design Types

Since their potential use as an electrostatic thruster was first observed, several types of electrospray emitter designs have been studied. Slender, capillary-like emitters have been studied, along with externally wetted and porous emitter types. A schematic representation of these three basic emitter types is shown in Figure 1.6.

Although designs may vary, the general operation of electrospray emitters is the same. One characteristic that is common among all design types is a narrow capillary or emitter that is, for some designs, tapered to a sharp point. This design characteristic is chosen to enhance the electric field intensity at the tip of the emitter, which allows for a decreased voltage for the electrospray phenomena to begin. This voltage that accompanies the beginning of electrospray is known as onset voltage and will be discussed further in Chapter 2. Lower onset voltages are desirable, as smaller power supplies help reduce the size and cost of the thruster. Reducing the size and cost of the thruster allows for an increase in payload mass, or a larger supply of propellant, which can increase the flight time of the thruster. Therefore, it is important to design an electrospray thruster with the lowest practical onset voltage that can be achieved.

1.4 Motivation

When designing an electrospray thruster, there are several important design features that must be considered. Any successful design will take into consideration the size of the required power supply, which depends on the voltage

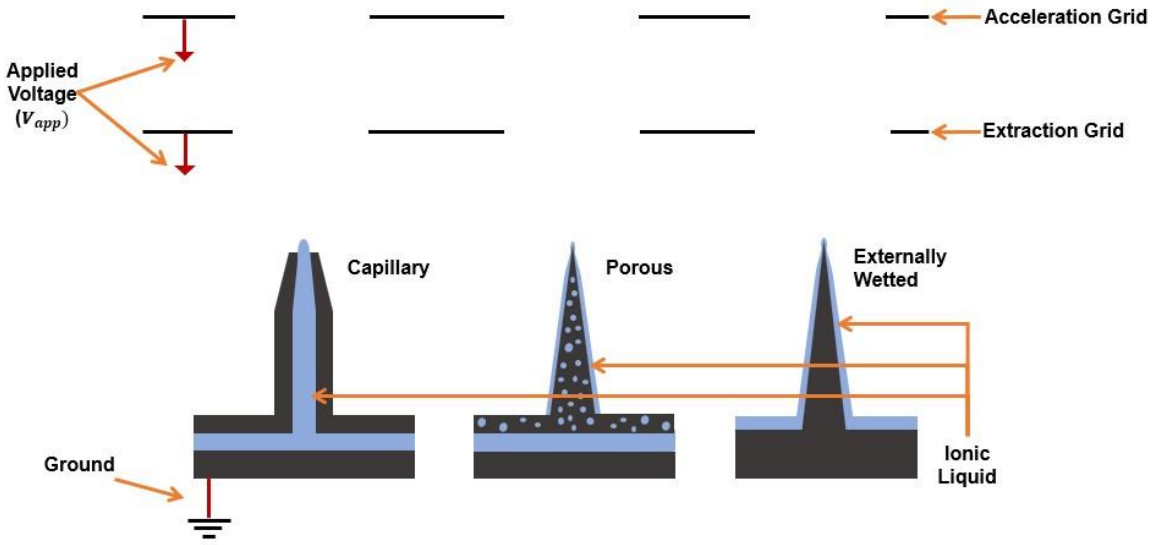

Figure 1.6. Schematics of typical emitter design types.

requirements of the thruster. Therefore, it is important to perform a numerical study to optimize the power supply requirements for the electrospray thruster. This is accomplished by designing an emitter that minimizes the onset voltage requirements. This optimization study is concerned with three electrospray thruster design features: the emitter aspect ratio, electrode erasure during the fabrication of the emitter, and the choice of IL propellant source for the thruster. These are three of the key design features that have an impact on the onset voltage of the electrospray thruster. If knowledge of the power supply requirements as a function of the onset voltage is determined numerically via simulations, an understanding of the optimal design can be gained before fabrication of the emitter has started. This leads to the development of guidelines, or best practices, for designing an electrospray thruster. These design guidelines can then be used as a starting point for construction of electrospray thrusters. This study is performed on a novel electrospray thruster design as proposed by the Micro Scalable Thruster for Adaptive Mission Profiles in Space (μSTAMPS) team at the University of Tennessee Space Institute (UTSI). The goal is to provide a robust emitter design that minimizes power requirements to allow a greater range of versatility for low-thrust electric propulsion technology. This design consists of microcapillary electrospray emitters that are embedded in a dielectric material (borosilicate glass) and open into a cylindrical void, which has been defined as the electrospray cavity. This design feature has been chosen to act as a buffer zone between the IL propellant and the extraction grid to prevent shorting and contamination of the extraction grid by collecting stray IL discharge from the emitter. The extraction grid material is indium tin oxide (ITO) and is deposited onto the top surface of the emitter before the capillaries or electrospray cavities are etched. A key parameter of this emitter design is the electrospray cavity aspect ratio, AR, which is a function of the width and the height of the electrospray cavity, m and d, respectively. AR is unitless, and in this study, is defined as the ratio of $\frac{m}{d}$, where m and d are in units of micrometers (μm). The details of these

parameters will be discussed in greater detail later in this thesis. However, a schematic representing the overall design concept is shown in Figure 1.7 so that some of the features discussed in the literature review can be easily referenced.

1.5 Literature Review of Related Work

This literature review is divided into three subsections. The first subsection is a discussion on the earliest observations and research of the electrospray phenomena. Since this study relies on numerical analysis of an electrospray emitter, the development and comparison of relevant models is also discussed. The literature regarding relationships between variations in emitter geometry (AR and electrode erasure) and onset voltage characteristics is then examined. Finally, the pertinent research into the effects of ILs on onset voltage is considered.

1.5.1 Early Observations and Research of Electrospray Physics

One of the earliest recorded observations of the electrospray phenomena is from the 17th century. William Gilbert observed the phenomena in his works with magnetism. He noticed that water on a dry surface deformed into a cone when a piece of charged amber was placed nearby. As a result of this observation, Gilbert [17] stated that,

> Indeed, it plainly does draw the body itself in the case of a spherical drop of water standing on a dry surface; for a piece of amber applied to it at a suitable distance pulls the nearest parts out of their position and draws it up into a cone.

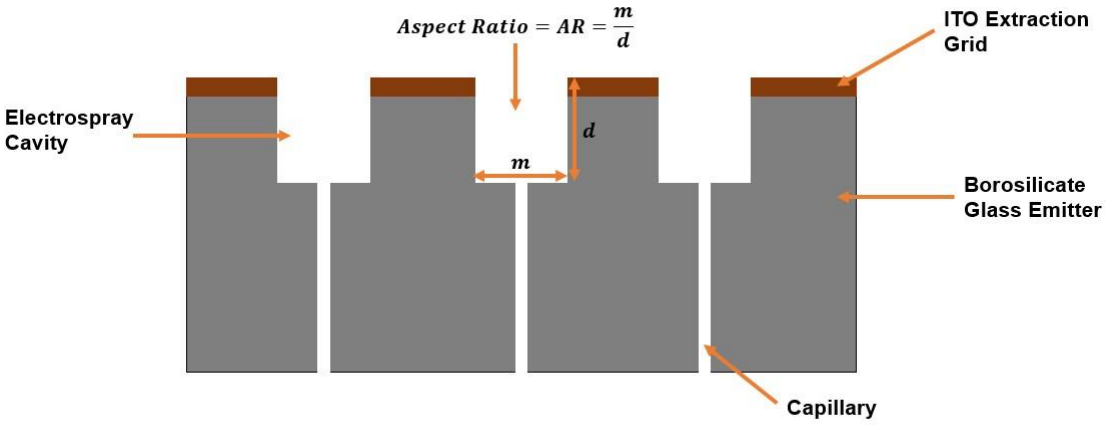

Figure 1.7. Schematic representation of the μSTAMPS novel emitter design.

The underlying physics may have been unknown to Gilbert, but he had observed and described the basis of electrospray phenomena, including what is known today as the Taylor cone.

Although Gilbert may have been one of the first to observe and describe the phenomena behind electrospray, much of the published modern research into this field and its potential applications began with the American physicist John Zeleny in the early 20th -Century. Zeleny's work with conducting liquids and electric fields began in 1914 with his study of the electrical discharge from liquid points [18]. Zeleny had worked previously in 1907 with experiments regarding the electrical discharge from pointed conductors (platinum and brass) of varying sizes [19]. Zeleny's study found that the shapes of the liquid points varied for different levels of applied voltages. After his experimentation with electrical discharge from liquid points, Zeleny then turned to a study of the instability of liquid surfaces that were electrified [20]. During his research, Zeleny witnessed the cone and jet emission of an electrified liquid surface that is characteristic of the electrospray process. Zeleny's work with the instability of electrified liquid points demonstrated one of the major physical phenomena of electrospray physics, what is known today as the Taylor cone. Zeleny's lab assistant was able to capture some of the first photographs of this process, as is shown in Figure 1.8. Zeleny's work would serve as a starting point for further studies by the British physicist, Sir Geoffrey Ingram Taylor, whose name was given to the Taylor cone for his foundational studies of the electrospray phenomena.

Taylor's work with electrospray physics in 1964 built upon the results of Zeleny's work from 1917. After correcting an error in an assumption made by Zeleny, Taylor was able to determine a relationship between the length and equatorial diameter of the liquid for instability to occur, resulting in cone-jet emission. However, one of the most important findings from Taylor's research was

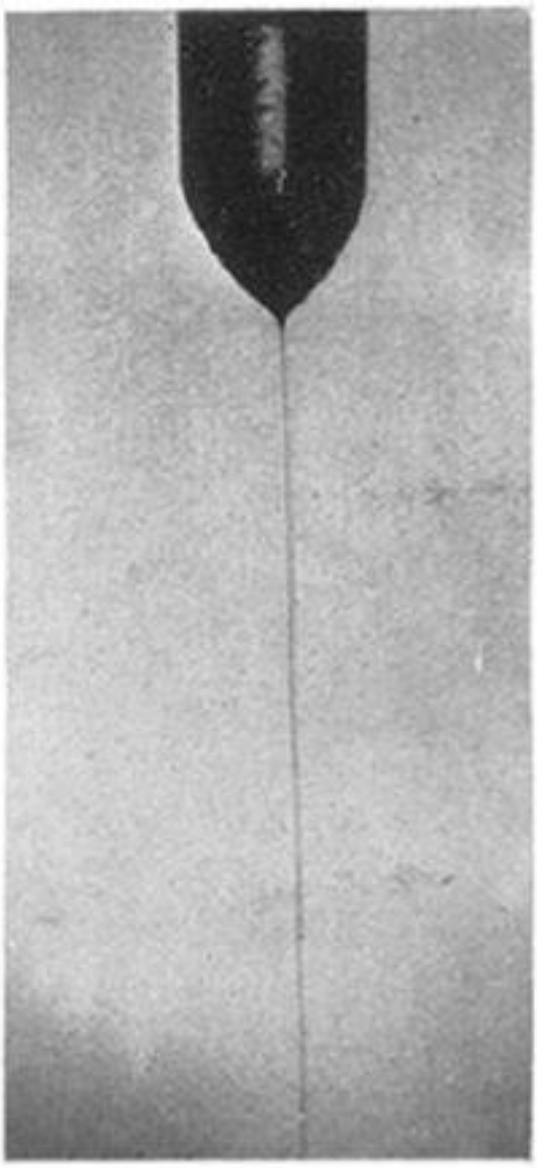

Figure 1.8. Photograph of the Taylor cone and liquid jet from Zeleny's experiments with the instability of electrified liquid surfaces (taken from [20]).

regarding the shape of the liquid that corresponds to equilibrium between the liquid and the electric field. This shape is the Taylor cone and occurs for a conically shaped liquid tip that Taylor determined empirically to correspond to a semi-vertex angle of 49.3°, which is obtained by the solution of a ½-order Legendre function [16]. Taylor, like Zeleny, photographed the successive stages of his experiment showing the evolution of the Taylor cone and cone-jet emission. Figure 1.9 shows a photograph from Taylor's experiment demonstrating the Taylor cone and cone-jet emission.

Now that Taylor had begun to research the electrospray phenomena, he knew that a more thorough treatment of the underlying physics was necessary. This physical description of the relationships explaining fluid behavior under the influence of applied electric fields falls into a branch of physics known as electrohydrodynamics (EHD), which is essentially the union of fluid mechanics and electrodynamics. In EHD, the dynamic currents are small, which renders the magnetic induction negligible. The result of this is an irrotational electric field intensity, which allows the analysis to be simplified to the relations that govern electrostatic behavior. During Taylor's time, applications and research based in EHD were already in existence. However, Taylor understood that there were issues with being able to reproduce experimental results, and a lack of a theoretical framework to accurately describe this branch of physics [21]. With this knowledge in mind, Taylor and American physicist, James Melcher, sought to define a portion of EHD mathematically. Taylor and Melcher confined their study of EHD to fluids with uniform electrical properties and electromechanical coupling at the fluid interfaces. At surface interfaces, the shear stress that arises is very important for the study of fluid behavior in this region.

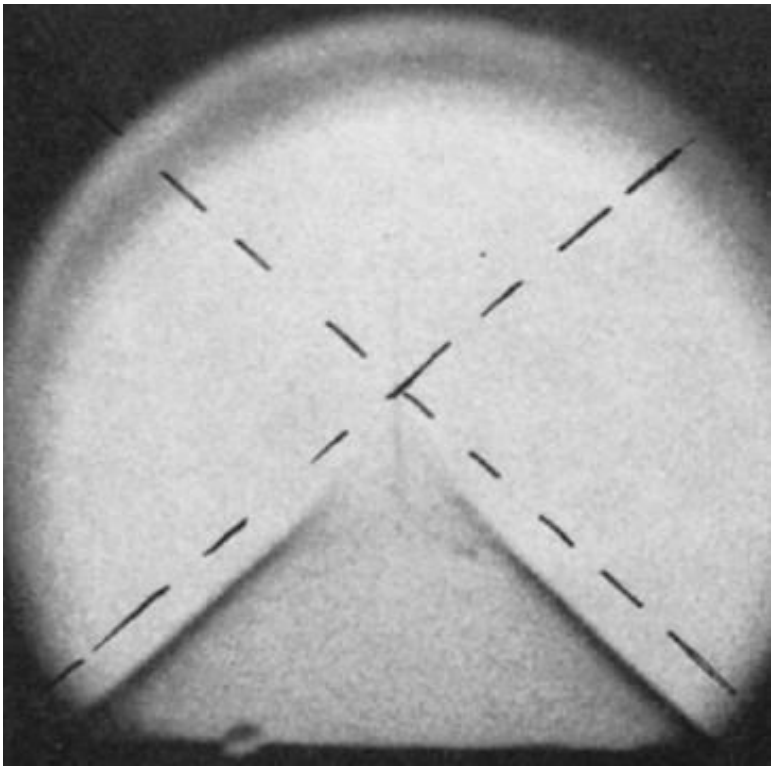

Figure 1.9. Photograph of results from Taylor's work. Note the black chalk markings that distinguish the angle 98.6° which corresponds to twice the semi-vertex angle of 49.3° (taken from [16]).

The model that was used by Taylor and Melcher included the influence of electrical stresses on the fluid but neglected the converse effects of the fluid on the electrical behavior. Several experiments of varying complexity were performed during the study. A key parameter that was used in the study was the electric Reynolds number, R_e. This parameter is defined as a dimensionless time. The electric Reynolds number is the ratio of the charge relaxation time to the characteristic time of the fluid's motion (characteristic velocity over a given characteristic distance). Taylor and Melcher observed the importance of this parameter during their experiments. For very small electric Reynolds numbers ($R_e \ll 1$), the results of their experiments agreed with the theoretical framework. However, as the electric Reynolds number approached values closer to unity, instabilities arose that were not explained by the model. The importance of this result, as noted by Taylor and Melcher, is that there are many phenomena that the model is useful for explaining. However, there are also other physical behaviors at interfaces, such as electrical conduction, that cannot be ignored and are not predicted or accounted for by this model.

1.5.2 Numerical Modeling of Electrospray Physics

As the physics behind the electrospray phenomena is better understood, it is desirable to use this knowledge to design and implement the most effective electrospray device that is possible within practical design limitations. To this end, numerical simulations have been used in better understanding the conditions for optimal performance of electrospray devices. These conditions may include emitter geometry, propellant types, and materials used in the construction of the device. Numerical modeling allows thruster characteristics to be changed and simulated with relative ease. The accuracy of the simulation and its computational cost are important for any numerical analysis of electrospray devices. Presented

below is a summary of the relevant literature related to numerical modeling of electrospray physics.

There has been work in numerical modeling that sought to capture a complete picture of the EHD phenomena. In a 2010 work by López-Herrera, Popinet, and Herrada, a complete simulation of EHD behavior was made that neglected any sort of simplifying assumptions [22]. A lack of simplifying assumptions meant that the EHD solver could handle any type of EHD problem. The solver would require the inclusion of electric forces in the Navier-Stokes equations, and consideration of charge migration due to electric conduction and convection in the charge conservation equation. There are various fluid mechanics solvers in existence; however, a way to integrate the electric forces into the fluid mechanics was required. This analysis used the Gerris solver [23], which utilizes the volume of fluid (VOF) method, to examine EHD physics. To analyze the EHD behavior of the fluid, a special EHD solver was created and used as an extension within the Gerris solver. The solver was then used to test various EHD behaviors of interest and was found to provide accurate results. Most relevant to the focus of this thesis is the simulation of the deformation of liquid droplets under the effects of an applied electric field. This is directly related to the electrospray phenomena and was studied further by some of the same researchers.

In 2012, Herrada, López-Herrera, and Gañán-Calvo studied the numerical simulation of electrospray devices operating in the cone-jet mode under the assumption of steady-state conditions [24]. This study was focused on the comparison of the numerical and experimental shape of the liquid when it is operating in cone-jet mode. The steady-state assumption allowed for simplification of the Navier-Stokes equations that define the fluid motion. The numerical models that were used in this approach were an interface-tracking technique and the VOF method. The interface-tracking method is computationally more affordable than

the VOF method. Results from the interface-tracking method were compared to the more complicated VOF method to determine its accuracy. For the interface-tracking technique, a boundary-fitted coordinate system was used to simplify the computational domain. This allowed a system of equations to be generated that were solved iteratively using a trust-region method. This method was implemented using the built-in MATLAB function FSOLVE. This method was efficient and computational costs were quite low (on the order of one hour for all cases). The second numerical approach used the Gerris solver that had been utilized previously in work by López-Herrera et al. [22]. The VOF solution was more computationally expensive and required a running time of around seventy-two hours. Both methods agreed well with the experimental data, which indicates that the less computationally expensive interface-tracking method can be used without introducing large errors to the analysis. Another important result of this study was the ability to determine the current transmitted by the liquid jet by using a scaling law determined in previous work by Gañán-Calvo [25]. This work with the comparison of experimental results and scaling laws deserves more discussion because of its importance with regards to work by other authors.

In 1996, Gañán-Calvo, Dávila, and Barrero performed experiments to test whether a set of scaling laws that they derived from charge transport theory could be used to estimate the droplet size and current of electrospraying liquids operating in the cone-jet mode [26]. The research team was able to determine a set of dimensionless parameters that were used to determine the conditions where certain equations could be used to describe the behavior of the conducting liquid. This is analogous to how the Reynolds number is used to determine fluid flow regimes, which then allow a given relationship to be used to determine flow characteristics. These dimensionless parameters describe the magnitudes of the fluid conductivities and viscosities where certain theoretical relationships remain valid. Two relationships were developed: one that is appropriate for fluids with

large conductivities and viscosities, while the other is valid for fluids with smaller conductivities and viscosities. Both relationships were shown to agree well with the experimental data that was collected, and the results have been used in other studies as validations for their numerical models.

A later study based on the experimental results of the 1996 work by Gañán-Calvo et al. [26] was performed by Lastow and Balachandran in 2006 [27]. This work was very similar to the study performed by López-Herrera et al. [22], except for the numerical solver that was used and the method for coupling the EHD and fluid mechanics. Lastow and Balachandran chose a computational fluid dynamics (CFD) solver, Ansys CFX 4.4 [28], that could handle free-surface problems. With regards to coupling the EHD and fluid mechanics, Lastow and Balachandran modified the built-in heat conduction equation to solve the electrostatic field equations instead. Their simulation did not account for any current and did not include a model for droplet break-up. A similar experimental set up to the one used by Gañán-Calvo et al. [26] was used to validate the model. The experimental results agreed well with the CFD model and were also in good agreement with the results determined by Gañán-Calvo et al. [26].

Several studies have been performed to analyze the voltage required for onset of electrospray. In 1986, David Smith performed a study to begin modeling the behavior of steady-state electrospray operation (cone-jet mode) [29], that Zeleny first observed [20]. Smith restricted his study to needle-like electrospray emitters that closely resembled experiments performed by Zeleny [20], or what are now known as capillary-type emitters (see Figure 1.6). At the time, no suitable model existed to describe the electric field intensity in the region near the tip of the Taylor cone required for electrospray onset to begin. Smith developed a model of the form

$$V_0 = A_1\sqrt{\frac{2\gamma r_c \cos(\theta_0)}{\varepsilon_0}}\ln(\frac{4d}{r_c}). \quad [1.3.1]$$

This model was adapted from a form previously suggested by Taylor in Reference [16]. The variables and constants in the above equation are the onset voltage, V_0 in units of volts (V), an empirical constant, A_1, which has an optimal value that is determined experimentally, the surface tension coefficient, γ, in units of newtons per meter (N/m), capillary radius, r_c, in units of μm, the cone half angle, θ_0, in degrees (°), the constant vacuum permittivity, ε_0, in farads per meter (F/m), and the emitter to extraction grid distance, d, in μm. This form is important to the current research because it relates three important parameters: the surface tension, extraction grid distance from the emitter, and the capillary radius. This form was also adopted by Ikonomou, Blades, and Kebarle in a 1991 study [30]. After performing an experiment which was similar in nature to Smith's [29], Ikonomou et al. found that the experimental data was predicted reliably by equation [1.3.1].

Examining the full EHD behavior using commercial solvers can be computationally expensive and may not yield parameters of interest, depending on the electrospray properties being examined, i.e., the onset voltage in this study. Using empirical models to compare and correlate experimental results requires the fabrication of a test apparatus and emitter arrays. This can lead to expenses that may yield results which are not useful, or only apply to certain situations. Thus, it is desirable to develop a model to analyze the onset voltage so that an optimal electrospray emitter design can be tested for a reasonable computational expense before testing the emitter in the laboratory. A simplified model for determining onset voltage for electrospray emitters was suggested by Krpoun and Shea in 2008 [31]. This study is important since it forms the basis for determining the onset voltage in this study. The physical intricacies of this method and their application

to this project will be discussed in Chapters 2 and 3. As mentioned before, this model allows for a much quicker method for determining onset voltage without a loss in the accuracy of the result. Another benefit of this model is the fact that both simple and complex geometries can be handled. Because this model assumes a quasistatic evolution of the Taylor cone, the liquid surface and capillary are considered equipotential surfaces. Another assumption of the model is that the onset voltage occurs at the immediate onset of cone-jet operation and there is no net space charge. The model begins by assuming a shape for the Taylor cone and then calculating the electric field strength at the tip of the cone. The physical model, which will be explained in Chapter 2, is then used to calculate the voltage. The sharpness of the cone is gradually increased with each simulation until the voltage has reached a steady-state value, which is defined as the onset voltage. This method is useful for determining the steady-state onset voltage. Krpoun and Shea showed that this model had excellent agreement with experimental onset voltages of the electrospray emitters that they compared.

However, there are other phenomena that are not observable by using this method, such as the transients during startup and shutdown. Phenomena like space charge are also neglected, which has an impact on the efficiency of electrospray emitters beyond cone-jet mode operation.

1.5.3 Effects of Electrospray-Cavity Aspect Ratio on Onset Voltage

The next section of literature that will be reviewed is research into the effects of geometrical variations on the onset voltage of electrospray emitters. Since the electrospray emitter detailed in this report is of a novel design, the literature does not include many studies with which to compare it. Geometries and aspect ratios have been examined in the literature; however, usually the goal is to understand other performance parameters and not the onset voltage. The studies of Ryan et

al. (2009 and 2012) [32, 33], yielded interesting results on the effects of electrospray emitter geometry on their operation. The goal of both studies was to examine the volumetric flow rate sensitivity to the applied voltage of the system based on variations in capillary geometry. It was found that there is a relationship between the volumetric flow rate sensitivity to applied voltage and the geometry of the capillary. In particular, it was found that the flow rate sensitivity to applied voltage increased for capillaries with smaller outer diameters [32], which was also confirmed in their later study [33]. As understanding of this phenomenon is increased, it could lead to increased control over the variability of thrust for electrospray thrusters.

More relevant to the work at hand is a 2020 study by Jones et al., in which variations of emitter geometry and constituent materials were used to analyze the onset voltage of the proposed emitter. This study used the numerical model developed by Krpoun and Shea to examine how the onset voltage varied with different geometrical designs and material properties [34]. This design consists of a capillary emitter embedded in a dielectric material. This design is more robust, as the emitter is embedded within a dielectric material instead of protruding from a substrate into the operational environment. Jones et al. used the Maxwell toolkit with the electromagnetic solver, Ansys Electronics Desktop (EDT), to perform the simulations in the study [28]. The goal of the study was to examine the variations of the onset voltage for changes in several key geometrical and material variations. The geometrical variations studied were the dielectric thickness, h_e in μm (equivalent to the emitter height of this study), capillary radius, distance between the emitter and extraction grid, and for emitter arrays, the pitch, p in μm, between emitters. Along with these geometric parameters, the dielectric material was varied to examine the influence of the dielectric constant on the onset voltage. Jones et al. determined several design choices that could help optimize the onset voltage. Emitter heights greater than 300 microns (μm) should be used so that the

emitter can escape shielding effects of the surrounding electric fields. Small capillary radii with a pitch-to-emitter-height ratio of greater than 2.5 should be used. A small distance between the emitter and extraction grid also allows for a more optimal onset voltage. Finally, emitter materials with the lowest possible dielectric constant will result in lower onset voltages. The numerical model used by Jones et al. is important to this work because this method will be used to determine onset voltage values in this thesis.

Most studies of emitter aspect ratios have dealt with capillary- or needle-type emitters (externally wetted and/or porous). Much of the research is concerned with improved efficiency for mass spectrometry, which is another application of the electrospray phenomenon. This includes studies such as the work performed by Kelly et al. [35]. There are some interesting results in the literature, however, that pertain to electric propulsion applications. Ticknor et al. examined the effects of aspect ratio on the performance of both externally fed and porous needle emitters [36]. Ticknor et al. discovered that emitters with higher aspect ratios (higher needle length to diameter), had a decreased propellant flow rate. This meant that shorter needles provided electrospray plumes that were mostly mixed ion and liquid sprays, while the higher aspect ratio needles operated more closely to the purely ionic regime. Another important finding that is more directly related to the work at hand is that of Guerra-Garcia et al. [37]. Guerra-Garcia et al. studied the uniformity of the current that was emitted by an array of electrospray emitters. Guerra-Garcia et al. discovered that for a low-enough applied voltage, not all of the emitters in the array were operating in cone-jet mode. Some emitters were not firing at all, which is an indication that the onset voltage was not high enough for those particular emitters. Guerra-Garcia et al. explained that this behavior was a result of nonuniformity between individual emitter geometry as a result of the fabrication process. Another important finding was that hotspots occurred for the emitters that fired early as a result in the increased potential requirement to allow the other

emitters to fire. Therefore, this result indicates a direct relationship between geometrical parameters, including aspect ratio, to the onset voltage for a given emitter. In particular, nonuniformity in the design of electrospray emitters can lead to shortened thruster lifespans.

1.5.4 ITO Extraction Grid Erasure

The emitter capillary and electrospray cavity geometries studied in this thesis are fabricated using ultrafast laser machining [38] of borosilicate glass with a deposited coating of ITO. As a consequence of the machining process, portions of the ITO may be erased in a small region extending in a radial direction from the cavity rim. This effectively removes a portion of the ITO extraction grid which can have an effect on emitter operation. This consequence of the manufacturing process is defined as extraction-grid erasure for the purpose of this study. Figure 1.10 displays the effects of extraction grid erasure on the emitter chip. Although not directly related to electrospray-thruster emitter chips, related phenomena have been reported in the literature [39, 40]. In fact, to the author's knowledge, there has been no literature dedicated to the impact of electrode erasure on electrospray-emitter onset voltage.

1.5.5 Ionic Liquid Comparison

Since ILs are the primary propellant choice for electrospray thrusters, it is important to choose an IL with physical properties that can be used to achieve lower onset voltages. Studies exist where the onset voltage of a small selection of ILs have been recorded. For example, Ma et al. [41] performed a study in which the onset voltages, emission currents, and other plume characteristics were identified for several porous emitter designs. Ma et al. considered only a single IL, 1-ethyl-3-methylimidazolium tetrafluoroborate (EMI-BF4), in their study [41].

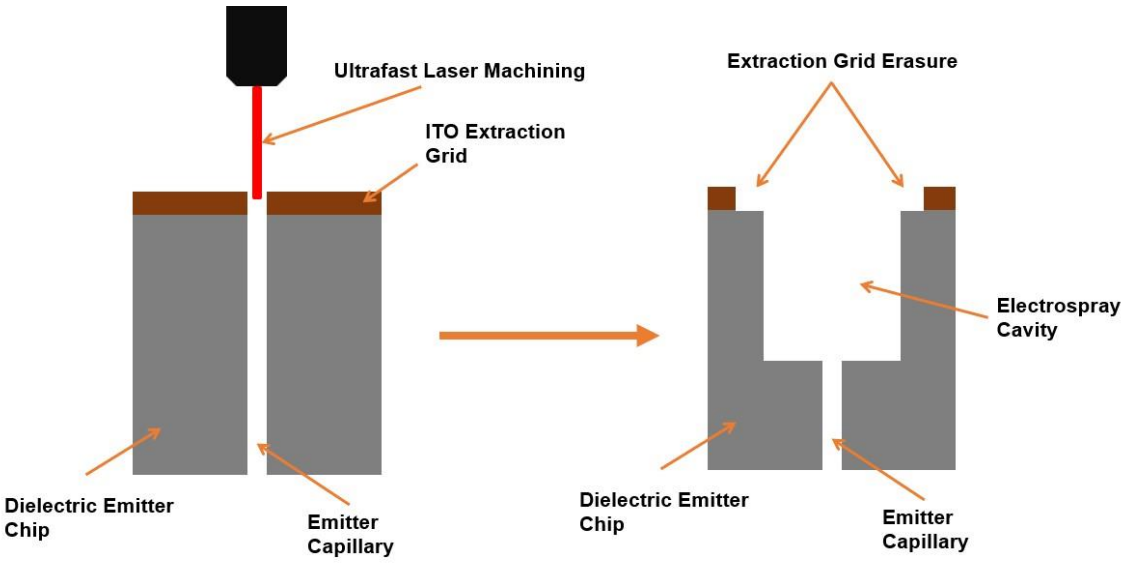

Figure 1.10. Extraction grid erasure as a side-effect of ultrafast-laser machining.

Huang et al. [42] experimentally studied current modes of porous electrospray thrusters which also documented the onset voltage characteristics of the thruster. Although much useful information was gained from these studies, their main goal was not to specifically measure onset voltage differences between IL-propellant sources.

Most relevant to the work performed here are the results of another study by Huang et al. [43]. Huang et al. used a porous emitter array to characterize the electrospray process for three different ILs. Important to this study is the onset voltage, which was one of the characteristics that were measured by Huang et al. [43]. While not solely focused on comparison of onset voltage differences in ILs, the selection of various ILs is more similar to the work presented here than the previous two studies mentioned above. Even more importantly, two of the ILs used by Huang et al. are also considered in this study. The ILs used in their study were EMI-BF4, 1-ethyl-3-methylimidazolium bis(trifluoromethylsulfonyl)imide (EMI-Im), and 1-butyl-3-methylimidazolium hexafluorophosphate (BMI-PF6), which had corresponding onset voltages of 740 V, 800 V, and 1120 V, respectively [43]. EMI-BF4 and EMI-Im are used in the study presented here for the embedded dielectric emitters and the onset voltage results will be compared with the results of Huang et al. in Chapter 4.

1.6 Organization

The relevant background information and related literature have been presented thus far. The remainder of this thesis will focus on the underlying physics of electromagnetics and fluid mechanics (Chapter 2), a detailed discussion of the methodology used in collecting and analyzing the information presented in this study (Chapter 3), a discussion of the results obtained from this work (Chapter 4), a section to discuss the implications of the results and what future work might

be performed as next steps in the development of this novel thruster (Chapter 5), and finally, a list of References.

CHAPTER 2: PHYSICAL BACKGROUND

The operation of electrospray devices is dependent on the effects of electromagnetic forces upon liquid propellants. This electrohydrodynamic behavior is governed by the physics of both fluid dynamics and electromagnetics. Fluid dynamics can be represented by the conservation equations (energy, mass, and momentum), along with an equation of state. Maxwell's equations are representative of the underlying electromagnetic behavior in electrospray devices. The full sets of equations are presented in the following two sections. However, simplifications based on assumptions made in this study are introduced in a later section that greatly aid in the simplification of the computational and electrohydrodynamics models used. The development of the fluid dynamics and electromagnetics governing equations can be found in many textbooks on the subject. The author recommends References [44] and [45] for a complete treatment of the development of the fluid dynamics and electromagnetic governing equations, respectively.

2.1 Fluid Dynamics Governing Equations

The behavior of fluid in motion is governed by the equations of fluid dynamics. These equations are the continuity equation (conservation of mass), the conservation of momentum, and the conservation of energy.

The conservation of momentum is given by

$$\frac{\partial(\rho \boldsymbol{u})}{\partial t} + \nabla \cdot (\rho \boldsymbol{u} \cdot \boldsymbol{u}) + \nabla P = \nabla \cdot \bar{\bar{\boldsymbol{\tau}}} + \rho \boldsymbol{b}. \qquad [2.1.1]$$

where ρ is the fluid density in kilogram per cubic meter (kg/m^3), $\boldsymbol{u}$ is the fluid velocity vector in meters per second (m/s), P is the pressure in pascals (Pa), $\bar{\bar{\boldsymbol{\tau}}}$ is the viscous stress tensor, also in pascals (Pa), and $\boldsymbol{b}$ represents body forces at work on the fluid. Note that all body forces are in units of newtons per cubic meter (N/m^3). This form of the conservation of momentum is also known as the conservation form of the Cauchy momentum equation.

The continuity equation is represented by

$$\frac{\partial \rho}{\partial t} + \nabla \cdot (\rho \boldsymbol{u}) = 0, \qquad [2.1.2]$$

with u being the velocity vector of the fluid.

Excluding any generation terms, the energy equation can be written as

$$\frac{\partial \rho\left(\frac{1}{2}v^2 + U_i\right)}{\partial t} = -\nabla \cdot \rho \boldsymbol{u}\left(\frac{1}{2}v^2 + U_i\right) - (\nabla \cdot \boldsymbol{q}) - P(\nabla \cdot \boldsymbol{u}) - \nabla \cdot (\bar{\bar{\boldsymbol{\tau}}}\boldsymbol{u}) + \rho \boldsymbol{b} \cdot \boldsymbol{u}, \qquad [2.1.3]$$

where v is the scalar velocity of the bulk fluid in meters per second (m/s), U_i is the internal energy per unit mass in joules per kilogram (J/kg), and $\boldsymbol{q}$ is the heat flux vector in watts per square meter (W/m^2). The term $\left(\frac{1}{2}v^2 + U_i\right)$ is called the total energy, U, with units of joules (J). The term $\boldsymbol{q}$ can be written as $-k\nabla T$ by Fourier's law, where k is the scalar (for isotropic materials) thermal conductivity in watts per meter-kelvin (W/m-K), and T is the temperature in kelvin (K). With this in mind, Equation [2.1.3] can be written as

$$\frac{\partial (\rho U)}{\partial t} = -\nabla \cdot \rho U \boldsymbol{u} + k(\nabla^2 T) - \nabla \cdot (P\boldsymbol{u}) - \nabla \cdot (\bar{\bar{\boldsymbol{\tau}}}\boldsymbol{u}) + \rho \boldsymbol{b} \cdot \boldsymbol{u}. \qquad [2.1.4]$$

Finally, the ideal gas law is a commonly used equation of state in fluid dynamics. The form most commonly used is given by

$$P = \rho RT, \qquad [2.1.5]$$

where the constant, R, is the specific gas constant of the gas under consideration in joules per kilogram-kelvin (J/kg-K).

Equations [2.1.1] – [2.1.5] are necessary to explain the behavior and motions of the fluids that are being acted upon by electromagnetic forces. However, none of the above equations takes into consideration the effects of surface tension between two fluids at their interface. This is a necessary consideration and requires the inclusion of surface tension effects at the interfacial boundary of the two fluids. As this work builds on the foundation of Jones et al. [34], the same surface tension terms will be included in the interfacial boundary conditions. This representation is taken from the 1990 work on continuum methods for modeling surface tension by Brackbill, Kothe, and Zemach [46]. Brackbill et al. gave the surface stress boundary condition at the fluid-fluid interface as

$$(P_1 - P_2 + \gamma\kappa)\boldsymbol{n} = (\bar{\bar{\tau}}_1 - \bar{\bar{\tau}}_2)\boldsymbol{n} + \nabla \cdot \gamma, \qquad [2.1.6]$$

with P_1 and P_2 defined as the pressures at interfaces 1 and 2 respectively, κ being the local curvature of the surface at the fluid-fluid interface with units of inverse meters (1/m), $\bar{\bar{\tau}}_1$ and $\bar{\bar{\tau}}_2$ are the viscous stress tensors at interfaces 1 and 2 respectively, and $\boldsymbol{n}$ is the unit normal vector. Equation [2.1.6] asserts that the surface stresses at the fluid-fluid interface are balanced. Since Equation [2.1.6] is from a study that is mainly concerned with the fluid dynamics aspect of fluid-fluid

interfaces, there is no inclusion of body forces that are electromagnetic in nature. With the addition of the body force term, Equation [2.1.6] can be written as

$$(P_1 - P_2 + \gamma\kappa)\boldsymbol{n} = (\bar{\bar{\tau}}_1 - \bar{\bar{\tau}}_2)\boldsymbol{n} + \nabla \cdot \gamma + \rho\boldsymbol{b}. \qquad [2.1.7]$$

Since this study is concerned with the effects of electromagnetic body forces on the fluid-fluid interface, the body force term, $\rho\boldsymbol{b}$, can be written as the electromagnetic body force, $\boldsymbol{b}_s^{EM}$, yielding

$$(P_1 - P_2 + \gamma\kappa)\boldsymbol{n} = (\bar{\bar{\tau}}_1 - \bar{\bar{\tau}}_2)\boldsymbol{n} + \nabla \cdot \gamma + \boldsymbol{b}_s^{EM}. \qquad [2.1.8]$$

It is worth noting that depending on the circumstances of operation, additional body force terms may be required to account for gravitational acceleration or other such physical interactions which will be discussed in more detail in a subsequent section. The governing equations of fluid dynamics are collected in Table 2.1 for convenience.

Along with the governing equations of fluid dynamics, the governing electromagnetic equations must be considered to understand the operation of electrospray devices. The following section details the electromagnetics background required to further discuss electrospray device operation.

2.2 Electromagnetics Governing Equations

The physics of the electromagnetics that govern the electrospray phenomena can be fully represented by Maxwell's equations. Gauss's law in terms of the free charge density, q, is given by the divergence of the electric displacement field, $\boldsymbol{D}$:

Table 2.1. Fluid dynamics governing equations.

Fluid Dynamics Governing Equations		
Conservation of Momentum	$\frac{\partial(\rho \boldsymbol{u})}{\partial t} + \nabla \cdot (\rho \boldsymbol{u} \cdot \boldsymbol{u}) + \nabla P = \nabla \cdot \bar{\bar{\boldsymbol{\tau}}} + \rho \boldsymbol{b}$	[2.1.1]
Continuity	$\frac{\partial \rho}{\partial t} + \nabla \cdot (\rho \boldsymbol{u}) = 0$	[2.1.2]
Conservation of Energy	$\frac{\partial(\rho U \boldsymbol{u})}{\partial t} = -\nabla \cdot \rho U \boldsymbol{u} + \boldsymbol{k}(\nabla^2 T) - \nabla \cdot (P \boldsymbol{u}) - \nabla \cdot (\bar{\bar{\boldsymbol{\tau}}} \boldsymbol{u}) + \rho \boldsymbol{b} \cdot \boldsymbol{u}$	[2.1.4]
Equation of State	$P = \rho R T$	[2.1.5]
Surface Stress Boundary Condition	$(P_1 - P_2 + \gamma \kappa)\boldsymbol{n} = (\bar{\bar{\tau}}_1 - \bar{\bar{\tau}}_2)\boldsymbol{n} + \nabla \cdot \gamma + \boldsymbol{b}_s^{EM}$	[2.1.8]

$$\nabla \cdot \boldsymbol{D} = q, \qquad [2.2.1]$$

where ∇ is the nabla, or del operator, with q and $\boldsymbol{D}$ having units of coulombs per cubic meter (C/m^3) and coulombs per square meter (C/m^2), respectively. Gauss's law for magnetism is the statement that magnetic monopoles do not exist, or equivalently the divergence of the magnetic flux density, $\boldsymbol{B}$, is equal to zero:

$$\nabla \cdot \boldsymbol{B} = 0. \qquad [2.2.2]$$

In Equation [2.2.2], the magnetic flux, $\boldsymbol{B}$, is given in units of teslas (T).

The Ampère-Maxwell equation relates the magnetic field intensity, $\boldsymbol{H}$, about a closed loop induced by the flowing electric displacement field, $\boldsymbol{D}$, within the loop and the free current density, $\boldsymbol{J}$. Mathematically, this statement is that the curl of the magnetic field intensity is equal to the free current density plus the time rate of change of the electric displacement field, or:

$$\nabla \times \boldsymbol{H} = \boldsymbol{J} + \frac{\partial \boldsymbol{D}}{\partial t}, \qquad [2.2.3]$$

where $\boldsymbol{H}$, $\boldsymbol{D}$, and $\boldsymbol{J}$, are in units of amps per meter (A/m), coulombs per square meter (C/m^2), and amps per square meter (A/m^2), respectively. The term, $\frac{\partial \boldsymbol{D}}{\partial t}$, in Equation [2.2.3] is defined as the displacement current.

The Maxwell-Faraday equation rounds out the set of Maxwell's equations. This equation, also known as Faraday's law of induction, describes the electric field induced by a time-varying magnetic field, i.e., magnetic induction. The Maxwell-Faraday equation states that the curl of the electric field, $\boldsymbol{E}$, is equal to the negative of the time rate of change of the magnetic flux:

$$\nabla \times \boldsymbol{E} = -\frac{\partial \boldsymbol{B}}{\partial t}, \qquad [2.2.4]$$

with $\boldsymbol{E}$ having units of volts per meter (V/m). Maxwell's equations (Equations [2.2.1] – [2.2.4]) are collected in Table 2.2 for reference.

The magnetic field intensity, $\boldsymbol{H}$, and the electric field, $\boldsymbol{E}$, can be related to the magnetic flux, $\boldsymbol{B}$, and electric displacement field, $\boldsymbol{D}$, respectively, by the constitutive equations:

$$\boldsymbol{B} = \mu_0(\boldsymbol{H} + \boldsymbol{M}), \qquad [2.2.5]$$

and

$$\boldsymbol{D} = \varepsilon_0 \boldsymbol{E} + \boldsymbol{P}, \qquad [2.2.6]$$

where μ_0 is the permeability of free space in henries per meter (H/m), $\boldsymbol{M}$ is the magnetization in amperes per meter (A/m), and $\boldsymbol{P}$ is the polarization in coulombs per square meter (C/m^2).

In many circumstances, such as the optical responses of nonlinear materials, the behavior of the polarization field and the magnetization is quite complicated. However, for the case of the dielectric media used in this work, a linear relationship can be assumed, thus simplifying the relevant equations. This yields the following relationship between the magnetization, $\boldsymbol{M}$, and the magnetic field intensity, $\boldsymbol{H}$:

$$\boldsymbol{M} = \overline{\overline{\chi_m}}\boldsymbol{H}, \qquad [2.2.7]$$

Table 2.2. Maxwell's Equations.

Maxwell's Equations		
Gauss's Law	$\nabla \cdot \boldsymbol{D} = q$	[2.2.1]
Gauss's Law for Magnetism	$\nabla \cdot \boldsymbol{B} = 0$	[2.2.2]
Ampère-Maxwell Equation	$\nabla \times \boldsymbol{H} = \boldsymbol{J} + \frac{\partial \boldsymbol{D}}{\partial t}$	[2.2.3]
Maxwell-Faraday Equation	$\nabla \times \boldsymbol{E} = -\frac{\partial \boldsymbol{B}}{\partial t}$	[2.2.4]

where $\overline{\overline{\chi_m}}$ is defined as the magnetic susceptibility tensor. Likewise, the electric field, $\boldsymbol{E}$, and the polarization, $\boldsymbol{P}$, are related by:

$$\boldsymbol{P} = \varepsilon_0 \overline{\overline{\chi_e}} \boldsymbol{E}, \qquad [2.2.8]$$

where $\overline{\overline{\chi_e}}$ is defined as the electric susceptibility tensor. The magnetic and electric susceptibility tensors are both unitless (--) when the linear approximation for dielectric media is assumed.

Equations [2.2.7] and [2.2.8] can be substituted into Equations [2.2.5] and [2.2.6], respectively, which results in

$$\boldsymbol{B} = \mu_0 \boldsymbol{H} (\delta_{ij} + \overline{\overline{\chi_m}}), \qquad [2.2.9]$$

and

$$\boldsymbol{D} = \varepsilon_0 \boldsymbol{E} \left(\delta_{ij} + \overline{\overline{\chi_e}}\right), \qquad [2.2.10]$$

where δ_{ij} is the Kronecker delta and is used to ensure valid addition of unity to the susceptibility tensors.

The absolute permittivity and permeability of any arbitrary material or medium are themselves tensors ($\bar{\bar{\varepsilon}}$ and $\bar{\bar{\mu}}$, respectively) and are defined as

$$\bar{\bar{\varepsilon}} = \varepsilon_0 (\delta_{ij} + \overline{\overline{\chi_e}}), \qquad [2.2.11]$$

and

$$\bar{\bar{\mu}} = \mu_0(\delta_{ij} + \overline{\overline{\chi_m}}). \quad [2.2.12]$$

As mentioned above, the nature of the permittivity, permeability, electric susceptibility, and magnetic susceptibility tensors can be quite complicated. However, this work focuses on materials that are isotropic, resulting in the tensors of Equations [2.2.11] and [2.2.12] becoming scalars. This simplifies the terms $\left(\delta_{ij} + \overline{\overline{\chi_e}}\right)$ and $(\delta_{ij} + \overline{\overline{\chi_m}})$ in Equations [2.2.11] and [2.2.12] to become $(1 + \chi_e)$, and $(1 + \chi_m)$. These two terms are defined as relative permittivity and relative permeability, respectively, and are given by

$$\varepsilon_r = (1 + \chi_e), \quad [2.2.13]$$

and

$$\mu_r = (1 + \chi_m), \quad [2.2.14]$$

where ε_r, μ_r, χ_e, and χ_m are the scalar relative permittivity, scalar relative permeability, electric susceptibility, and magnetic susceptibility, respectively. Thus, Equations [2.2.11] and [2.2.12] can be written as

$$\varepsilon = \varepsilon_0\varepsilon_r, \quad [2.2.15]$$

and

$$\mu = \mu_0\mu_r. \quad [2.2.16]$$

ε, and μ are the absolute permittivity, with units of farads per meter (F/m) and absolute permeability with units of henries per meter (H/m), respectively. The

relative permittivity and permeability are often expressed in terms of the ratio of their absolute to vacuum values, resulting in

$$\varepsilon_r = \frac{\varepsilon}{\varepsilon_0}, \qquad [2.2.17]$$

and

$$\mu_r = \frac{\mu}{\mu_0}. \qquad [2.2.18]$$

Thus, by assuming linear relationships between $\boldsymbol{M}$ and $\boldsymbol{H}$, and $\boldsymbol{P}$ and $\boldsymbol{E}$, and isotropic media, the constitutive equations ([Equations [2.2.5] and [2.2.6]) can be expressed as

$$\boldsymbol{B} = \mu_0 \mu_r \boldsymbol{H}, \qquad [2.2.19]$$

and

$$\boldsymbol{D} = \varepsilon_0 \varepsilon_r \boldsymbol{E}. \qquad [2.2.20]$$

Finally, by use of Equations [2.2.17] and [2.2.18], the constitutive equations take the form of

$$\boldsymbol{B} = \mu \boldsymbol{H}, \qquad [2.2.21]$$

and

$$\boldsymbol{D} = \varepsilon \boldsymbol{E}. \qquad [2.2.22]$$

Thus, the physics of the electromagnetic phenomena is fully described by Maxwell's equations and the simplified constitutive relations.

Another useful equation for describing the physics of electrospray devices, which is to be discussed in the next section, is the charge conservation equation. The charge conservation equation is obtained from taking the divergence of the Ampère-Maxwell equation (Equation [2.2.3]) from Maxwell's equations which yields

$$\nabla \cdot (\nabla \times \boldsymbol{H}) = \nabla \cdot \boldsymbol{J} + \frac{\partial(\nabla \cdot \boldsymbol{D})}{\partial t}. \quad [2.2.23]$$

However, since the divergence of the curl of any vector is identically zero and the divergence of the electric displacement is the free charge density, q, then Equation [2.2.23] becomes

$$\frac{\partial q}{\partial t} + \nabla \cdot \boldsymbol{J} = 0. \quad [2.2.24]$$

Since the physics of electrospray devices occur at interfacial areas of differing media, considerations must be taken when dealing with electromagnetic properties at these interfaces. These considerations are given by the following interfacial boundary conditions [47]:

$$E_{t1} = E_{t2}, \quad [2.2.25]$$

$$D_{n1} - D_{n2} = q_s, \quad [2.2.26]$$

$$H_{t1} - H_{t2} = K, \quad [2.2.27]$$

and

$$B_{n1} = B_{n2}. \quad [2.2.28]$$

The subscripts t and n refer to the tangential and normal vector components, respectively. The subscripts 1 and 2 denote the two unique media for which the interface exists. Note that Equations [2.2.25] – [2.2.28] are for any two arbitrary media. However, Equations [2.2.26] and [2.2.27] also account for a surface charge density, q_s in coulombs per square meter (C/m^2), and a linear current density sheet of infinitesimal thickness, K, in amperes per meter (A/m), respectively.

2.3 Application of Physics to Electrospray Devices

The governing equations of Sections 2.1 and 2.2 can be quite cumbersome to attempt a complete solution. However, since the parameter of interest in this study was the onset voltage, many simplifications can be made to the governing equations of fluid dynamics and electromagnetics to facilitate a more economic computational cost. This section details some of these assumptions and how a notable model from the literature used them to predict the onset voltage of electrospray emitters. These assumptions and the corresponding modeling methods are the electrohydrodynamic model, quasi-static evolution, and the parametric modeling of the Taylor cone shape.

2.3.1 Electrohydrodynamic Model

Considering that the electrospray device under consideration in this study used an IL as its propellant, the assumption of an incompressible fluid can be used [48]. This assumption fits well in this case and for other electrospray devices for which the propellant can be considered an incompressible fluid. An

incompressible fluid has a density that can be considered invariant, allowing for the continuity equation (Equation [2.1.2]) to be reduced to

$$\nabla \cdot \boldsymbol{u} = 0. \qquad [2.3.1]$$

As a consequence of constant density, the momentum equation (Equation [2.1.1]) can be written as

$$\rho \frac{\partial(\boldsymbol{u})}{\partial t} + \rho \nabla \cdot (\boldsymbol{u} \cdot \boldsymbol{u}) + \nabla P = \nabla \cdot \bar{\bar{\boldsymbol{\tau}}} + \rho \boldsymbol{b}, \qquad [2.3.2]$$

where the density constant is placed in front of all terms involving rates of change or gradients. The constant-density assumption also further serves to simplify the governing equations, because the dynamics of the flow and the thermodynamics have been decoupled. Therefore, the energy equation (Equation [2.1.3]), and equation of state (Equation [2.1.5]) are no longer necessary for fluid dynamics analyses.

The next step in the hydrodynamic model examines the simplifications that can be made to the electromagnetics governing equations. From the EHD model set forth by Taylor and Melcher [21], Saville [49] has related useful simplifications that can greatly simplify the electromagnetic governing equations. Essentially, electric, and magnetic behaviors can be assigned characteristic times in seconds (s). This characteristic time is based on the absolute permittivity and absolute permeability values of the media under consideration in relation to the vacuum values. A comparison of these characteristic times allows for the decoupling of the electric and magnetic behaviors. This results in the ability to perform an electrostatic analysis that greatly simplifies the solution process. The characteristic relaxation time for electric behavior, τ_E, is given by

$$\tau_E = \frac{\varepsilon_r \varepsilon_0}{\sigma}. \quad [2.3.3]$$

In Equation [2.3.3], σ is the electric conductivity in siemens per meter (S/m). Similarly, the characteristic relaxation time for magnetic behavior, τ_M, is

$$\tau_M = \mu_r \mu_0 \sigma l^2, \quad [2.3.4]$$

where l is the characteristic length, which for the purposes of the electrospray device considered in this study is on the order of microns.

In order for the electrostatic assumption to hold, the characteristic magnetic time must be much less than the characteristic electric time ($\tau_E \gg \tau_M$). Saville gives an approximation of 10^{-12} seconds as a minimum value of τ_E for the electrostatic assumption to be valid [49]. The IL under consideration in this study was 1-butyl-1-methylpyrrolidinium dicyanamide (BMPyrr DCA), which has a dielectric constant of 18.00 and an electrical conductivity of 1.123 S/m. Solving for the characteristic electric relaxation time yields

$$\frac{\varepsilon_r \varepsilon_0}{\sigma} = \frac{(18.00)(8.85\times10^{-12}\frac{F}{m})}{(1.123\frac{S}{m})} = 142.0 \times 10^{-12} s, \quad [2.3.5]$$

which is a longer electric relaxation time than the minimum guideline. This means that for the case of this study, the electrostatic modeling method was valid.

The first consequence of the electrostatic assumption is that the Maxwell-Faraday equation (Equation [2.2.4]) is reduced to

$$\nabla \times \boldsymbol{E} = 0. \quad [2.3.6]$$

Equation [2.3.6] essentially states that the electric field is conservative, i.e., has no rotation. In this case, the electric field vector, $\boldsymbol{E}$, becomes the gradient of the scalar electric potential, or voltage V_E, in volts (V), and is given by

$$\boldsymbol{E} = -\nabla V_E. \qquad [2.3.7]$$

Because of the relationship between $\boldsymbol{B}$ and $\boldsymbol{H}$ (Equation [2.2.21]), the Ampère-Maxwell equation (Equation [2.2.3]) can be rewritten as

$$\boldsymbol{J} = -\frac{\partial D}{\partial t}. \qquad [2.3.8]$$

Gauss's law (Equation [2.2.1]) is unchanged by the electrostatic assumption and likewise, the constitutive Equation [2.2.22] remains the same. However, Gauss's law for magnetism (Equation [2.2.2]) and constitutive Equation [2.2.21] are no longer required.

The conservation of charge equation (Equation [2.2.24]) can also be obtained by taking the divergence of the Ampère-Maxwell equation (Equation [2.2.3]), and by the definition of Gauss's law (Equation [2.2.1]),

$$\nabla \cdot \boldsymbol{J} = -\frac{\partial q}{\partial t}, \qquad [2.3.8]$$

is obtained. Based on a simplification presented by López-Herrera et al. [22], the free electric current density, $\boldsymbol{J}$, can be written as the sum of the ohmic charge conduction, $\sigma \boldsymbol{E}$, and the convection of charges, $q\boldsymbol{u}$, yielding

$$\boldsymbol{J} = \sigma \boldsymbol{E} + q\boldsymbol{u}. \qquad [2.3.9]$$

Which, substituting into Equation [2.3.8] yields

$$\nabla \cdot (\sigma \boldsymbol{E} + q\boldsymbol{u}) = -\frac{\partial q}{\partial t}. \qquad [2.3.10]$$

With the simplifications of the electromagnetic equations, the next step is to define the electromagnetic force terms in the conservation of momentum equation. The electromagnetic force acting on the fluid is governed by the Lorentz force, which is given as

$$\boldsymbol{b}_S^{EM} = q(\boldsymbol{E} + \boldsymbol{u} \times \boldsymbol{B}). \qquad [2.3.11]$$

Because of the electrostatic assumption, Equation [2.3.11] becomes

$$\boldsymbol{b}_S^{EM} = q\boldsymbol{E}. \qquad [2.3.12]$$

Also, since it has yet to be introduced, the body force due to gravity can be written as ρg. Before writing the final set of electrostatic equations, Equation [2.3.7] for $\boldsymbol{E}$, can be substituted into Equations [2.2.22], [2.3.10] (yielding the conservation of charge equation), and [2.3.12] resulting in

$$\boldsymbol{D} = -\varepsilon \nabla V_E, \qquad [2.3.13]$$

$$\nabla \cdot (-\sigma \nabla V_E + q\boldsymbol{u}) = -\frac{\partial q}{\partial t}, \qquad [2.3.14]$$

and,

$$\boldsymbol{b}_S^{EM} = -q\nabla V_E. \qquad [2.3.14]$$

Then, Equations [2.2.22] and [2.3.12] can be substituted back into Gauss's law (Equation [2.2.1]) and the conservation of momentum equation (Equation [2.3.2]) yielding

$$\nabla \cdot (\varepsilon \nabla V_E) = -q \qquad [2.3.15]$$

and

$$\rho \frac{\partial(\boldsymbol{u})}{\partial t} + \rho \nabla \cdot (\boldsymbol{u} \cdot \boldsymbol{u}) + \nabla P = \nabla \cdot \bar{\bar{\boldsymbol{\tau}}} + \rho g - q \nabla V_E \qquad [2.3.16]$$

These substitutions yield the final set of electrohydrodynamic equations as given in Table 2.3. For reference, the required interfacial conditions after the electrostatic simplifications are listed in Table 2.4.

Now the complete physical phenomena of the electrospray device under consideration are fully represented by the reduced governing equations obtained from the electrostatic assumptions. Next, the concept of quasi-static evolution and its relevance to this study is considered.

2.3.2 Quasi-Static Evolution

Besides the electrohydrodynamic model, further simplifications can be made to the computational model for determining onset voltage. Because onset voltage is the parameter of interest in this study, any electromagnetic phenomena that occurs after the start of IL emission is considered irrelevant. This means that space charge effects can be neglected since they only occur once the IL has begun emission and a volumetric buildup of charged particles can occur. This also serves to further simplify the electrostatic equations by eliminating the free charge density,

Table 2.3. Electrohydrodynamics governing equations.

Electrohydrodynamics Governing Equations		
Gauss's Law	$\nabla \cdot (\varepsilon \nabla V_E) = -q$	[2.3.15]
Conservation of Charge	$\nabla \cdot (-\sigma \nabla V_E + q\boldsymbol{u}) = -\frac{\partial q}{\partial t}$	[2.3.17]
Continuity	$\nabla \cdot \boldsymbol{u} = 0$	[2.3.18]
Conservation of Momentum	$\rho \frac{\partial (\boldsymbol{u})}{\partial t} + \rho \nabla \cdot (\boldsymbol{u} \cdot \boldsymbol{u}) + \nabla P = \nabla \cdot \bar{\bar{\boldsymbol{\tau}}} + \rho g - q \nabla V_E$	[2.3.16]

Table 2.4. Interfacial conditions for electrostatic assumption

Interfacial Conditions	
$\nabla V_{E,t2} = \nabla V_{E,t1}$	[2.3.19]
$\varepsilon \nabla V_{E,n2} = \varepsilon \nabla V_{E,n1} + q_s$	[2.3.20]
$(P_1 - P_2 + \gamma\kappa)\boldsymbol{n} = (\tau_1 - \tau_2)\boldsymbol{n} + \nabla \cdot \gamma + \rho g - q\nabla V_E$	[2.3.21]

q, from the governing equations. This simplification effectively decouples the electrostatics and fluid dynamics governing equations. This assumption and simplification lead to the method of quasi-static evolution that was first developed by Krpoun and Shea [31].

The quasi-static evolution can be considered as a series of static simulations that model the deformation of the IL into a specific Taylor cone shape [31]. The voltage at the Taylor-one tip is calculated for each successive simulation and is then recorded for each change of the Taylor cone shape. Once the voltage has reached a steady value, this is taken as the onset voltage. The modeling of the shape of the Taylor cone over time is important and will be discussed in greater detail in the following section. The ability to examine electrospray behavior as a series of static simulations reduces the need for any solution of dynamic equations, so long as the only parameter of interest is the onset voltage. For example, if the nature of the evolution of the IL deformation was of interest, the dynamic solution along with an examination of fluid behavior at the fluid-fluid interface would still be required. With this in mind, and by elimination of the free charge density from the governing equations, the hydrodynamic model reduces to

$$\nabla^2 V_E = 0, \qquad [2.3.22]$$

where ∇^2 is the Laplacian operator. In fact, this is a form of Laplace's equation for electrostatics and can be solved to determine the electric field strength in regions of interest for this study.

For each of the successive electrostatic simulations, the surface tension and electrical stresses are considered to be in equilibrium, which is represented by [31]

$$\frac{2\gamma}{r_a} = \frac{1}{2}\varepsilon_0 E_{EQ}^2, \qquad [2.3.23]$$

where r_a is the apex radius of the evolving Taylor cone shape in units of meters (m), and E_{EQ} is the equilibrium electric field magnitude. This linear relationship implies that, for every subsequent electrostatic analysis, the ratio of the electric field strength at some point to the voltage applied across the emitter is a constant. Since the goal of this study is to determine the onset voltage at the point of emission (i.e., the tip of the Taylor cone), the constant ratio of electric field strength at the liquid tip or apex is related to the applied voltage by

$$C = \frac{E_{Apex}}{V_{Applied}}, \qquad [2.3.24]$$

where C is a constant with units of inverse meters (1/m), E_{Apex} is the electric field strength at the liquid tip, and $V_{Applied}$ is the voltage applied across the electrospray emitter. Based on Equation [2.3.24], a relationship between the equilibrium electric field strength and the equilibrium voltage can be written as

$$V_{EQ} = \frac{E_{EQ}}{C}. \qquad [2.3.25]$$

In Equation [2.3.25] above, V_{EQ} is the equilibrium voltage. If Equation [2.3.25] is solved for E_{EQ} and substituted into Equation [2.3.23], then the equilibrium voltage can be solved for which results in

$$V_{EQ} = \frac{1}{C}\sqrt{\frac{4\gamma}{\varepsilon_0 r_a}}. \qquad [2.3.26]$$

For each new model simulation, the sharpness of the apex is increased, which changes the value of r_a for each simulation. As r_a is changed for each simulation (with constant applied voltage), the values of E_{EQ} and C also change. Krpoun and Shea found that as the apex radius changed with increasing sharpness of the liquid apex, the equilibrium voltage reached a steady-state value [31]. At this point, the equilibrium voltage does not vary with any changes in the apex radius due to increased sharpness of the liquid meniscus. This phenomenon can be seen in Figure 2.1. Then Equation [2.3.26] can be written as

$$V_0 = \frac{1}{C}\sqrt{\frac{4\gamma}{\varepsilon_0 r_a}}, \qquad [2.3.27]$$

which is the equation used to solve for V_0 in this study.

The next section of this report will detail the methods used to change the shape and increase the sharpness of the liquid meniscus or Taylor cone over the course of the electrostatic simulations.

2.3.3 Taylor Cone Modeling

The model assumes that the IL meniscus deformation follows the shape of a Taylor cone. As presented in Section 1.5.1 of the Literature Review, Taylor determined the half-angle of the conical shape for which the surface tension and electric tension were perfectly balanced to be $49.3°$. Taylor discovered this because he knew that there was a way to describe this phenomenon. After he observed trends in photographic images of his experiments, Taylor set out to determine the nature of the liquid deformation into conic sections. When examining the conditions at the point of a deformed drop, Taylor showed mathematically that the onset potential could be determined by the solution of the

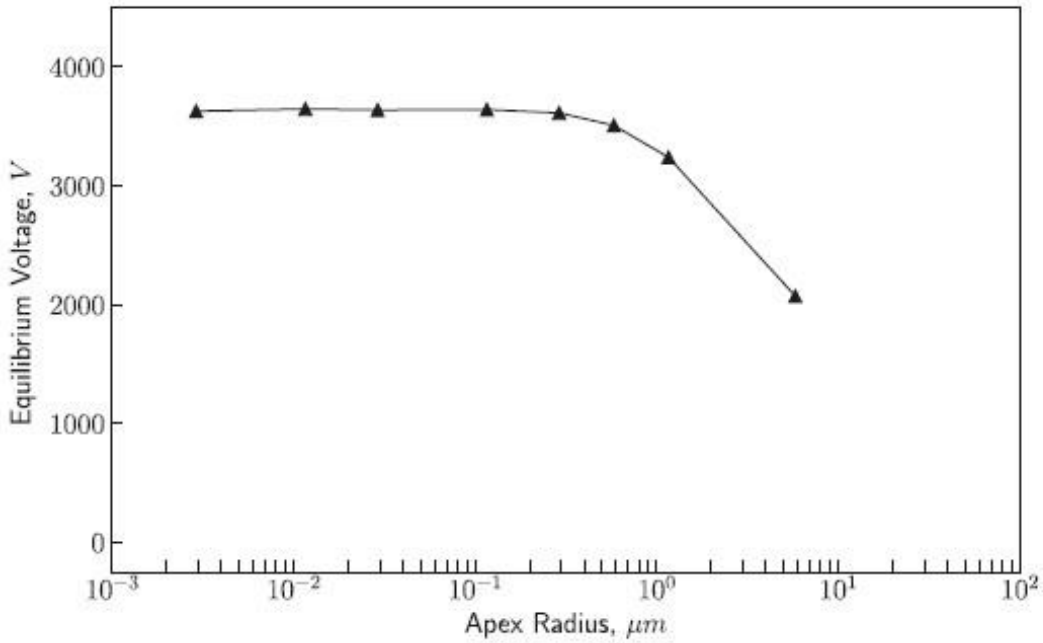

Figure 2.1. Plot of the equilibrium voltage as it approaches a steady-state value for decreasing r_a (taken from [34]).

½-order Legendre function given by [16]

$$P_{\frac{1}{2}}(\cos(\theta)) = 0. \qquad [2.3.28]$$

In Equation [2.3.28], θ is the angle between the horizontal and the surface of the cone's exterior. Based on tabulated solutions to Equation [2.3.28] Taylor determined that the only solution between 0 and π (or $180°$) was $130.7099°$ and therefore the cone half angle was found by

$$\phi_0 = 180° - 130.7099° \cong 49.3°. \qquad [2.3.29]$$

This is the well-known half-angle value for the Taylor cone, and it has been found that the half-angle approximation above is a reasonable estimate of the cone angle where electrospray emission occurs. This approximation for the cone half-angle is the one that was used by Jones et al. [34], and which is also used for this study.

Even though the half-angle above is a good approximation to the modeling of IL flows, it is worth noting that some studies have found some interesting discrepancies in the above value. Most notably is a study by Siddharth Maheshwari and Hsueh-Chia Chang [50], in which it was determined that the Taylor cone half-angle can vary drastically, depending on whether or not the driving field was generated by direct current (DC) or alternating current (AC). M. Gamero-Castaño, I. Aguirre-de-Carcer, L. de Juan, and J. Fernández de la Mora determined that the space-charge effects, fluid flow rate, and fluid properties also had an impact on the actual half-angle of the Taylor cone [51]. Their study in particular was interested in how this might affect liquid metal ion sources. Although some variations inevitably exist, the assumption of a cone half-angle of $49.3°$ is reasonably accurate and is used in this study. If future experimental data result in

a different half-cone angle, it would be quite simple to update the simulations to account for this difference.

The method of modeling that follows was adapted from Krpoun and Shea [31], who parametrically modeled the shape of the Taylor cone evolution based on a Bernstein-Bézier curve. The shape of the curve changes as the Taylor cone geometry is modified and increases in sharpness towards the theoretical point of electrospray emission. With the z-axis as the axis of rotation, this model is represented by

$$x(t,w,\phi) = \frac{(1-2t)r_a}{1-2t(1-t)(1-w)}\cos(\beta), \qquad [2.3.30]$$

$$y(t,w,\phi) = \frac{(1-2t)r_a}{1-2t(1-t)(1-w)}\sin(\beta), \qquad [2.3.31]$$

and

$$z(t,w) = \frac{2(1-t)twr_a}{1-2t(1-t)(1-w)}\cot(\theta), \qquad [2.3.32]$$

where in the above equations, $t \in [0,0.5]$ is the parametric variable, $\beta \in [0,2\pi)$ in radians (rad) defines the revolution of the conical section, $w \in [0,\infty)$ is a parameter related to the sharpness of the conical shape, and $\theta = \phi_0$ (assumed for this study) is the cone half-angle as defined in Equation [2.3.29]. A representation of the assumed shapes for several variations in the parameter, w, is shown in Figure 2.2. With an increase in w, it can be seen that the shape of the conical section varies from that of an ellipsoid up until $w = 1$, where the shape becomes a paraboloid, and after further increase of w, becomes that of a hyperboloid. Krpoun and Shea [31] also presented the representation of the apex radius as

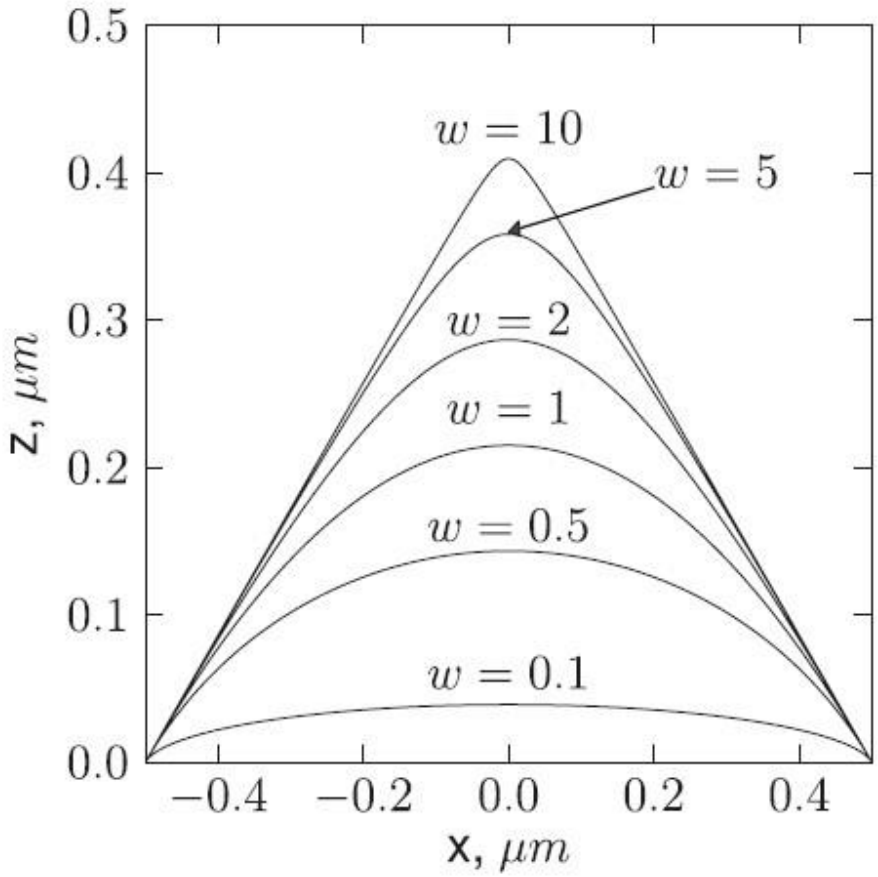

Figure 2.2. Representation of the Taylor cone modeling showing the effects of changes in w (taken from [34]).

$$r_a = \frac{r}{w}\tan(\phi_0), \qquad [2.3.33]$$

which was used in the numerical simulations performed in this work.

The computational model proposed by Krpoun and Shea above was used in this work as the basis for an analysis of electrospray emitters leading up to electrospray emission.

CHAPTER 3: METHODOLOGY

3.1 Design of Research Model for Electrostatic Simulations

The model used in this study has been designed according to the newest iteration of the electrospray thruster proposed by the μSTAMPS team. This design has been selected to provide for a more robust electrospray emitter. This design is achieved by the etching of capillaries and electrospray cavities in borosilicate glass, with an indium tin oxide (ITO) extraction electrode deposited on the top surface of the emitter (see Figure 1.7). Using Ansys EDT [28], three models were designed to simulate the three test cases used in this study: a single-capillary emitter, an array of capillary emitters, and a single-capillary case with the ability to simulate portions of the extraction electrode where the ITO has been erased. All of the models used for the electrostatic simulations are three-dimensional (3D) and utilize quarter-symmetry boundary conditions to reduce simulation computational costs.

The single-capillary case was used to aid in the reduction of the overall computational expenses for the required simulations. Single-capillary emitters were found by Jones et al. to be a good representation of how the onset voltage of a single emitter will behave when extended to the multi-capillary emitter array, i.e., an emitter chip [34]. Figures 3.1 and 3.2 show the single-capillary model from Ansys EDT. Figure 3.1 is an image of a 3D view of the emitter design with several key features labeled. Figure 3.2 shows a two-dimensional (2D) representation of the emitter while also displaying key features of the design.

The next variation in geometry that was studied included the ability to replace a section of the ITO extraction grid with borosilicate glass to simulate ITO erasure from the extraction grid. The onset voltage is examined as the width of

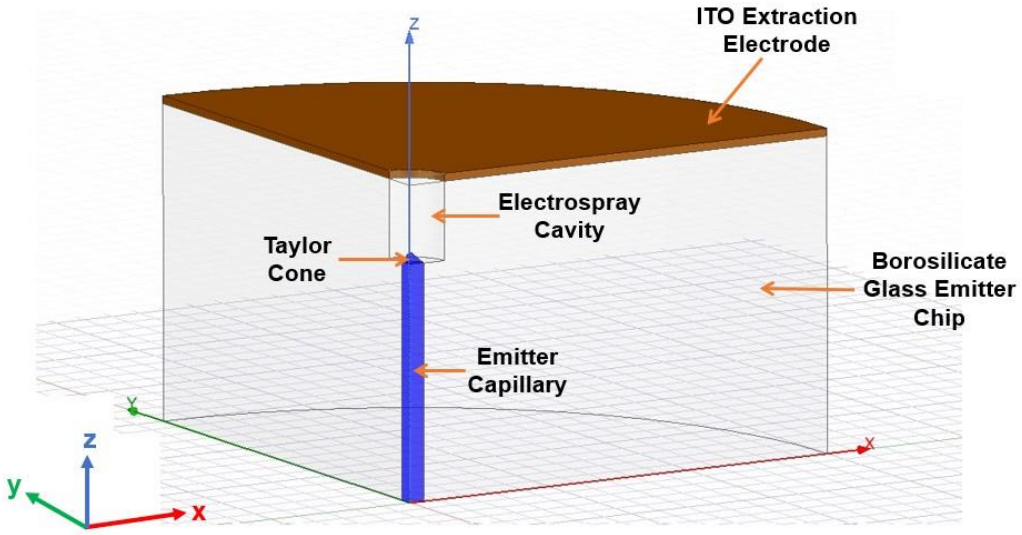

Figure 3.1. 3D view of the single-capillary model from Ansys EDT.

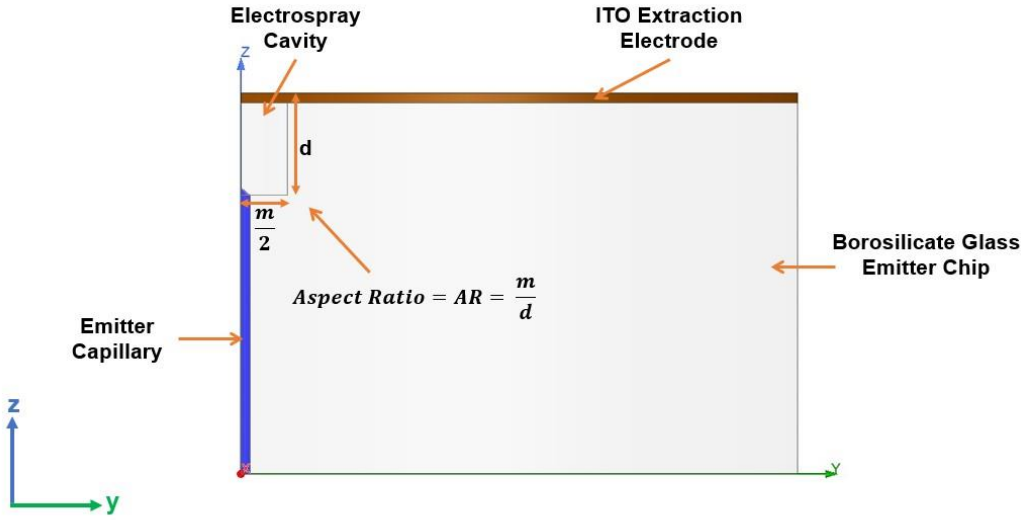

Figure 3.2. 2D view of the model from Figure 3.1 including the dimensions of the electrospray cavity.

the ITO erasure, W_e, is increased to determine the impact of ITO erasure. This will be discussed further in Section 3.3.2. Figures 3.3 and 3.4 show the model that was used for simulating ITO erasure.

Since practical electrospray thrusters rely on arrays of capillary emitters (i.e., an emitter chip) to provide thrust, a 3D model of a multi-capillary emitter array was designed in Ansys EDT. Simulation results from the emitter array were compared to the single-capillary case to determine the accuracy of the single-emitter case for the current design iteration. Figures 3.5 and 3.6 display the 3D and 2D representations of the emitter-array model, respectively.

3.2 Determining Onset Voltage

Since this work follows the methods of Jones et al. [34], the same methodology for determining the onset voltage will be used. This method follows from Section 2.3 and is briefly repeated here for convenience. The shape of the Taylor cone is assumed by the parametric Equations [2.3.30] – [2.3.32]. The simulation is then performed for the given (assumed) Taylor cone shape. After the first simulation has been completed, a second is performed, where the sharpness of the Taylor cone is increased by changing the sharpness parameter, w, to a larger value. This process is repeated until the electric field strength at the tip of the Taylor cone, and consequently the onset voltage, reaches a steady-state value. This indicates that the onset voltage has been achieved for the assumed Taylor cone shape and that no changes in onset voltage will occur even when w is further increased. It was determined by Jones et al. that the simulations had generally reached steady state for $w \sim 11$. Therefore, this value of w is used in this study for calculation of the onset voltage. The mesh resolution of the model is important to attaining accurate results, especially in the sharp apex of the Taylor cone. Special attention to the mesh resolution of the model was given by Jones

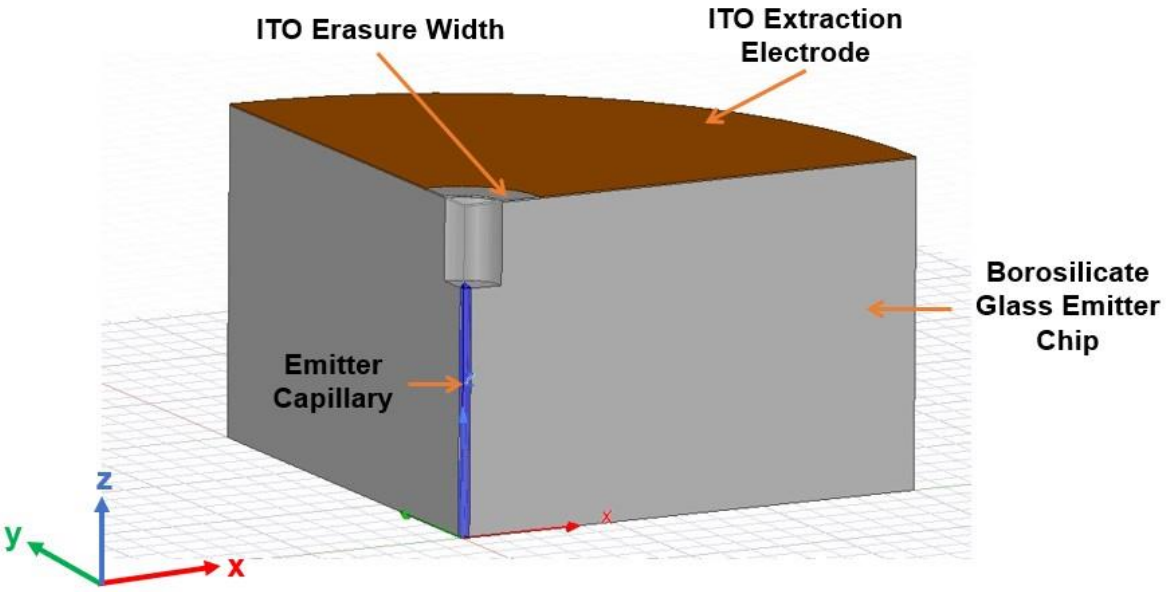

Figure 3.3. 3D view of the Ansys EDT model used for the extraction grid erasure simulations.

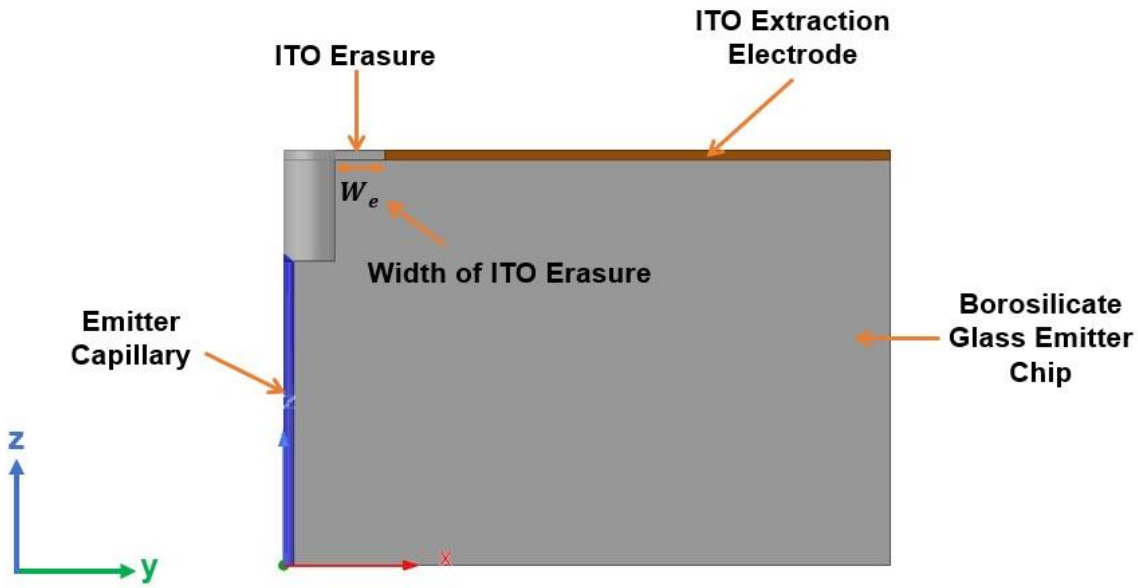

Figure 3.4. 2D view of the model from Figure 3.3 including the dimensions of the electrospray cavity.

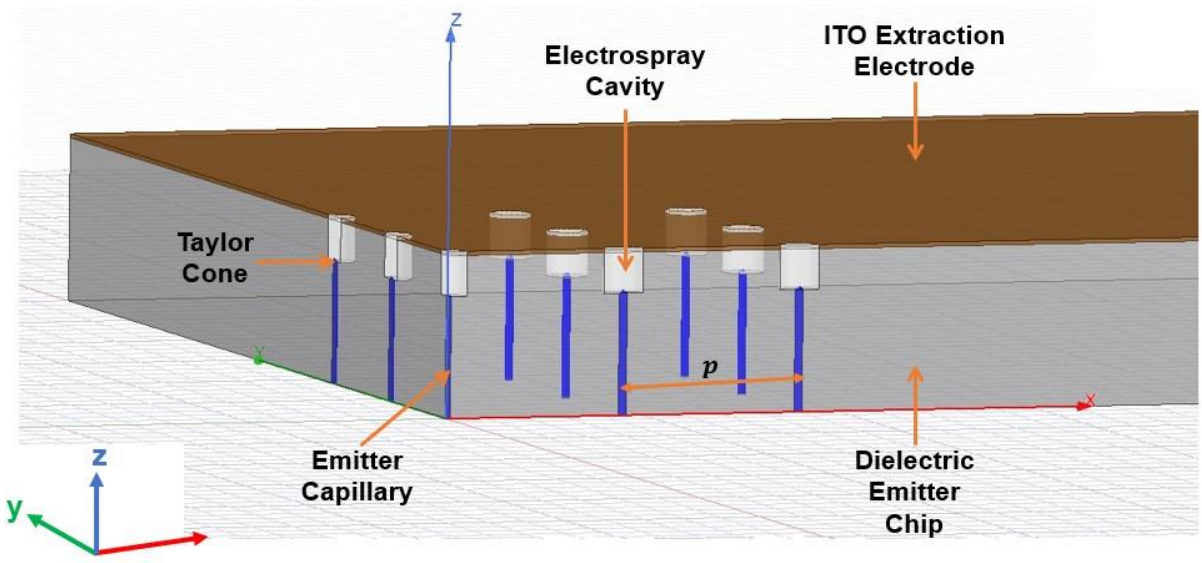

Figure 3.5. 3D view of the multi-emitter array.

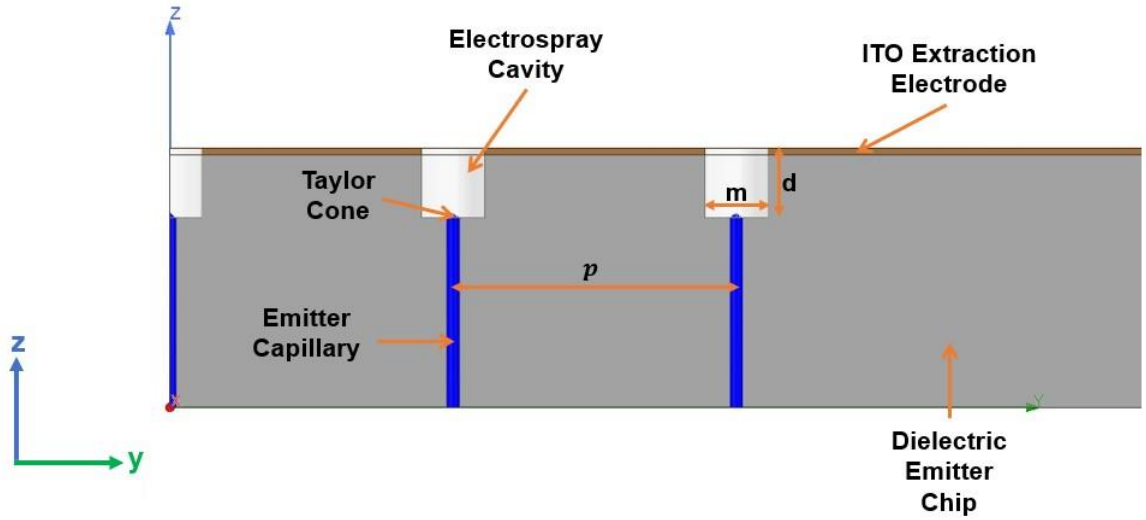

Figure 3.6. 2D view of the model from Figure 3.5 including the dimensions of the electrospray cavity.

et al. [34] to achieve accurate simulation results. The process that was used by Jones et al. [34], and in this study, is presented in the following section. A mesh convergence study for the current model was also performed and is discussed in Section 3.2.2.

3.2.1 Mesh Resolution Guidelines for Mesh Independent Solutions

It was determined by Jones et al. that the shape of the Taylor cone can be approximated and used in subsequent simulations. This is related to the manner in which the mesh resolution is assigned for the electrostatic simulations in Ansys EDT. Jones et al. found that the increased sharpness of the Taylor cone tip had a direct impact on the simulation results. Therefore, the region of the IL capillary column, the Taylor cone base, and the Taylor cone tip, or liquid apex, had to be assigned separate values for their element lengths, L_e, in nanometers (nm). The section of the IL capillary column was assigned an L_e of 400 nm, which was found to be sufficient for this region. The Taylor cone was given a total height, h (μm), which was then split into the two sections mentioned above (Taylor cone base and liquid apex). The Taylor cone base was assigned a height of $0.9h$, while the liquid apex was assigned the remaining height of $0.1h$, which correspond to 90% and 10% of the total Taylor cone height, respectively. Jones et al. defined the maximum L_e as M (nm). The liquid apex was assigned a value of M, while the Taylor cone base was assigned a value of $10M$. A convergence study was then performed for decreasing values of M, and mesh-independent solutions were found to begin for values of M that were 1 nm or less. This corresponded to M values of 1 nm and 10 nm for the liquid apex and the Taylor cone base, respectively. These results are represented in Figure 3.7. These results were obtained by using a set value for the IL capillary radius, r_c, and w. However, the result for the set values used in the convergence study can be used to scale M to any variations in r_c and w, which reduces the need for tedious mesh-requirement

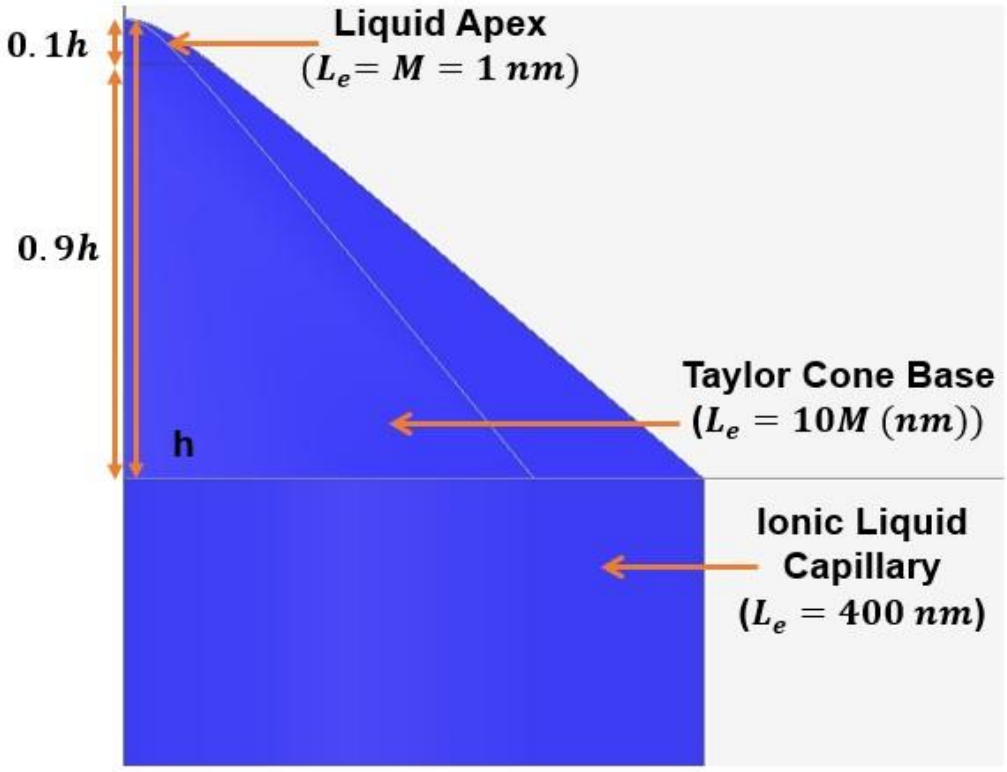

Figure 3.7. Regions of the IL column where specific element lengths, L_e, were required.

analysis in future simulations.

3.2.2 Mesh Convergence Study

The results from Jones et al. [34] that were discussed above were used as a starting point in this study. However, to ensure accuracy in the simulation results, a separate convergence study was performed with the current geometric design for the electrospray emitter. The convergence study was performed for the values of $w \approx 11.63$ and $w \approx 13.95$ for three values of AR. These values of AR were chosen to account for a representative selection of AR values across the simulation space. The values of L_E used in this study (in nm) are 0.5, 0.75, 1, 2, 4, 6, 8, and 10. The aspect ratios and their corresponding values of m and d that were used in the convergence study are shown in Table 3.1.

3.3 Simulation Variations

Since the goal of this research project is to find an emitter design that optimizes onset voltage, several characteristic features of the currently proposed μSTAMPS electrospray emitter are considered. These features include variations in the electrospray-cavity aspect ratio, etching effects of the ITO extraction grid, and a comparison of potential IL propellants. The specifics of these variations are discussed in the following sections.

3.3.1 Electrospray Cavity Aspect Ratio

The aspect ratio of the electrospray cavity of the proposed emitter is an important design feature for the current μSTAMPS emitter design. As defined in

Table 3.1. AR variations, and their corresponding values of m and d used in the mesh-convergence study.

AR [--]	m [μm]	d [μm]
2.5	5	2
1	25	25
1	50	50

Section 1.4, the AR of the electrospray cavity is defined as the ratio of the cavity width to height, $\frac{m}{d}$. In the simulations that were performed, values of m were chosen for $m = 5 - 50$ μm in increments of 5 μm, and d was then varied in 2 μm increments from $d = 2 - 50$ μm. Then d was varied in the same manner for the next value of m. The next simulation variation was for changes in m with d held constant. The value of m was varied from $m = 5 - 50$ μm for constant d values in the range of 5 – 50 μm with a step size of 5 μm. These variations were chosen so that the results covered a large range of simulation results that could be useful in determining the optimal values of emitter onset voltage.

3.3.2 ITO Extraction Grid Erasure

As introduced in Section 1.4, the effects of the erasure of a portion of the ITO extraction grid are considered in this study. Variations in the amount of erasure, W_e, were modeled and compared to determine the impact of erasure on the onset voltage of the emitter. Several cases were studied that correspond to a selection of the aspect ratios that resulted in optimal onset voltage from the results of Section 3.3.1. Therefore, m and d were held constant while W_e was changed. The variations in W_e used were from 2 – 16 μm in increments of 2 μm.

3.3.3 Ionic Liquid Comparison

Since ILs have differing physical properties, it is useful to compare the effect of the most widely used IL propellants on the onset voltage of the electrospray emitter. The ILs that were considered for this study are BMPyrr DCA, EMI-BF4, and EMI-Im. When considering electromagnetic effects, the most important properties of ILs for use in electrospray applications are the relative permittivity, ε_r, electrical conductivity, σ, and surface tension coefficient, γ. Table 3.2 shows the properties mentioned above as given by empirical results from the literature.

Table 3.2. Relevant physical properties of the ILs used in this study at $\mathbf{25}$*° C.*

Ionic Liquid Propellants (25° C)			
	ε_r [--]	σ [S/m]	γ [N/m]
BMPyrr DCA	18.00 [52]	1.317 [54]	0.0561 [56]
EMI-BF4	12.90 [53]	1.573 [55]	0.0444 [57]
EMI-Im	12.00 [52]	0.921 [55]	0.0359 [58]

The onset voltage is calculated for the three IL choices for variations in AR. The AR variations were chosen for m values of 5 μm, 25 μm, and 50 μm, while d was varied from 2 – 50 μm in 2 μm increments. These choices for m have been used to obtain results across the range of AR variations used in this study.

3.3.4 Comparison of Single-Capillary Emitter and Multi-Capillary Arrays

The single-capillary emitter case is a simplification of the multi-capillary-emitter chip; therefore, it is useful to compare the results from the single-capillary case to the emitter-chip results since electrospray thrusters operate with multi-capillary-emitter chips for practical applications. Simulations were performed for the same ranges of data for AR variations with d and m as the single capillary case, except that a step size of 4 μm was used. Based on the results of Jones et al. [34], the emitter pitch-to-height ratio should be $\frac{p}{h_e} \geq 2.5$ to escape the shielding effects of neighboring emitters. The ratio used in this study is equivalent to 2.5.

CHAPTER 4: RESULTS AND DISCUSSION

In this chapter, the results and their significance are discussed. The mesh convergence study is presented first, since it has a direct impact on the accuracy of the rest of the design features considered in this study. The simulation results are then considered, beginning with the change in V_0 with variations in AR, followed by the impact on V_0 from ITO erasure from the extraction grid, a comparison of V_0 between IL propellants, and finally the effects of AR on V_0 for emitter arrays is discussed.

4.1 Mesh Convergence Study Results

Determining the values of L_E for which the electrostatic solutions become mesh independent is very important in producing accurate simulation results for the rest of this study. This was achieved by examining decreasing values of L_E for the values of AR and w discussed in Section 3.2.2. The convergence study showed that the modeling assumptions used by Jones et al. [34] are also valid for use in this study. Figures 4.1 and 4.2 show the results of the convergence study for $w \approx 11.63$ and $w \approx 13.95$, respectively. Note that the abscissas in both plots are logarithmic in scale. The results from both studies clearly show that for all cases, there is minimal variations in the simulation results (electric field intensity), and the mesh yields steady results for values of $L_E \leq 1$ nm. In fact, once the onset voltage had been determined, there was a less than 1% difference in onset voltage with an increase in w. This indicates that the simulation results achieved in this study are mesh independent and that there is no need to increase the sharpness parameter past the suggested value of $w \approx 11.63$ established by Jones et al. [34].

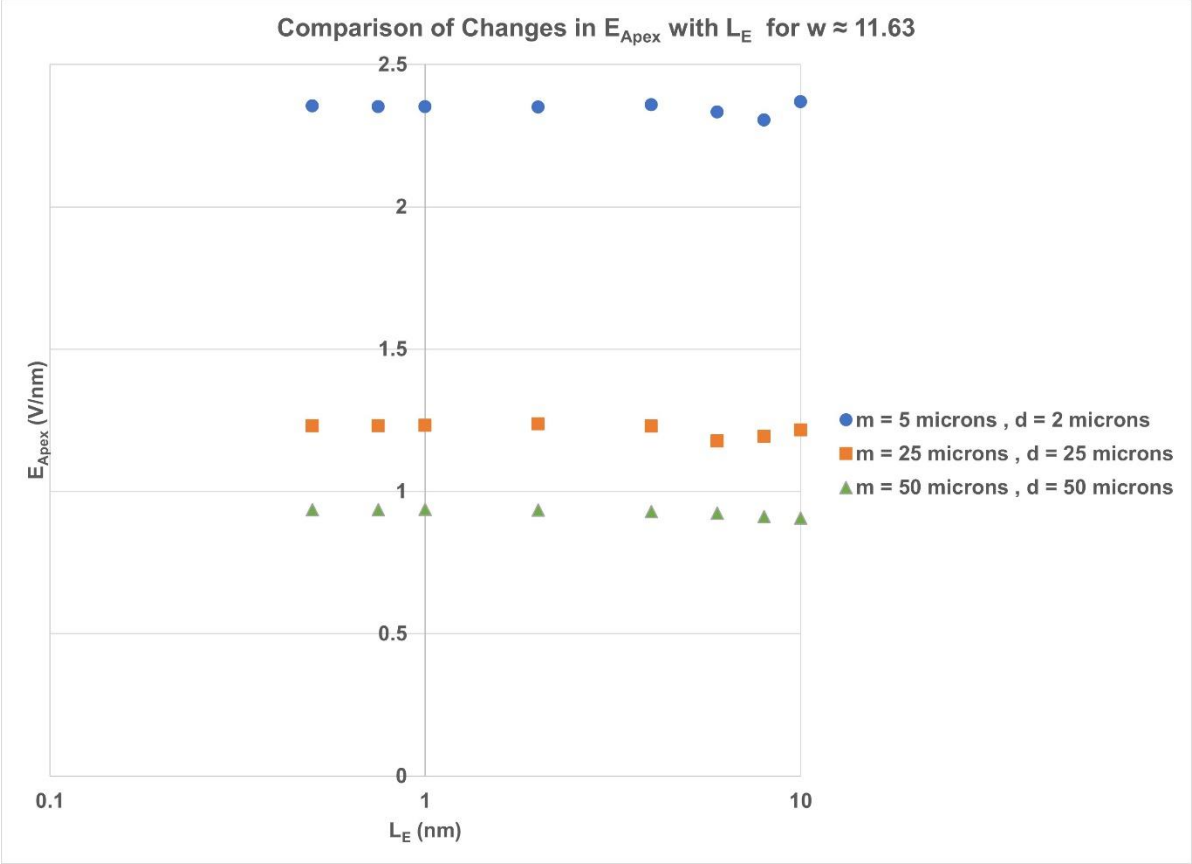

Figure 4.1. Mesh convergence study results for $w \approx 11.63$.

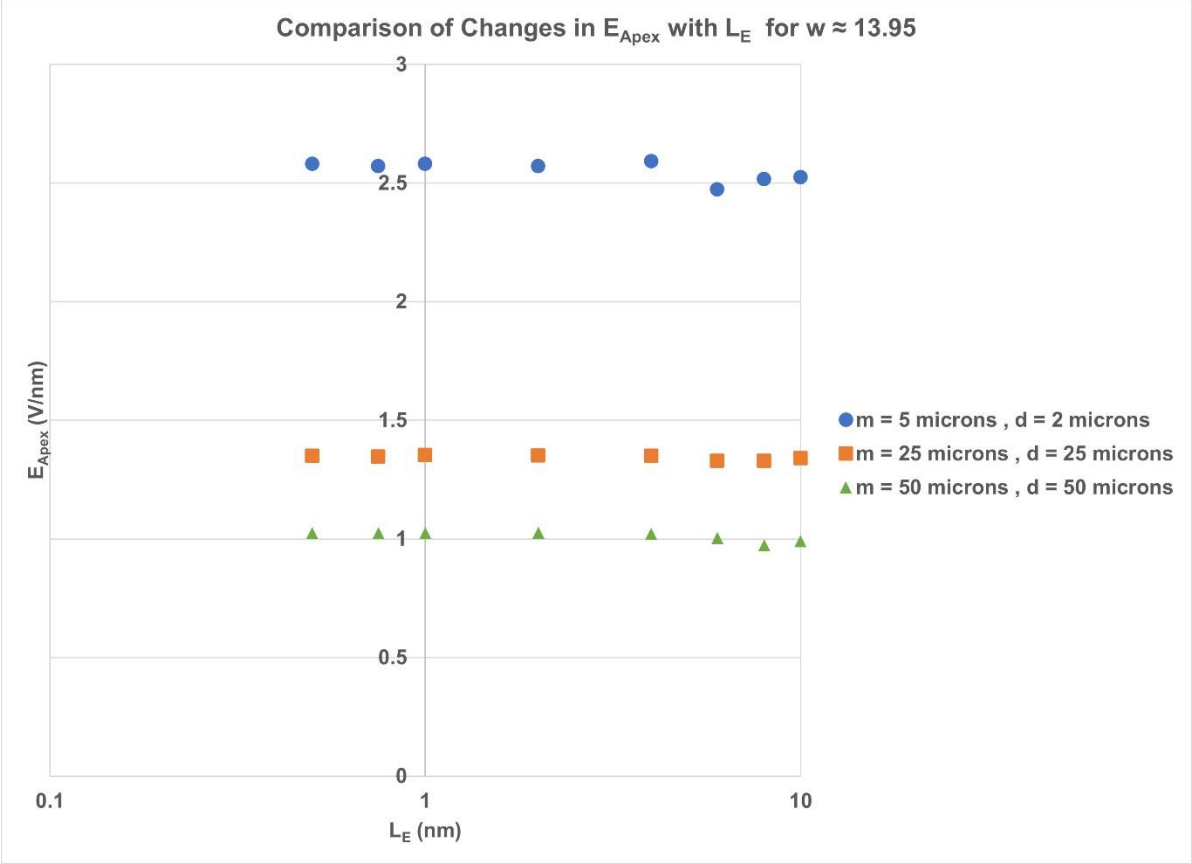

Figure 4.2. Mesh convergence study results for $w \approx 13.95$.

4.2 Electrospray Cavity Aspect Ratio

Now that the accuracy of the simulation model has been demonstrated via the mesh convergence study, variations in the simulation can now be considered. The first design feature that is considered is the variations of the emitter AR that were discussed in Section 3.3.1 and its impact on V_0. The effects of changes in AR on V_0 for variations in d with m held constant can be seen in Figure 4.3.

Although the highest computed aspect ratio was 25, which corresponded to $m = 50$ μm and $d = 2$ μm, the optimal aspect ratio (AR_{opt}) for the entire data set was always found to be $AR < 6$. Furthermore, AR_{opt} only changed by 2.5 across the data considered in this study, i.e., $2.5 \leq AR_{opt} \leq 5$. As m is increased, the corresponding value of d also changes. In some cases, for example $m = 10$ μm and $m = 15$ μm, the value of d for AR_{opt} remained the same even though m had increased.

Figure 4.4 displays the relationships between variations in m and d that results in AR_{opt}. Although d does not change with each increase in m, d does increases with m monotonically. Further conclusions might be drawn if the simulation step size between m was decreased from the value of 5 μm used in this study; however, the relationship between m and d to obtain AR_{opt} is not one-to-one.

If the values of V_0 are compared for $m = 5$ μm and $m = 50$ μm (i.e., the upper and lower limits compared in this study), the effects of wider electrospray cavities can be seen. From the simulation results, V_0 for $m = 5$ μm and $m = 50$ μm are 151 V and 310 V, respectively.

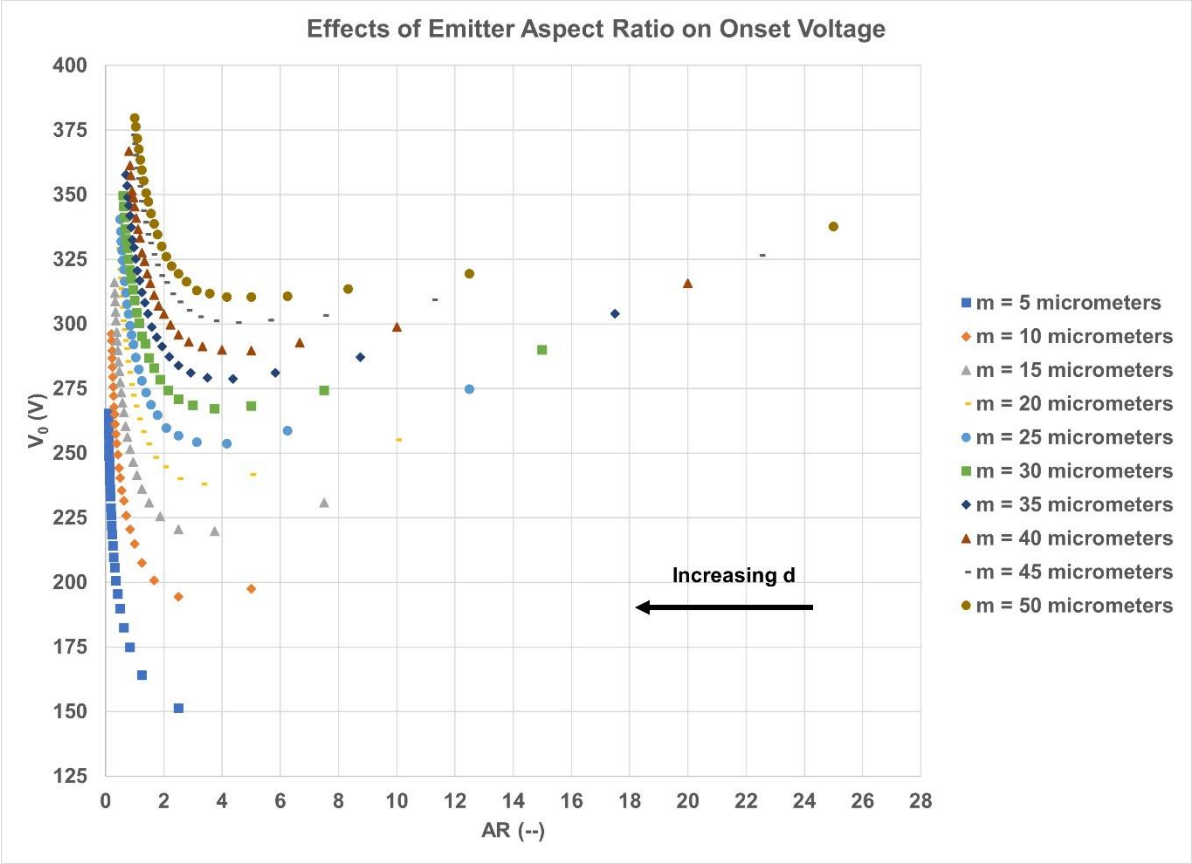

Figure 4.3. Comparison of the effects of emitter AR on V_0 for variations in d with m held constant.

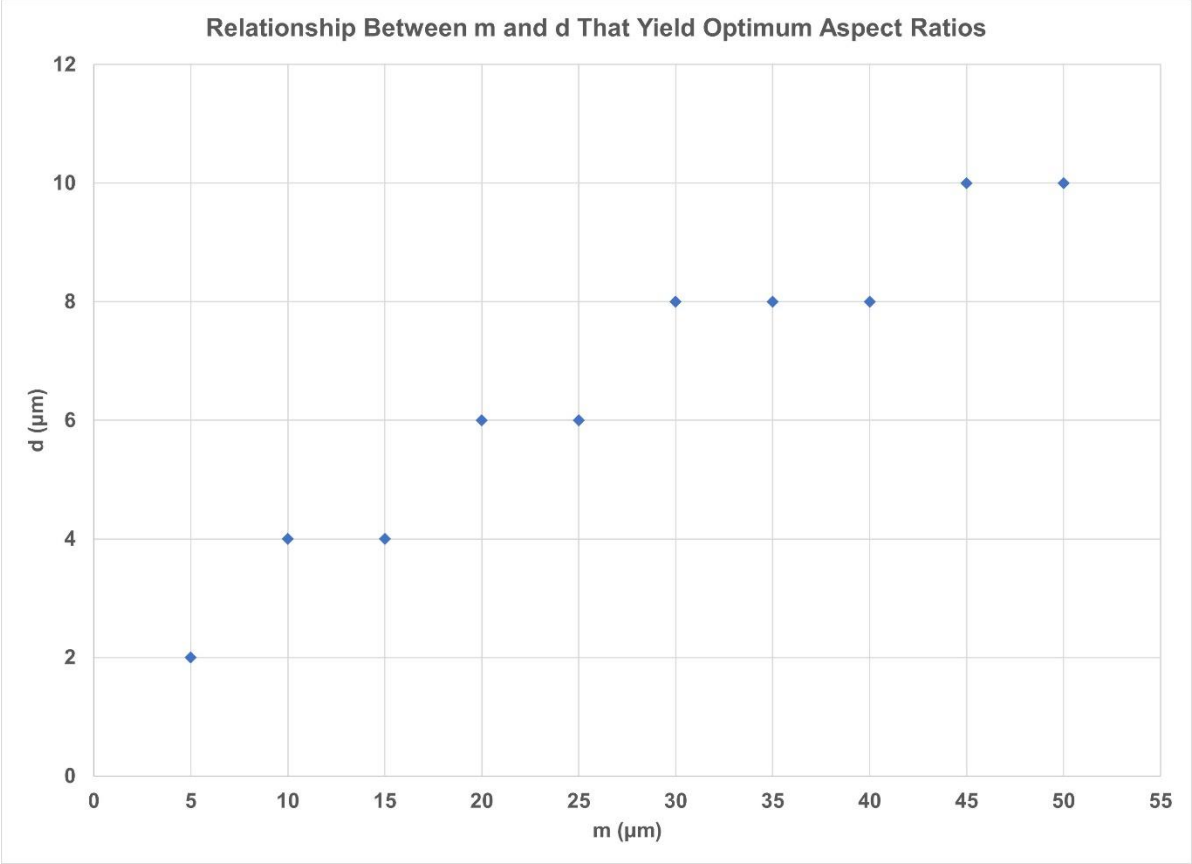

Figure 4.4. Values of d for increasing m values that result in AR_{opt}.

This corresponds to an 105% increase in onset voltage across the parameter space that was studied. Therefore, to reduce V_0 requirements, electrospray cavities with small values of m and d are desirable for design choices where m is considered a set or chosen value for the design. This helps to explain the designs of some of the electrospray thrusters seen in the literature, i.e., with emitters placed closely to the extraction grid.

Before discussing the results of AR simulations where m is varied as d is held constant, a note is made regarding the possible reasons for the results discussed above. Jones et al. determined that emitters with a short extraction grid distance resulted in lower onset voltage values [34]. In this study, it was found that smaller values of d for a given m value resulted in lower onset voltages. This is equivalent to a shorter extraction grid distance in this study, because as d increases, the distance from the IL to the extraction grid also increases. This would support the results of Jones et al. in stating that achieving a small extraction grid distance aids in obtaining a smaller value of V_0 [34]. Similarly, Jones et al. also stated that to escape shielding effects of the electric field strength near the extraction grid (or where the applied voltage is applied), that there should be some spacing between the emitter and extraction grid [34]. In this study, the applied voltage was applied to the extraction grid while the IL remained at ground. Since Jones et al. determined that the electric field shielding effects are pronounced when two fields are in close proximity [34], this may explain why the onset voltage begins at a higher value (for close proximity to the extraction grid) and then decreases to a minimum value before increasing again as the IL and extraction grid move apart. It is possible that for high AR values that shielding effects are prevalent. These shielding effects then become less dominant as AR decreases until V_0 reaches a minimum value. Then as AR becomes even smaller, the distance between the extraction grid and IL grows. A decrease in the electric field strength at the IL apex occurs due to this distance and the required value of V_0

increases. This can be seen in Figure 4.5 where V_0 can be seen to decrease with d before beginning to increase again after the minimum value of V_0 is achieved. Another possible explanation for this effect could be the nature of the electric field itself and how it is formed for these geometric variations. Even though more research is required to determine the nature of this result, it is important to design emitters with the guidelines mentioned above to obtain smaller values of V_0.

The next variation of AR was for changes in m with d held constant. Figure 4.6 represents the relationship between these variations and V_0. In this case, the highest computed AR was 10. The minimum V_0 always occurred for $AR < 2$. The range of AR_{opt} values for this parameter space was $0.1 \leq AR_{opt} \leq 1$. This range is smaller than the results considered when m was held constant as d was varied. The minimum values of V_0 for the bounds of this parameter space ($d = 5$ μm and $d = 50$ μm) are 170 V and 265 V, respectively. This results in a 56% increase in V_0 across the parameter space, which is less than the 105% result when variations in d were considered for constant m.

Another interesting result can be seen in Figure 4.7, which demonstrates trends in V_0 for increasing m with d held constant. Unlike the results for variations in d with m held constant, as seen in Figure 4.5, there is no decrease to an AR_{opt} value before a corresponding increase. It can also be seen that for $d \leq 20$ μm, there is some overlap between V_0 values as m is increased. This is likely a consequence of electric field interactions near the liquid-apex region or possibly a result of how the electric field is formed in this region for certain geometrical variations in the electrospray cavity. However, this overlap occurs for values of AR beyond those which yield AR_{opt}, therefore this result is not likely to have an impact on emitter chip design considerations. The value of AR_{opt} in each case corresponded to the lowest value of m, 5 μm. Figure 4.8, which shows the

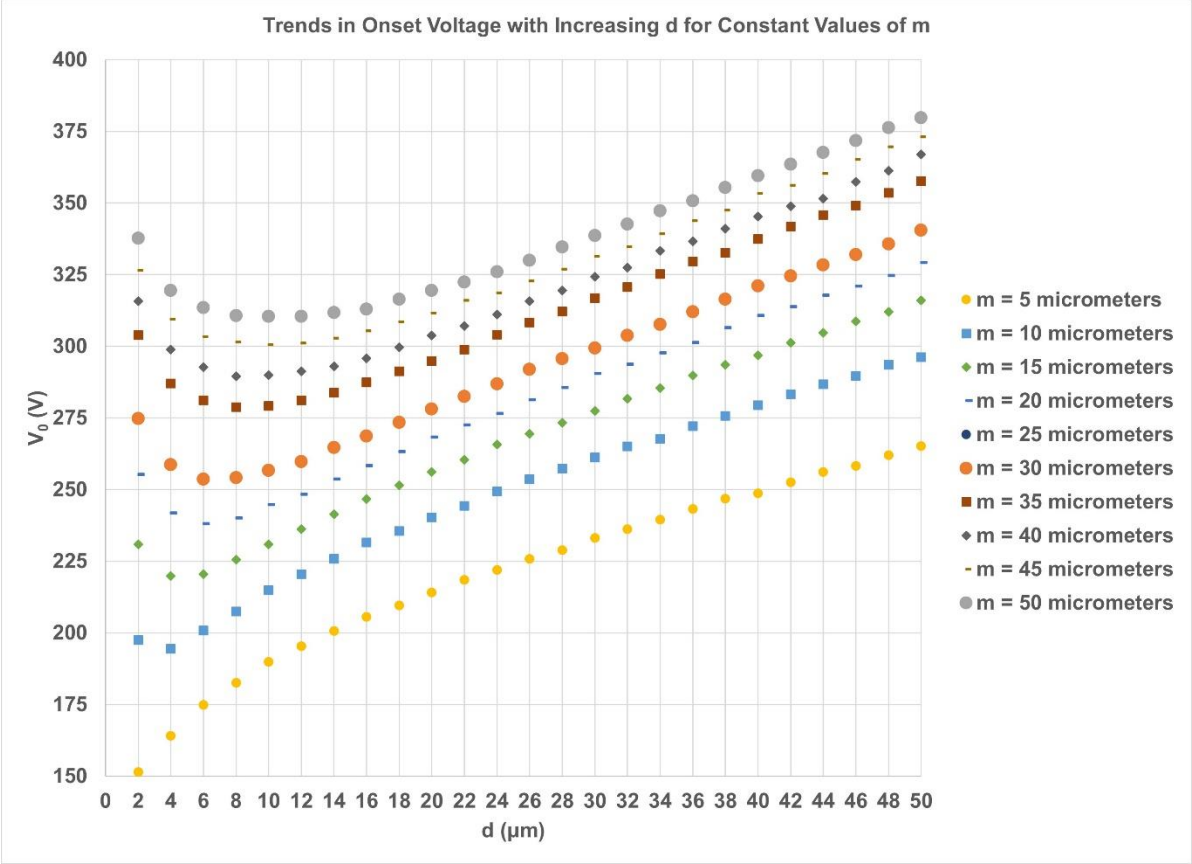

Figure 4.5. Comparison of the behavior of V_0 with increasing d for set values of m.

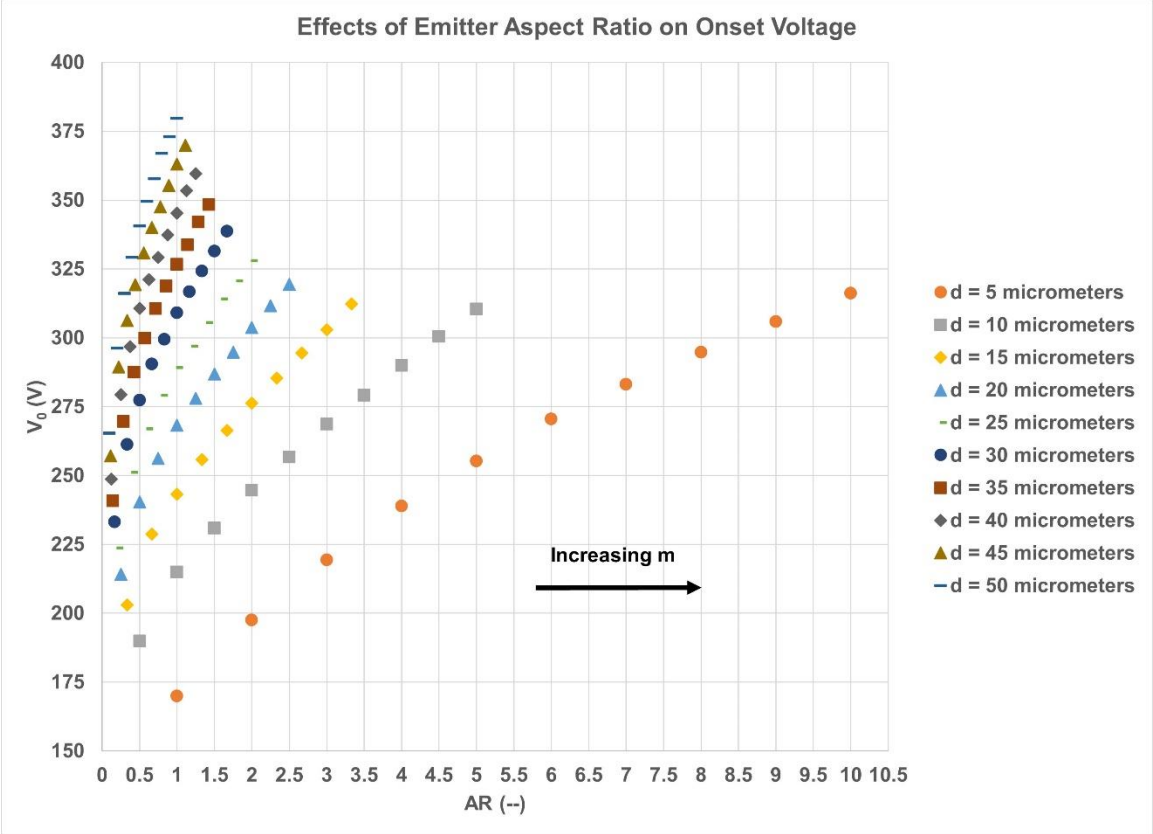

Figure 4.6. Comparison of the effects of emitter AR on V_0 for variations in m with d held constant.

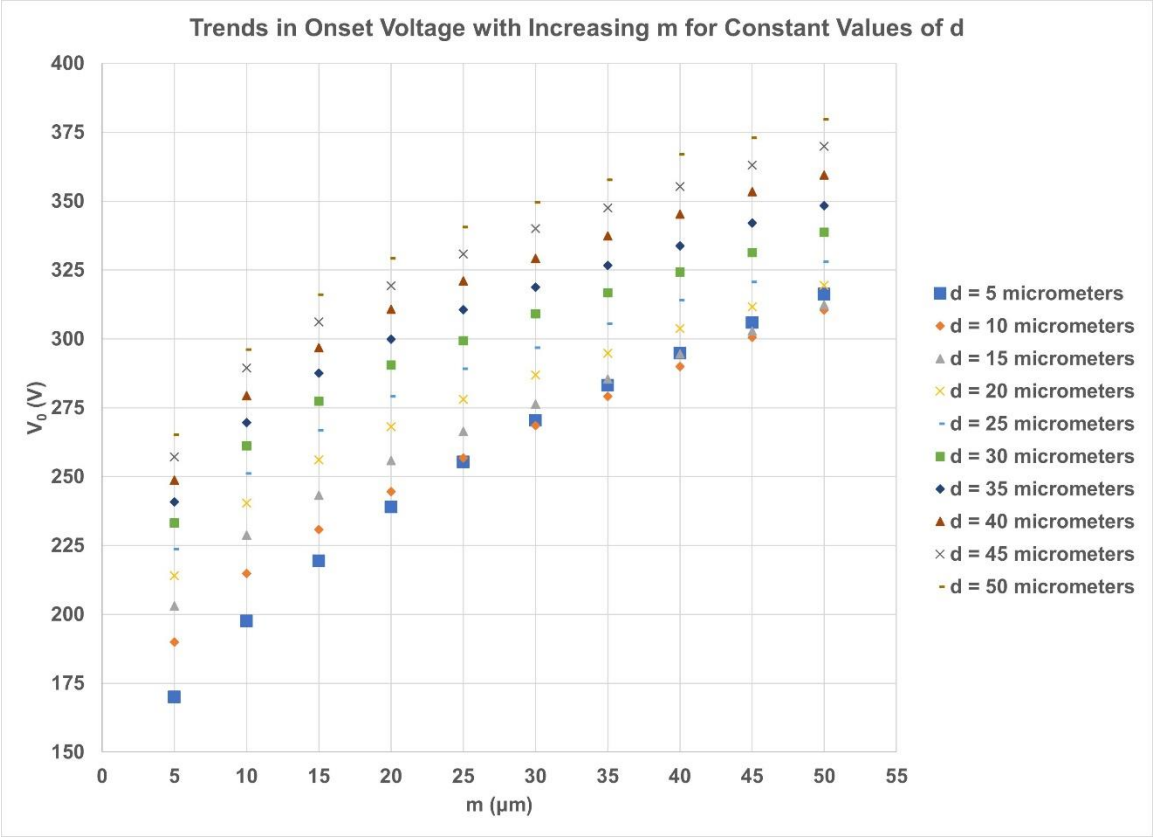

Figure 4.7. Comparison of the behavior of V_0 with increasing m for set values of d.

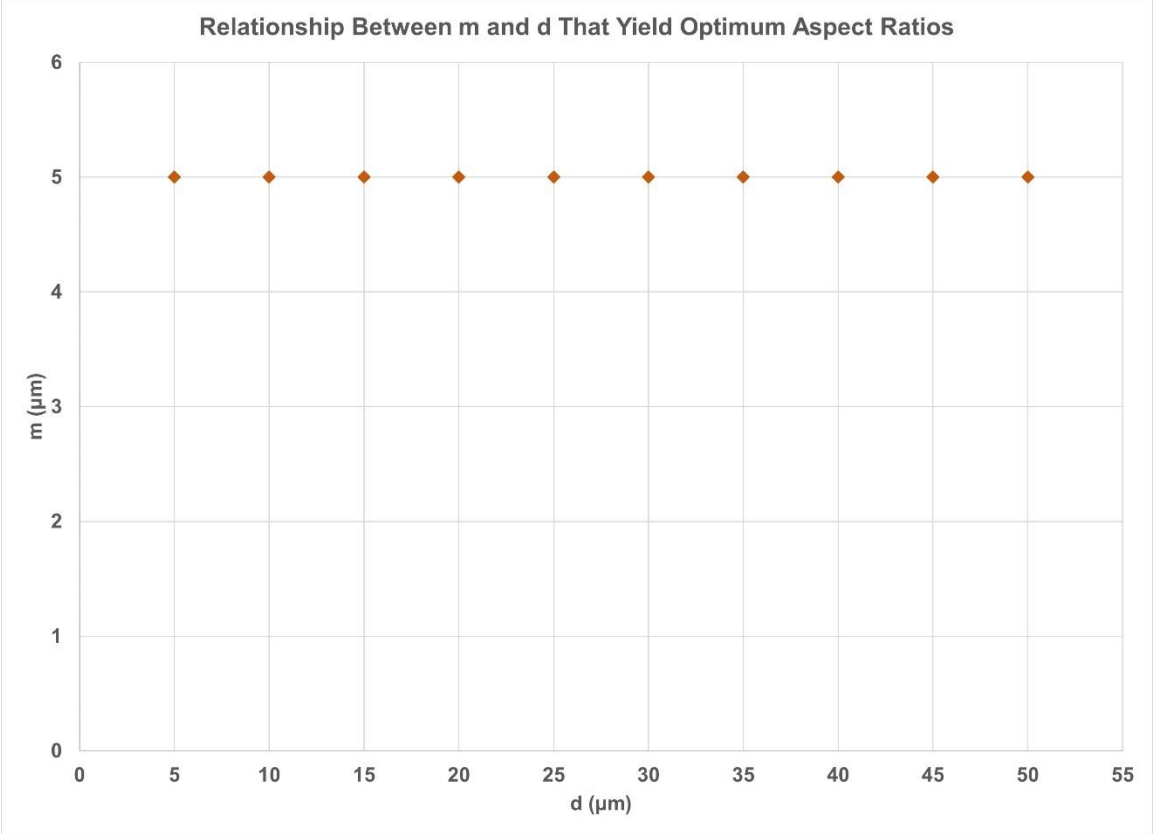

Figure 4.8. Values of m for increasing d values that result in AR_{opt}.

relationship between m and d that yield AR_{opt}, highlights this effect. As can be seen in Figure 4.8, the value of m that yielded AR_{opt} was always 5 μm, even as d was increased. This suggests that m should be made as small as possible for any design choice where d is a set or chosen parameter.

4.3 ITO Extraction Grid Erasure

The next design parameter to consider, is the effect of ITO extraction grid erasure on V_0. From an intuitive standpoint, the expected result would be that as the amount of ITO erasure increases, V_0 should increase as well. This is because as ITO is erased, the distance from the IL to the conducting portion of the extraction grid is increased. Physically speaking, the electric field experienced by the IL will be diminished as the distance to the extraction grid grows with ITO erasure. The simulation results also show an increase in V_0 as W_e is increased, i.e., the electric field strength has decreased. Figure 4.9 displays the results of the simulations that considered the impact on V_0 from increasing W_e.

As expected by intuition of the physical situation, V_0 increases with W_e. Another interesting result is the percent increase in V_0 between the maximum and minimum values of W_e as m increases, i.e., the difference in V_0 between $W_e = 2$ μm and $W_e = 16$ μm. This result can be seen in Figure 4.10, where the percent increase in V_0 over the range of W_e for each increase in m is shown. This result shows that for wider electrospray cavities, the percentage increase in V_0 is less for smaller values of m. Also, it is worth noting that d only changes by 10 μm compared to the 50 μm that m changes. This indicates that d is more sensitive to the results of ITO erasure. However, since this effect is most profound for small values of both m and d, erasure should be minimized in all cases. Before discussing this result, it is important to note that the results here are entirely dependent on the emitter geometry.

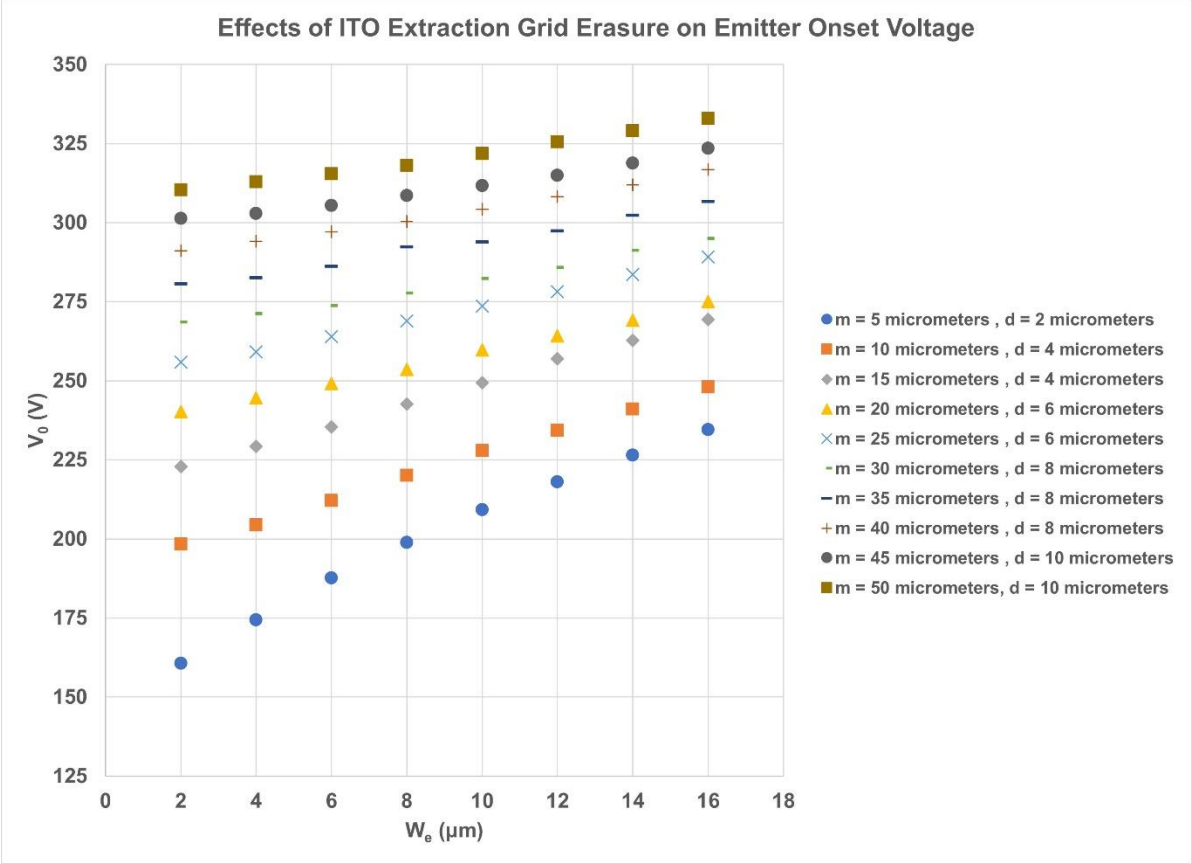

Figure 4.9. Effects of ITO W_e on V_0 for the AR_{opt} values found in Section 4.2.

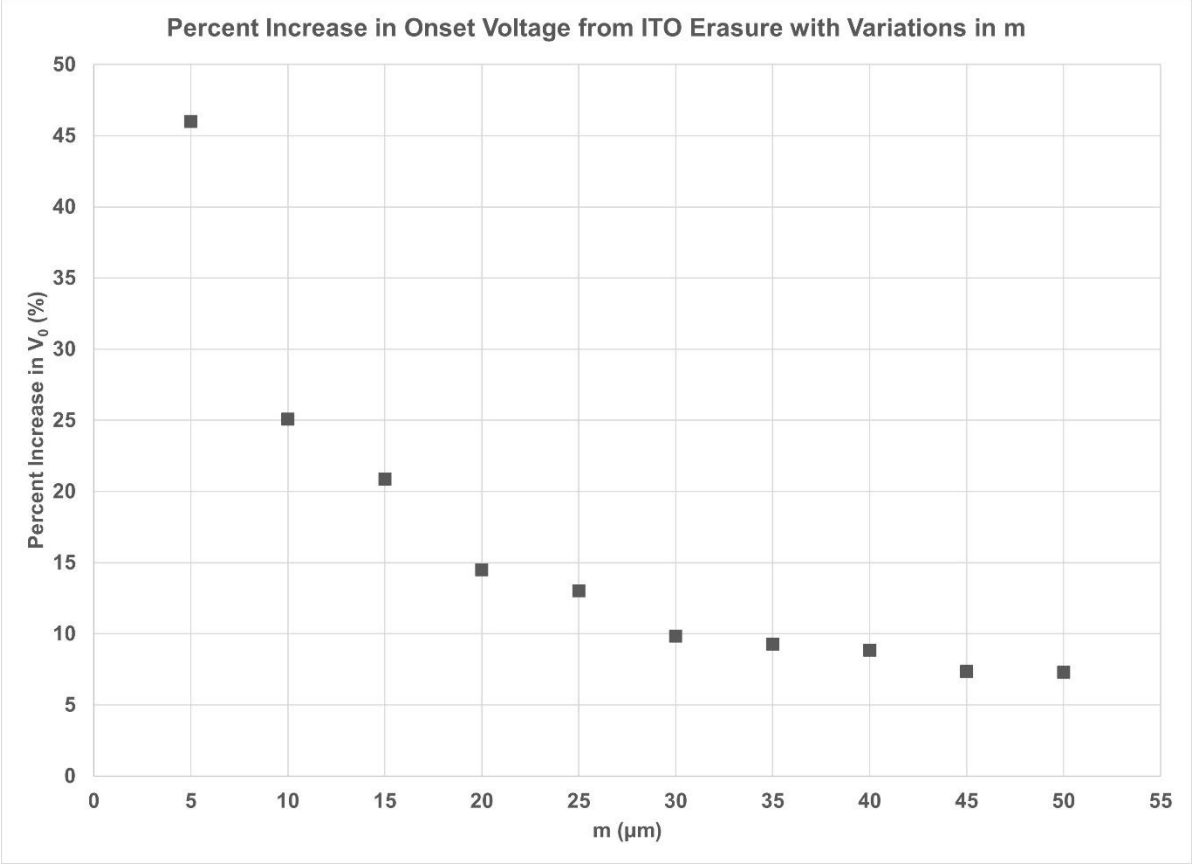

Figure 4.10. Percent increase in onset voltage with increasing m and W_e.

This is because V_0, as determined by Equation [2.3.27], depends only on the liquid-apex radius, r_a, which in turn only depends on the sharpness parameter w, the Taylor-cone half angle, and the IL capillary radius, r, which are all constant between simulations. This means that any change in V_0 is due to a change in the electric field strength, which is dependent only on changes in the emitter geometry, i.e., ITO erasure or changes in AR. It is possible that once m has reached a certain width, that the increase in V_0 has reached a settling point where the 16 μm ITO erasure width has less of an effect on the widening electrospray cavity. At this distance, the IL is already experiencing a diminished electric field strength due to the emitter distance. This distance likely has a stronger effect than the 16 μm ITO erasure width is at this point. Since the results of Section 4.2 suggest the use of smaller-width electrospray cavities to minimize V_0, some guidelines can be considered. Regardless of the size of the electrospray cavity AR, it is important to minimize the amount of ITO erasure in all cases. Since smaller values of AR are desirable, and this is where the effects of ITO erasure are most pronounced, it is important to reduce the amount of ITO erased when fabricating emitters.

4.4 Ionic Liquid Comparison

As mentioned in Section 3.3.3, the ILs considered are BMPyrr-DCA, EMI-BF4, and EMI-Im. Table 3.2 may be referenced to review the ILs and their fluid properties. Although the relative permittivity and electrical conductivity are important properties to consider for full electromagnetic simulations, the only property of practical use in this electrostatic study is the fluid surface tension coefficient, γ. From Table 3.2 and Equation [2.3.27], it can be observed that ILs with lower values of γ will yield lower onset voltages. This is precisely what was shown when the ILs in this study were compared. Figures 4.11 – 4.13 show the values of V_0 with variations in AR (for the ILs considered in this study), for m values of 5 μm, 25 μm, and 50 μm, respectively.

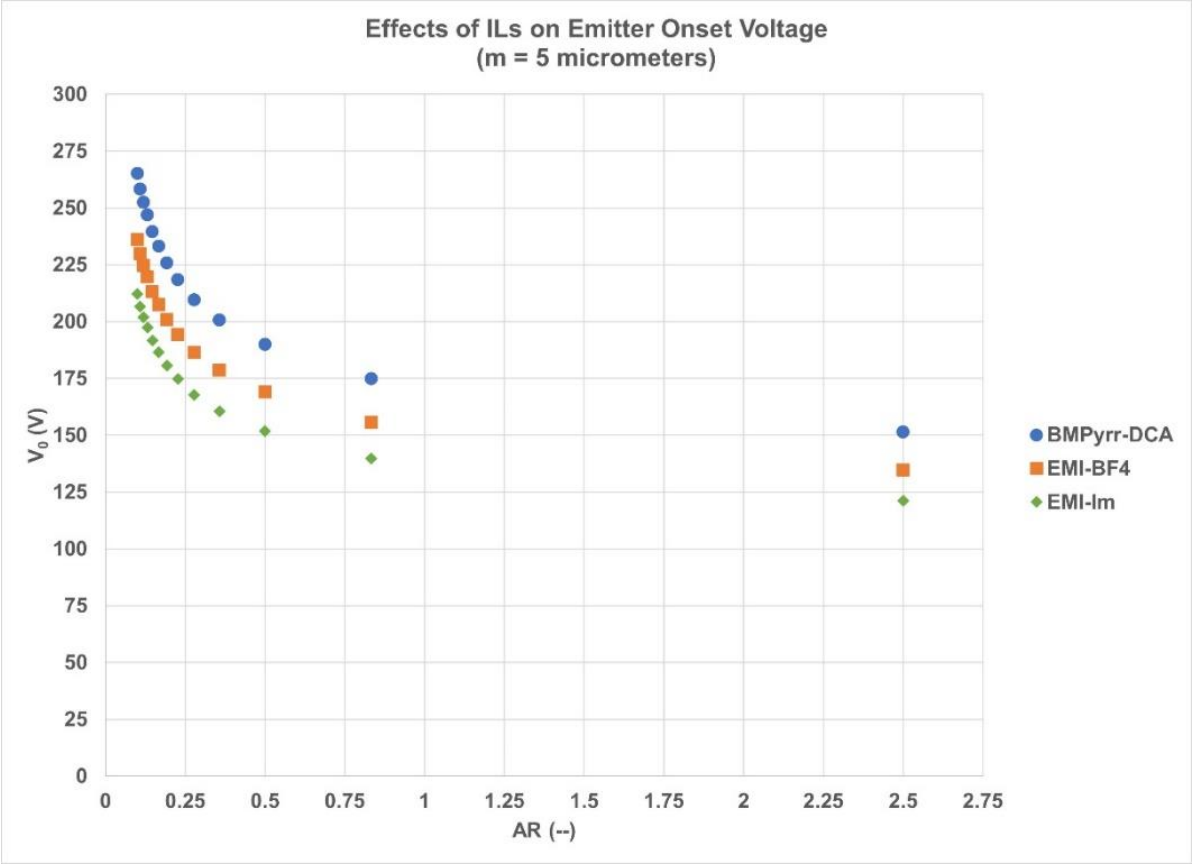

Figure 4.11. V_0 with variation in AR for the ILs considered in this study for $m = 5$ μm.

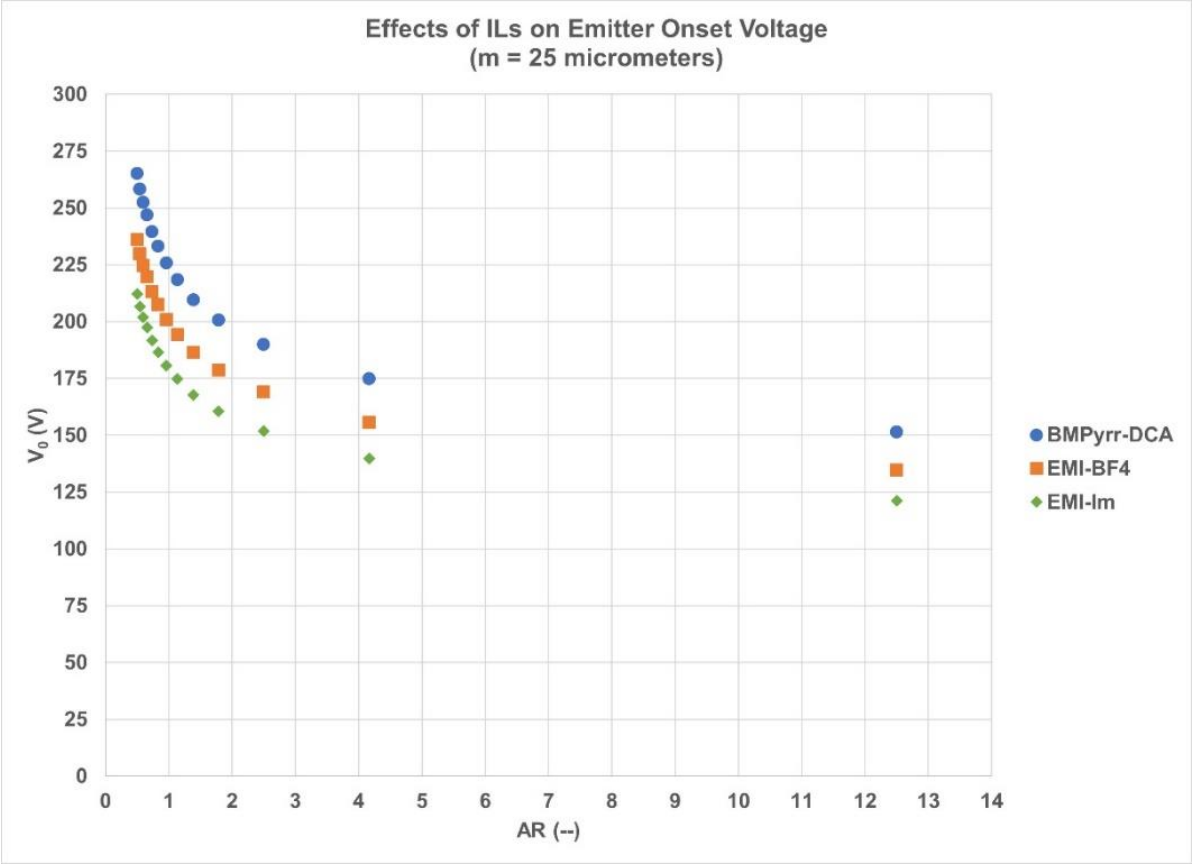

Figure 4.12. V_0 with variation in AR for the ILs considered in this study for $m = 25$ μm.

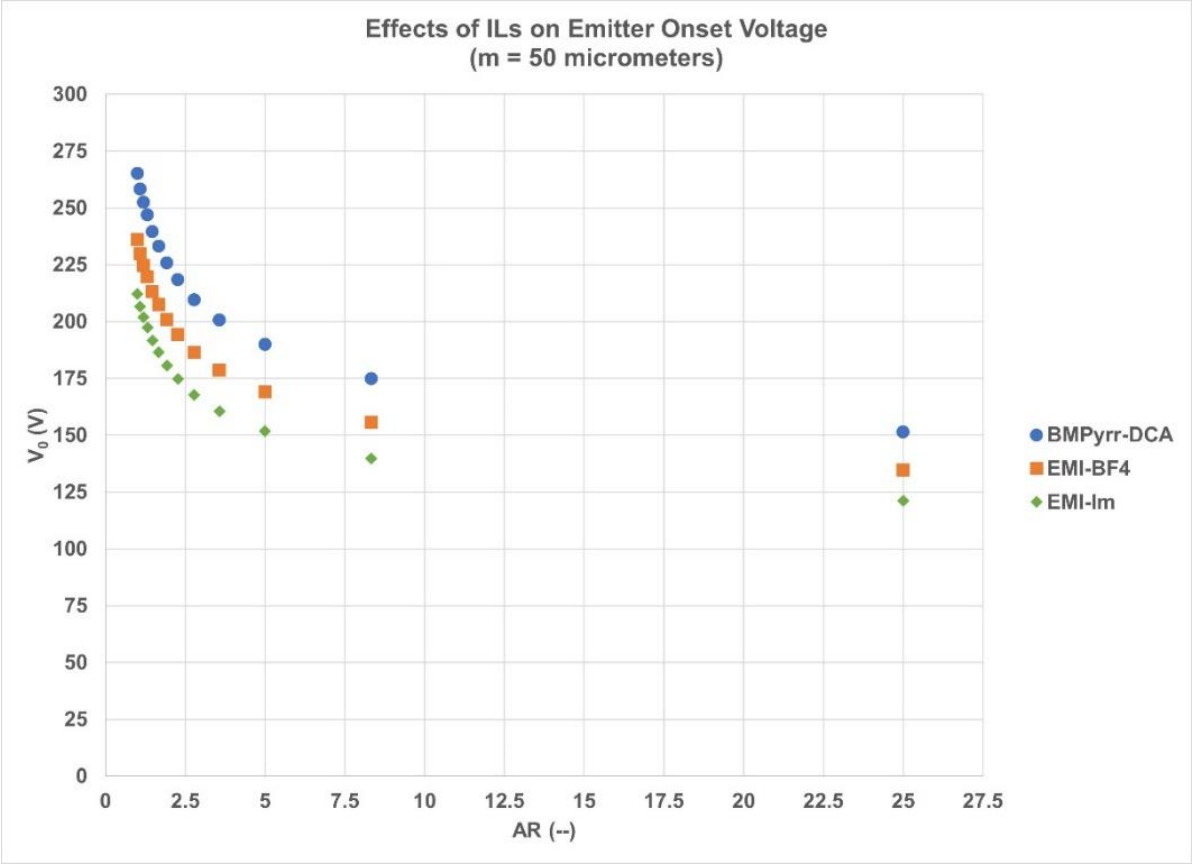

Figure 4.13. V_0 with variation in AR for the ILs considered in this study for $m = 50$ μm.

In all cases, the onset voltage increases as the values of γ increase for each IL. EMI-Im has the lowest surface tension coefficient, followed by EMI-BF4, and finally BMPyrr-DCA which has the highest γ value and consequentially, the highest values for V_0. Comparing the results here with those of Huang et al. [43], there is some discrepancy between the results. Huang et al. found that V_0 was lower for EMI-BF4 when compared to EMI-Im. This would indicate that other IL fluid properties are potentially having an impact on V_0 that are not accounted for by the electrostatic analysis. Since the current density and space charge depend on the conductivity of the IL [22], further investigation with a full electromagnetic solution is required to determine the potential impacts on emitter operation for both start up and steady-state operation.

4.5 Comparison of Single-Capillary Emitters and Multi-Capillary Arrays

Since practical electrospray thrusters rely on arrays of emitters in an emitter chip, it is important to consider the effects of their design on thruster power requirements. Due to the higher computational expense of this simulation type, simulations must be performed using the Linux based high-performance computing (HPC) clusters PRANDTL and INTEGRITY at UTSI. Simulations are sent to the cluster and run via a script. Utilizing all of the features of Ansys EDT [28] to run the simulations properly with the script proved challenging. A mesh-convergence study was performed to compare the results between simulations on the local machine (PC) and the INTEGRITY cluster. These results can be seen in Figure 4.14, where the results for E_{Apex} are compared for decreasing L_E between the two simulation methods. The solution is found to be mesh-independent in both INTEGRITY and PC cases for $L_E \leq 1$, as was determined in the convergence study for the single-capillary PC case. However, the PC results trend to lower values of E_{Apex} and converge to a higher value, while the INTEGRIY results trend to

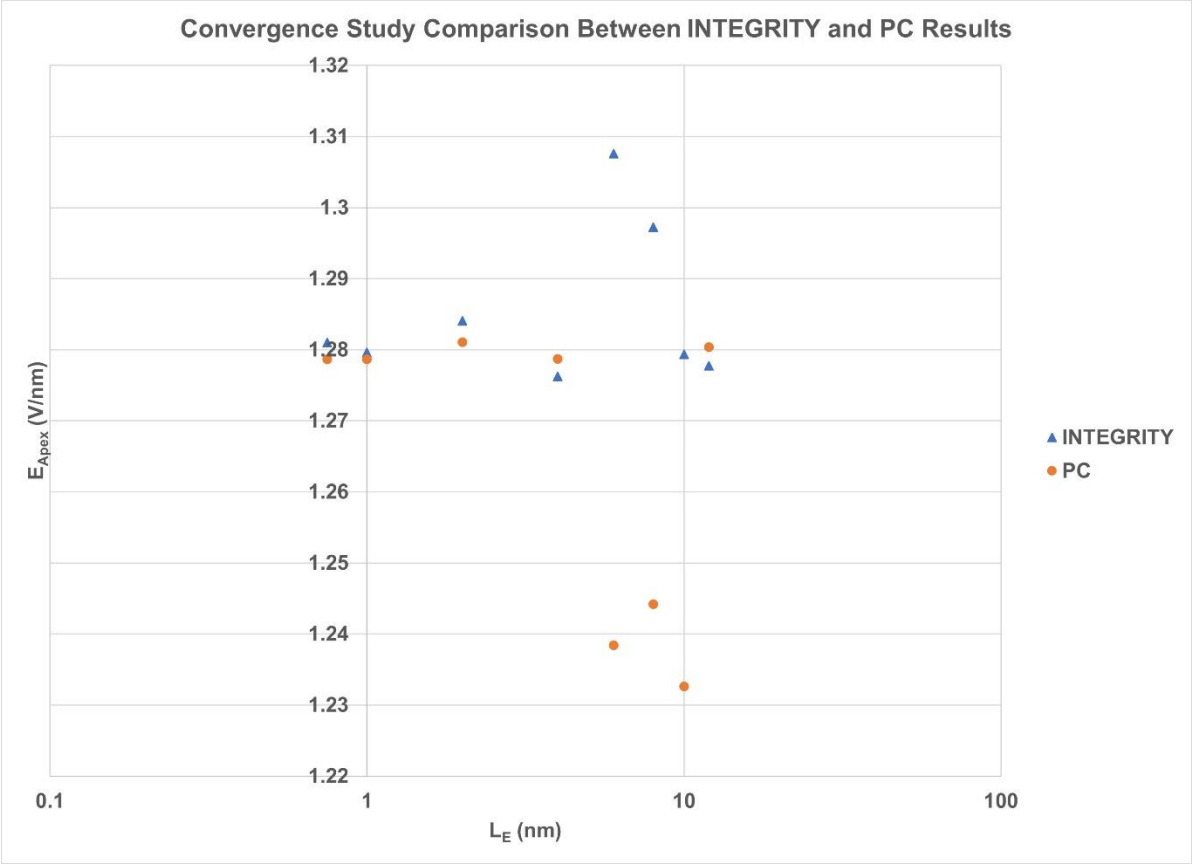

Figure 4.14. Comparison of convergence study results between the PC and INTEGRITY V_0 values.

higher values of E_{Apex} and then decrease until they converge to around the same values as the PC case. Since the models are identical, the behavior of the convergence trends should behave similarly between PC and INTEGRITY results. This behavior requires further analysis as it is not completely understood.

A method of comparison to check the results between the INTEGRITY and PC simulations was performed. This method included comparing the results of the single-capillary emitter chip run on the PC to the multi-capillary-array emitter chip with a high value of p. This choice was made since for sufficiently large p, the shielding effects between emitter capillaries is decreased, and the results approach those of a single-capillary emitter chip. Figure 4.15 shows the results of this comparison, which indicate that the simulation results are approximately equivalent. The highest recorded percent error between data collected from the INTEGRITY and PC simulations was $\sim$ 4%. This seems to indicate that, although the convergence study between PC and INTEGRITY differed slightly, the simulation results are comparably accurate. However, further convergence study data and comparisons in V_0 for several more cases of AR are required to ensure the validity of the results. Therefore, further simulations for multi-capillary emitter chips are omitted from this thesis and suggested as a topic for further study.

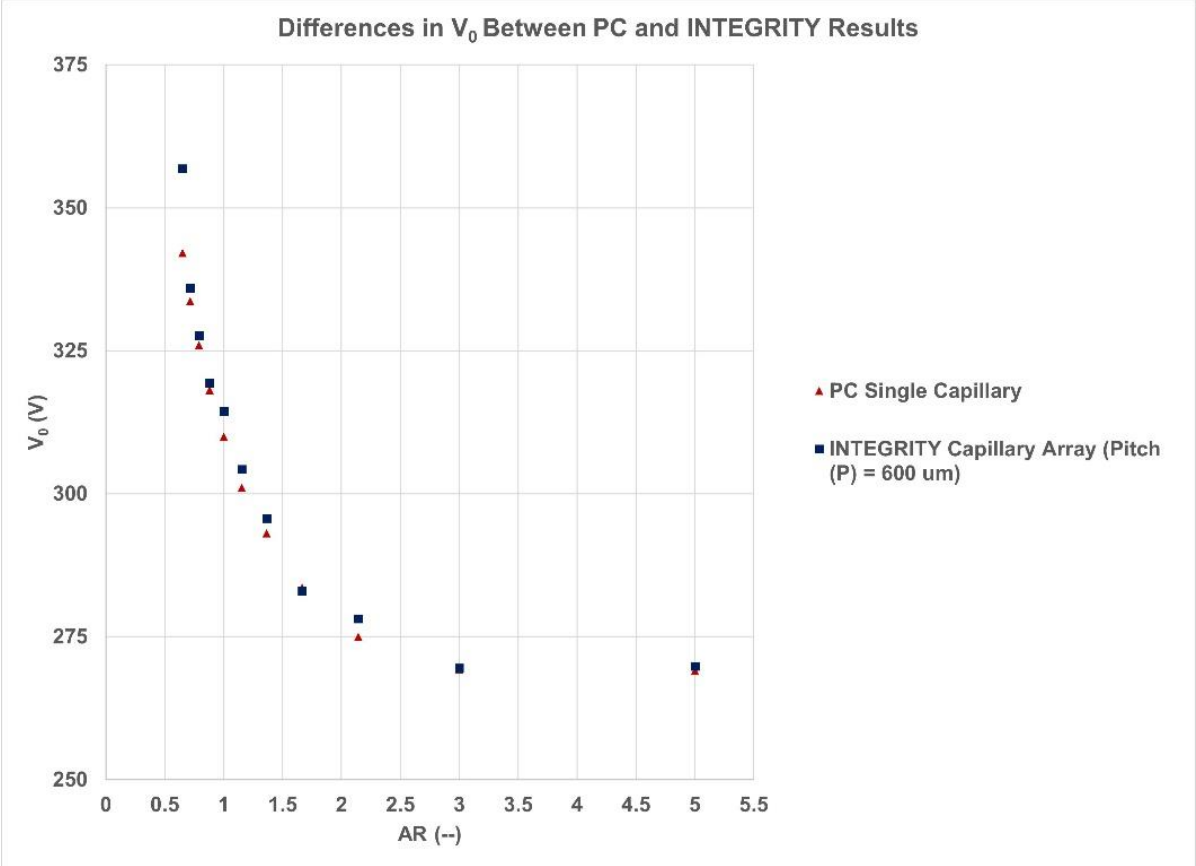

Figure 4.15. Comparison of V_0 results between a high-pitch, multi-emitter array on INTEGRITY and the single-capillary case on the PC.

CHAPTER 5: CONCLUSIONS AND FUTURE WORK

Based on the simulation results, several guidelines have been established to aid in the study of electrospray emitters. These guidelines can reduce development time by providing a starting point for future simulations based on the results in this thesis. The conclusions and guidelines determined in this thesis are listed below along with recommendations for future work on this topic.

5.1 Conclusions

The results of the study documented in this thesis have yielded several useful guidelines for either future numerical simulations or tests in the lab. The model used in this work was adapted from a method introduced by Krpoun and Shea [31], which they found to produce reasonably accurate results when compared with experimental data. Even so, it is useful to remember that the electrostatic assumptions used in the model will inevitably have some impact on the accuracy of the results. However, this model excels at producing computationally inexpensive and accurate results for V_0. With this in mind, based on the results of this study, several guidelines for emitter simulation, design, and testing should be considered:

- When m is considered a set design choice, values of the electrospray cavity AR should be less than 6 and, ideally, as close to 2.5 (this corresponds to $m = 5$ μm and $d = 2$ μm) as fabrication capabilities will allow. In this case, AR_{opt} can be found by taking the design choice for m and varying d in the electrostatic simulations.

- Design considerations when d is a set or predetermined value are much easier to analyze. Regardless of the design choice for d, m should be made as small as practical to minimize V_0. This study has found that values of m should be close to 5 μm or less, although future simulations with values of $m < 5$ μm are required to ascertain the trends in minimizing V_0 as m is decreased.

- The effects of ITO extraction grid erasure in the region of the electrospray cavity result in a large increase in V_0. This increase in V_0 due to increasing W_e becomes less profound as m and d are increased. Unfortunately, since V_0 is minimized for small m and d values, this effect is most pronounced for the values of m and d that are most desirable for minimizing V_0. Therefore, either ensuring that as little ITO is erased as possible or choosing an electrospray cavity with larger m and d values will result in an optimization of V_0 for a specific emitter-chip design.

- In order to minimize V_0 for simulations using an electrostatic assumption, an IL with the lowest value of γ should be used. However, based on the results of Huang et al. [43], electrical conductivity and the dielectric constants potentially play an important role in both start up and steady-state operation of electrospray emitters that must be considered in electrospray thruster design.

- The high-computational expense of simulating an emitter chip requires the use of HPC. A mesh-convergence study was performed to test the results between the INTEGRITY HPC cluster and the simulation results from PC analysis. The behavior of the convergence study differed between the two computational platforms even though the models used were identical. When a high-pitch emitter chip was compared with the single-capillary emitter, the results appeared to coincide with minimal variation. Although this is a promising result, further mesh-convergence studies are required, along with further simulations for V_0, to determine the accuracy of the results from utilizing the HPC cluster, INTEGRITY.

5.2 Suggestions for Future Work

Since definitive results for emitter arrays were not able to be determined in this study, this is one obvious area of research that needs to be built upon. This would involve determining the accuracy of the HPC simulations via further mesh-convergence studies, and then performing them for the emitter chip for the same variations as the single-capillary emitter to determine the effects of variations in AR on V_0 for emitter chips.

Since this work was based on an electrostatic model, a logical next step would be to perform a complete EHD analysis to obtain more data about the operation of the electrospray emitter beyond the establishment of onset voltage. This could be achieved by using a CFD solver and modifying the equations to account for the electromagnetic forces via a method similar to López-Herrera et al. [22], where the full EHD behavior was considered. Although these methods are computationally expensive, they represent the next step in numerical optimization studies and also have the ability to yield results of interest other than V_0.

Determination of V_0 for a full electromagnetic analysis could be used to compare with the experimental results of Huang et al. [43] to determine which ILs actually produce the lowest values of V_0. This full analysis would also yield other results of interest such as the effects of space charge and charge-current density on emitter operation. These effects are not solely dependent on the IL used, and their importance warrants further study of this phenomena. This form of analysis is suited to a model where the full EHD behavior is considered, such as the work by López-Herrera et al. [22] mentioned above.

The last suggestion for future work would be the design, fabrication, and testing of electrospray emitter prototypes. The results of this study could be used

in the design optimization of electrospray emitters. These emitters could then be tested in the laboratory, and the results for V_0 could be compared with the models examined in this thesis. The results of these tests could be very useful in determining future studies. If laboratory and theoretical results agree, it would validate the electrospray emitter design guidelines established in this study. If the results of the lab tests differ significantly from the results of this study, then further, more computationally expensive, dynamic simulations may be warranted to determine the source of the discrepancy. Results from laboratory tests also give a basis for comparison with empirical results that exist in the literature. This is obviously a very important next step in the novel electrospray emitter design developed by μSTAMPS in an effort to design and develop electrospray thruster technology for space missions.

WORKS CITED

[1] R. Jahn, *Physics of Electric Propulsion*. Mineola, NY: Dover Publications, 2006.

[2] F. Ebersohn, L. Raja and J. Shebalin, "Resistive Magnetohydrodynamic Study of Magnetic Field Effects on Plasma Plumes," *44th AIAA Plasmadynamics and Lasers Conference*, 2013. doi: 10.2514/6.2013-2759.

[3] Y. Song, Y. Lee, J. Park and S. Park, "CANYVAL-X: Operational Scenario and Strategy," *2018 SpaceOps Conference*, 2018. doi: 10.2514/6.2018-2636.

[4] M. Keidar, "Micro-Cathode Arc Thruster for small satellite propulsion," *2016 IEEE Aerospace Conference*, pp. 1-7, doi: 10.1109/AERO.2016.7500506.

[5] “GMS: CANYVAL-X: CubeSat Astronomy by NASA and Yonsei using Virtual Telescope Alignment eXperiment,” Oct. 13, 2015. https://svs.gsfc.nasa.gov/vis/a010000/a012000/a012025/

[6] I. Levchenko, M. Keidar, J. Cantrell, Y. Wu, H. Kuninaka, K. Bazaka and S. Xu, "Explore space using swarms of tiny satellites," *Nature*, vol. 562, no. 7726, pp. 185-187, 2018 [Online]. Available: https://www.nature.com/articles/d41586-018-06957-2. doi: 10.1038/d41586-018-06957-2

[7] T. Gray, "SpaceX launches latest Starlink mission – NASASpaceFlight," *NASASpaceFlight.com*, 2020. [Online]. Available: https://www.nasaspaceflight.com/2020/09/spacex-falcon-launch-starlink-11.

[8] "OneWeb satellite constellation for global internet access – AerospaceTechnology," *Aerospace-technology.com*, 2021. [Online]. Available: https://www.aerospace-technology.com/projects/oneweb-satellite-constellation.

[9] J. Foust, "SpaceX continues Starlink deployment with latest launch – SpaceNews," *SpaceNews.com*, 2021. [Online]. Available: https://spacenews.com/spacex-continues-starlink-deployment-with-latest-launch.

[10] M. Wall, "Arianespace Soyuz rocket launches 34 OneWeb internet satellites into space," *Space.com*, 2021. [Online]. Available: https://www.space.com/arianespace-sozyuz-launches-oneweb-9-internet-satellite-mission.

[11] A. Sengupta *et al.*, “Deep Space 1 Flight Spare Ion Thruster 30,000-Hour Life Test,” *Journal of Propulsion and Power*, vol. 25, no. 1, pp. 105–117, Jan. 2009, doi: 10.2514/1.36549.

[12] J. Brophy, C. Garner, B. Nakazono, M. Marcucci, M. Henry, and D. Noon, “The Ion Propulsion System for Dawn,” presented at the 39th AIAA/ASME/SAE/ASEE Joint Propulsion Conference and Exhibit, Huntsville, Alabama, Jul. 2003. doi: 10.2514/6.2003-4542.

[13] G. Anderson, J. Anderson, M. Anderson, G. Aveni, D. Bame, P. Barela, K. Blackman, A. Carmain, L. Chen, M. Cherng, S. Clark, M. Connally, W. Connolly, D. Conroy, M. Cooper, C. Cutler, J. D’Agostino, N. Demmons, E. Dorantes, C. Dunn, M. Duran, E. Ehrbar, J. Evans, J. Fernandez, G. Franklin, M. Girard, J. Gorelik, V. Hruby, O. Hsu, D. Jackson, S. Javidnia, D. Kern, M. Knopp, R. Kolasinski, C. Kuo, T. Le, I. Li, O. Liepack, A. Littlefield, P. Maghami, S. Malik, L. Markley, R. Martin, C. Marrese-Reading, J. Mehta, J. Mennela, D. Miller, D.

Nguyen, J. O'Donnell, R. Parikh, G. Plett, T. Ramsey, T. Randolph, S. Rhodes, A. Romero-Wolf, T. Roy, A. Ruiz, H. Shaw, J. Slutsky, D. Spence, J. Stocky, J. Tallon, I. Thorpe, W. Tolman, H. Umfress, R. Valencia, C. Valerio, W. Warner, J. Wellman, P. Willis, J. Ziemer, J. Zwahlen, M. Armano, H. Audley, J. Baird, P. Binetruy, M. Born, D. Bortoluzzi, E. Castelli, A. Cavalleri, A. Cesarini, A. Cruise, K. Danzmann, M. de Deus Silva, I. Diepholz, G. Dixon, R. Dolesi, L. Ferraioli, V. Ferroni, E. Fitzsimons, M. Freschi, L. Gesa, F. Gibert, D. Giardini, R. Giusteri, C. Grimani, J. Grzymisch, I. Harrison, G. Heinzel, M. Hewitson, D. Hollington, D. Hoyland, M. Hueller, H. Inchauspé, O. Jennrich, P. Jetzer, N. Karnesis, B. Kaune, N. Korsakova, C. Killow, J. Lobo, I. Lloro, L. Liu, J. López-Zaragoza, R. Maarschalkerweerd, D. Mance, N. Meshksar, V. Martín, L. Martin-Polo, J. Martino, F. Martin-Porqueras, I. Mateos, P. McNamara, J. Mendes, L. Mendes, M. Nofrarias, S. Paczkowski, M. Perreur-Lloyd, A. Petiteau, P. Pivato, E. Plagnol, J. Ramos-Castro, J. Reiche, D. Robertson, F. Rivas, G. Russano, C. Sopuerta, T. Sumner, D. Texier, D. Vetrugno, S. Vitale, G. Wanner, H. Ward, P. Wass, W. Weber, L. Wissel, A. Wittchen and P. Zweifel, "Experimental results from the ST7 mission on LISA Pathfinder," *Physical Review D*, vol. 98, no. 10, 2018 [Online]. Available: https://journals.aps.org/prd/abstract/10.1103/PhysRevD.98.102005. doi: 10.1103/PhysRevD.98.102005.

[14] "Colloid Microthrusters Demonstrated on LISA Pathfinder | Science Mission Directorate," *Science.nasa.gov*, 2021. [Online]. Available: https://science.nasa.gov/technology/technology-highlights/colloid-microthrusters-demonstrated-on-lisa-pathfinder.

[15] T. Rohner, N. Lion and H. Girault, "Electrochemical and theoretical aspects of electrospray ionization," *Physical Chemistry Chemical Physics*, vol. 6, no. 12, p. 3056, 2004 [Online]. Available: https://pubs.rsc.org/en/content/articlehtml/2004/cp/b316836k?casa_token=dikxh_

BIfR4AAAAA:VMz9lzQ8RINyiMTafBxZtPs3vacCmxW_vU99dqtIdq4eMWImEavmZEqVrlkS-Auk-i8Pybhlo0nb0mg. doi: 10.1039/B316836K.

[16] G. Taylor "Disintegration of water drops in an electric field," *Proceedings of the Royal Society of London. Series A. Mathematical and Physical Sciences*, vol. 280, no. 1382, pp. 383-397, 1964 [Online]. Available: https://royalsocietypublishing.org/doi/abs/10.1098/rspa.1964.0151. doi: 10.1098/rspa.1964.0151.

[17] W. Gilbert, M. Allchin and W. Allchin, *William Gilbert of Colchester, physician of London, On the magnet*. London: Chiswick Press, 1901, p. 215. [Online]. Available: https://www.gutenberg.org/files/33810/33810-h/33810-h.htm.

[18] J. Zeleny, “The Electrical Discharge from Liquid Points, and a Hydrostatic Method of Measuring the Electric Intensity at Their Surfaces,” *Phys. Rev.*, vol. 3, no. 2, pp. 69–91, Feb. 1914, doi: 10.1103/PhysRev.3.69.

[19] J. Zeleny, “The Discharge of Electricity from Pointed Conductors Differing in Size,” *Phys. Rev. (Series I)*, vol. 25, no. 5, pp. 305–333, Nov. 1907, doi: 10.1103/PhysRevSeriesI.25.305.

[20] J. Zeleny, “Instability of Electrified Liquid Surfaces,” *Phys. Rev.*, vol. 10, no. 1, pp. 1–6, Jul. 1917, doi: 10.1103/PhysRev.10.1.

[21] J. R. Melcher and G. I. Taylor, “Electrohydrodynamics: A Review of the Role of Interfacial Shear Stresses,” *Annual. Rev. Fluid Mech.*, vol. 1, no. 1, pp. 111–146, Jan. 1969, doi: 10.1146/annurev.fl.01.010169.000551.

[22] J. M. López-Herrera, S. Popinet, and M. A. Herrada, “A charge-conservative approach for simulating electrohydrodynamic two-phase flows using volume-of-fluid,” *Journal of Computational Physics*, vol. 230, no. 5, pp. 1939–1955, Mar. 2011, doi: 10.1016/j.jcp.2010.11.042.

[23] S. Popinet, “Gerris: a tree-based adaptive solver for the incompressible Euler equations in complex geometries,” *Journal of Computational Physics*, vol. 190, no. 2, pp. 572–600, Sep. 2003, doi: 10.1016/S0021-9991(03)00298-5.

[24] M. A. Herrada, J. M. López-Herrera, A. M. Gañán-Calvo, E. J. Vega, J. M. Montanero, and S. Popinet, “Numerical simulation of electrospray in the cone-jet mode,” *Phys. Rev. E*, vol. 86, no. 2, p. 026305, Aug. 2012, doi: 10.1103/PhysRevE.86.026305.

[25] A. M. Gañán-Calvo, “THE SURFACE CHARGE IN ELECTROSPRAYING: ITS NATURE AND ITS UNIVERSAL SCALING LAWS,” *Journal of Aerosol Science*, vol. 30, no. 7, pp. 863–872, Aug. 1999, doi: 10.1016/S0021-8502(98)00780-0.

[26] A. M. Gañán-Calvo, J. Dávila, and A. Barrero, “Current and droplet size in the electrospraying of liquids. Scaling laws,” *Journal of Aerosol Science*, vol. 28, no. 2, pp. 249–275, Mar. 1997, doi: 10.1016/S0021-8502(96)00433-8.

[27] O. Lastow and W. Balachandran, “Numerical simulation of electrohydrodynamic (EHD) atomization,” *Journal of Electrostatics*, vol. 64, no. 12, pp. 850–859, Nov. 2006, doi: 10.1016/j.elstat.2006.02.006.

[28] “Ansys | Engineering Simulation Software.” https://www.ansys.com/.

[29] D. P. H. Smith, “The Electrohydrodynamic Atomization of Liquids,” *IEEE Trans. on Ind. Applicat.*, vol. IA-22, no. 3, pp. 527–535, May 1986, doi: 10.1109/TIA.1986.4504754.

[30] M. G. Ikonomou, A. T. Blades, and Paul. Kebarle, “Electrospray-ion spray: a comparison of mechanisms and performance,” *Anal. Chem.*, vol. 63, no. 18, pp. 1989–1998, Sep. 1991, doi: 10.1021/ac00018a017.

[31] R. Krpoun and H. R. Shea, “A method to determine the onset voltage of single and arrays of electrospray emitters,” *Journal of Applied Physics*, vol. 104, no. 6, p. 064511, Sep. 2008, doi: 10.1063/1.2981077.

[32] C. N. Ryan, K. L. Smith, M. S. Alexander, and J. P. W. Stark, “Effect of emitter geometry on flow rate sensitivity to voltage in cone jet mode electrospray,” *J. Phys. D: Appl. Phys.*, vol. 42, no. 15, p. 155504, Aug. 2009, doi: 10.1088/0022-3727/42/15/155504.

[33] C. N. Ryan, K. L. Smith, and J. P. W. Stark, “The influence of geometry on the flow rate sensitivity to applied voltage within cone-jet mode electrospray,” *Journal of Applied Physics*, vol. 112, no. 11, p. 114510, Dec. 2012, doi: 10.1063/1.4768451.

[34] J. M. Jones, T. M. Moeller, L. Costa, B. K. Canfield, and A. Terekhov, “Numerical investigation of the effects of geometry and materials on the onset voltage of electrospray emitters,” *Journal of Electrostatics*, vol. 108, p. 103487, Nov. 2020, doi: 10.1016/j.elstat.2020.103487.

[35] R. T. Kelly, J. S. Page, K. Tang, and R. D. Smith, “Array of Chemically Etched Fused-Silica Emitters for Improving the Sensitivity and Quantitation of Electrospray

Ionization Mass Spectrometry," *Anal. Chem.*, vol. 79, no. 11, pp. 4192–4198, Jun. 2007, doi: 10.1021/ac062417e.

[36] B. Ticknor, J. Anderson, B. Fritz, and Y.-H. Chiu, "Effect of Aspect Ratio on the Wettability and Electrospray Properties of Porous Tungsten Emitters with the Ionic Liquid [Emim][Im]," presented at the 46th AIAA/ASME/SAE/ASEE Joint Propulsion Conference & Exhibit, Nashville, TN, Jul. 2010. doi: 10.2514/6.2010-6618.

[37] C. Guerra-Garcia, D. Krejci, and P. Lozano, "Spatial uniformity of the current emitted by an array of passively fed electrospray porous emitters," *J. Phys. D: Appl. Phys.*, vol. 49, no. 11, p. 115503, Mar. 2016, doi: 10.1088/0022-3727/49/11/115503.

[38] A. Terekhov, B. K. Canfield, J. M. Jones, T. M. Moeller, and L. Costa, "Ultrafast Laser Fabrication of Capillary Electrospray Emitter Arrays.," *Lasers in Engineering (Old City Publishing)*, vol. 49, no. 4–6, pp. 353–359, 2021.

[39] E. Jennett, M. Motamedi, S. Rastegar, C. Frederickson, C. Arcoria, and J. M. Powers, "Dye-enhanced Ablation of Enamel by Pulsed Lasers," *J Dent Res*, vol. 73, no. 12, pp. 1841–1847, Dec. 1994, doi: 10.1177/00220345940730120801.

[40] J. Song, D. Kong, X. Zhang, H. Wang, and Y. Dai, "LIPSS-covered annular ablation region induced on ZnO surface by focusing femtosecond laser beam spatially shaped by bubbles in cedar oil," *Appl. Phys. A*, vol. 127, no. 1, p. 18, Jan. 2021, doi: 10.1007/s00339-020-04149-2.

[41] C. Ma, T. Bull, and C. N. Ryan, “Plume Composition Measurements of a High-Emission-Density Electrospray Thruster,” *Journal of Propulsion and Power*, vol. 37, no. 6, pp. 816–831, Nov. 2021, doi: 10.2514/1.B37996.

[42] C. Huang, J. Li, M. Li, T. Si, C. Xiong, and W. Fan, “Experimental investigation on current modes of ionic liquid electrospray from a coned porous emitter,” *Acta Astronautica*, vol. 183, pp. 286–299, Jun. 2021, doi: 10.1016/j.actaastro.2021.03.014.

[43] C. Huang, J. Li, M. Li, T. Si, C. Xiong, and W. Fan, “Emission Performance of Ionic Liquid Electrospray Thruster for Micropropulsion,” *Journal of Propulsion and Power*, pp. 1–9, Aug. 2021, doi: 10.2514/1.B37878.

[44] R. B. Bird, W. E. Stewart, and E. N. Lightfoot, *Transport phenomena*, Revised ed. New York: Wiley, 2007.

[45] S. Orfanidis, *Electromagnetic Waves and Antennas*. Piscataway, N.J, 2016.

[46] J. U. Brackbill, D. B. Kothe, and C. Zemach, “A continuum method for modeling surface tension,” *Journal of Computational Physics*, vol. 100, no. 2, pp. 335–354, Jun. 1992, doi: 10.1016/0021-9991(92)90240-Y.

[47] J. D. Kraus, *Electromagnetics*, 3rd ed. New York: McGraw-Hill, 1984.

[48] J. Song, “Research Progress of Ionic Liquids as Lubricants,” *ACS Omega*, vol. 6, no. 44, pp. 29345–29349, Nov. 2021, doi: 10.1021/acsomega.1c04512.

[49] D. A. Saville, “ELECTROHYDRODYNAMICS: The Taylor-Melcher Leaky Dielectric Model,” *Annu. Rev. Fluid Mech.*, vol. 29, no. 1, pp. 27–64, Jan. 1997, doi: 10.1146/annurev.fluid.29.1.27.

[50] S. Maheshwari and H.-C. Chang, “Anomalous conical menisci under an ac field-departure from the dc Taylor cone,” *Appl. Phys. Lett.*, vol. 89, no. 23, p. 234103, Dec. 2006, doi: 10.1063/1.2402883.

[51] M. Gamero-Castaño, I. Aguirre-de-Carcer, L. de Juan, and J. Fernández de la Mora, “On the current emitted by Taylor cone-jets of electrolytes in vacuo: Implications for liquid metal ion sources,” *Journal of Applied Physics*, vol. 83, no. 5, pp. 2428–2434, Mar. 1998, doi: 10.1063/1.367002.

[52] M.-M. Huang, Y. Jiang, P. Sasisanker, G. W. Driver, and H. Weingärtner, “Static Relative Dielectric Permittivities of Ionic Liquids at 25 °C,” *J. Chem. Eng. Data*, vol. 56, no. 4, pp. 1494–1499, Apr. 2011, doi: 10.1021/je101184s.

[53] E. L. Bennett, C. Song, Y. Huang, and J. Xiao, “Measured relative complex permittivities for multiple series of ionic liquids,” *Journal of Molecular Liquids*, vol. 294, p. 111571, Nov. 2019, doi: 10.1016/j.molliq.2019.111571.

[54] N. Zec, M. Bešter-Rogač, M. Vraneš, and S. Gadžurić, “Physicochemical properties of (1-butyl-1-methylpyrrolydinium dicyanamide + γ-butyrolactone) binary mixtures,” *The Journal of Chemical Thermodynamics*, vol. 91, pp. 327–335, Dec. 2015, doi: 10.1016/j.jct.2015.08.014.

[55] C. Schreiner, S. Zugmann, R. Hartl, and H. J. Gores, “Fractional Walden Rule for Ionic Liquids: Examples from Recent Measurements and a Critique of the So-

Called Ideal KCl Line for the Walden Plot," *J. Chem. Eng. Data*, vol. 55, no. 5, pp. 1784–1788, May 2010, doi: 10.1021/je900878j.

[56] L. G. Sánchez, J. R. Espel, F. Onink, G. W. Meindersma, and A. B. de Haan, "Density, Viscosity, and Surface Tension of Synthesis Grade Imidazolium, Pyridinium, and Pyrrolidinium Based Room Temperature Ionic Liquids," *J. Chem. Eng. Data*, vol. 54, no. 10, pp. 2803–2812, Oct. 2009, doi: 10.1021/je800710p.

[57] W. Martino, J. F. de la Mora, Y. Yoshida, G. Saito, and J. Wilkes, "Surface tension measurements of highly conducting ionic liquids," *Green Chem.*, vol. 8, no. 4, p. 390, 2006, doi: 10.1039/b515404a.

[58] M. Geppert-Rybczyńska, J. K. Lehmann, and A. Heintz, "Surface Tensions and the Gibbs Excess Surface Concentration of Binary Mixtures of the Ionic Liquid 1-Ethyl-3-methylimidazolium Bis[(trifluoromethyl)sulfonyl]imide with Tetrahydrofuran and Acetonitrile," *J. Chem. Eng. Data*, vol. 56, no. 4, pp. 1443–1448, Apr. 2011, doi: 10.1021/je101146f.

VITA

Joshua Howell is a mechanical engineering major with a love for propulsion and aerospace. Ever since he was a child, he has found inspiration from science fiction and has thought about what the future of space travel might look like for the human race. Joshua completed his bachelor's degree in mechanical engineering at Lipscomb University (Nashville, TN) in 2019, where he participated in the construction and launch of a high-powered rocket for the NASA University Student Launch Initiative as a senior project. He completed his master's degree in mechanical engineering at the University of Tennessee Space Institute (UTSI) (Tullahoma, TN) in the Spring of 2022. Joshua worked under his major advisor Dr. Trevor Moeller as a graduate research assistant on numerical optimization of a novel electrospray thruster design with support from his advisors, Dr. Brian Canfield, and Dr. Lino Costa. Having finished his master's degree, he will continue researching under Dr. Moeller in the doctoral program at UTSI. After completing his doctoral work, it is Joshua's goal to obtain a position in research and academia to continue his aerospace research and to help inspire the next generation of engineers. Joshua resides in Franklin, TN with his wife and daughter.